Fracture instability in nuclear graphite

Andreas Andriotis

A dissertation submitted to the University of Bristol in accordance with the requirements for award of the degree of Doctor of Philosophy in the Faculty of Engineering

Department of Mechanical Engineering
November 2017

c. 38 500 words

Synopsis

This dissertation considers the fracture instability of nuclear graphite, specifically of isotropic Gilsocarbon, grade IM1-24, which acts as a structural component and neutron moderator within reactors. The presence of cracks within this graphite informs its behaviour and necessitates a study of fracture properties and instability. Amongst the factors studied, a major finding was that the size effect was the most prevalent. Two aspects of instability were also examined: the crack driving force or energy release rate and the fracture resistance or the incremental work of fracture. The conditions between the extremes of load control and displacement control affecting the energy release rate were studied, based on the compliance of the surrounding components or additional elastic material, generally known as elastic follow-up. The effects of elastic follow-up and specimen geometry on fracture instability was investigated in an idealised model. Two sets of experiments were presented to quantify the effect and to validate the idealised benchmark study. No measurable differences were exhibited at the equivalent degrees of elastic follow-up achieved in the experimental work. Additionally, the effects of load multiaxiality on the fracture of graphite were investigated. Despite the influence of load multiaxiality on fracture stress of graphite, there was little effect in post-peak fracture behaviour indicating the lack of influence on fracture stability. Moreover, to evaluate fracture resistance, this work investigated the crack growth resistance curves, K_{R} and R. To produce these curves, a considerable number of experiments of cyclic load and unload, with crack propagation, is presented. Different sized compact tension specimens were tested, to investigate the size effect typically exhibited in quasi-brittle materials which describes the fracture behaviour of IM1-24. The rising K_{R} and R-curve behaviour observed in all sizes, especially in the more distinct initial fracture stages of K_{R}, can be attributed to the formation of a bridging zone in the wake of the propagating crack. A mismatch between the scaling of the fracture process zone and the specimens was also exhibited, evident from the considerable differences in apparent toughness K_{Q} as well as the linear elastic contributions to the work of fracture. The results indicated that the fracture stability of IM1-24 graphite is only marginally affected by elastic follow-up, whilst size effect is a more prominent contributor.

To my beloved parents

Acknowledgements

This work could not have been possible without the guidance of my supervisor Professor David Smith. His untimely death cost us all, I am very grateful for his help and the chance to work with him.

I am also very grateful to my supervisor Dr Mahmoud Mostafavi, whose encouragement and expertise proved invaluable in the later stages of my PhD.

I would also like to thank Professor Martyn Pavier, for his smart and practical pieces of advice and Professor Peter Flewitt for his academic depth throughout our constructive discussions.

I would not have chosen to embark on my PhD if it were not for the supervision of Professor George Lampeas and Dr Ioannis Diamantakos during the final years of my undergraduate degree, at the University of Patras. Both of them helped me develop my curiosity, pushing me into the complexities of fracture mechanics.

I thank all the members of the Solid Mechanics Research Group, past and present, for making the office a great place to be and work. A special mention to Dr Graeme Horne for welcoming me to the group, Dr Derreck Van Gelderen for his assistance in all experimental matters and beyond and Dr Dong Liu for the adventures we had triggering all kinds of alarms in Engin-X and POLDI.

I would also like to thank Steve Harding and Guy Pearn for all the experimental support. I thank Dr Julie Etches for lending me the Department of Aerospace Engineering's imaging equipment and James Webley, our faculty librarian, for his perseverance in tracking down my most obscure requests.

Many thanks and gratitude to all my friends and PhD colleagues. I will personally thank you over a pint and if I do not, point me to this line and I will make amends.

Last, and by no means least, I am extremely grateful for the support of my parents, Pantelis and Amalia. Both of them encouraged me into undertaking the PhD journey and helped me tremendously throughout these years. My father is not here to see me finish but I hope I have made him proud.

Andreas Andriotis
November 2017

Author's declaration

I declare that the work in this dissertation was carried out in accordance with the requirements of the University's Regulations and Code of Practice for Research Degree Programmes and that it has not been submitted for any other academic award. Except where indicated by specific reference in the text, the work is the candidate's own work. Work done in collaboration with, or with the assistance of, others, is indicated as such. Any views expressed in the dissertation are those of the author.

Signed: Date:

Table of Contents

List of Tables **9**

List of Figures **10**

List of Abbreviations **15**

List of Latin Characters **16**

List of Greek Characters **18**

1 Introduction **19**
1.1 Background . . . 19
1.2 Research Aim & Objectives . . . 20
1.3 Overview of dissertation structure . . . 20

2 Literature review **22**
2.1 Graphite . . . 22
2.1.1 Structure . . . 22
2.1.2 Artificial graphite . . . 23
2.2 Linear elastic fracture mechanics . . . 24
2.2.1 Instability . . . 25
2.2.2 Structure compliance . . . 27
2.3 Fracture resistance . . . 29
2.3.1 Sakai 1983 . . . 29
2.3.2 Sakai 1988 . . . 32
2.3.3 Ouagne 2002 . . . 34
2.3.4 Hodgkins 2006 . . . 36
2.3.5 Other studies . . . 38
2.3.6 Summary . . . 40
2.4 Size effect . . . 42
2.4.1 Sakai 1995 . . . 48
2.4.2 Statistical size effect . . . 49

3 Instability and boundary conditions **51**
3.1 Instability . . . 52
3.1.1 Dimensionless load and displacement . . . 52
3.1.2 Dimensionless total energy . . . 53
3.2 Elastic follow-up . . . 57
3.2.1 Series . . . 57
3.2.2 Parallel . . . 59
3.2.3 Dimensionless total energy, load and displacement . . . 59
3.3 Series model . . . 61
3.3.1 Variables and structure . . . 63
3.3.2 Assumptions and conventions . . . 64
3.3.3 Results and comparison . . . 66
3.4 Discussion . . . 67

4 Elastic follow-up effect **73**
4.1 Biaxiality experiment, series . . . 74
4.1.1 Background . . . 74
4.1.2 Design . . . 75
4.1.3 Setup and procedure . . . 77
4.2 Results and analysis . . . 79
4.2.1 Uniaxial . . . 79
4.2.2 Biaxial . . . 82
4.2.3 Finite element analysis . . . 83
4.2.4 Flexural strength . . . 89
4.2.5 Elastic modulus . . . 90
4.3 Three bar experiment, parallel . . . 92
4.3.1 Design . . . 92
4.3.2 Setup and procedure . . . 93
4.3.3 Results . . . 94
4.4 Discussion . . . 96
4.4.1 Series experiment, uniaxial, biaxial . . . 96
4.4.2 Three bar experiment, parallel . . . 101

5 Fracture size effect **104**
5.1 Experimental Details . . . 105
5.1.1 Design . . . 105
5.1.2 Setup and procedure . . . 108
5.2 Results . . . 112
5.2.1 Load CMOD . . . 112
5.2.2 Discrepancies . . . 113
5.3 Analysis . . . 116
5.3.1 Cycle linear regression . . . 116
5.3.2 Crack length measurements . . . 119
5.3.3 K_{R} calculations . . . 126

5.3.4 Size effect . . . 128
5.3.5 R curves . . . 132
5.4 Discussion . . . 137
5.4.1 Unloading compliance . . . 137
5.4.2 Crack length estimations . . . 137
5.4.3 Fracture toughness K_{R} . . . 138
5.4.4 Apparent toughness and size effect . . . 139
5.4.5 R curves and work of fracture . . . 140

6 Conclusions **142**
6.1 Overall conclusions . . . 142
6.2 Recommendations for further work . . . 145

References **146**

Appendices **159**

A Energy release rate with compliant structure derivation **159**

B Interpolation & Regression **161**

List of Tables

3.1 Model specimen geometry variables 63
3.2 Model specimen material variables 63

4.1 Uniaxial test data 80
4.2 Biaxial test data 83

5.1 C(T) specimen dimensions. 106
5.2 Comparison of LEFM and R_{ini} contributions to γ_{wof}. 136
5.3 Comparison of LEFM and R_{pla} contributions to γ_{wof}. 136

List of Figures

2.1 Displacement control or fixed displacement 26
2.2 Load control or fixed load 27
2.3 R curve and driving force comparing load control P and displacement control Δ. 27
2.4 Structure with finite compliance. 28
2.5 Schematic of loading and unloading paths BC, DE used to graphically determine fracture parameters. 31
2.6 Curved loading and unloading paths BC, DE used to graphically determine J_R. 32
2.7 R-curve values for IM1-24 compact tension (C(T)) specimen, crack increment measurements taken with video camera. 35
2.8 R-curve values for Type A (short) and Type B (long) IM1-24 non-standard compact tension (C(T)) specimens, crack increment calculation from compliance. 38
2.9 Diagram of the R-curve and the mechanisms associated with each stage to crack length increase. 43
2.10 Size effect law asymptote. 46
2.11 Size effect plot of apparent toughness K_Q of different specimen types versus the brittleness number β. 49

3.1 Dimensionless equilibrium load-displacement showing the relationship of dimensionless compliance z_{ll} and shape factor Y, for increasing crack lengths ($\alpha_0 = 0.2 \rightarrow 0.9$) in compact tension (C(T)) and single edge notch beam (SEN(B)) standard specimen geometries. Straight lines plotted from point $0, 0$ to peak dimensionless loads for illustration purposes. 54
3.2 Dimensionless equilibrium total energy with relative crack length showing the fracture behaviour of compact tension (C(T)) and single edge notch beam (SEN(B)) standard specimen geometries for increasing crack lengths ($\alpha_0 = 0.2 \rightarrow 0.9$). 56
3.3 Dimensionless equilibrium total energy with relative crack length showing the fracture behaviour of middle tension (M(T)) standard specimen geometry, for increasing crack lengths ($\alpha_0 = 0.2 \rightarrow 0.9$), with various length to width ratios (L/W). 56

3.4 Simple element models. (a) Series model, (b) Parallel or three bar model. 58
3.5 Dimensionless equilibrium total energy with relative crack length showing the fracture behaviour of compact tension (C(T)) standard specimen geometry, for increasing crack lengths ($\alpha_0 = 0.2$ and $\rightarrow 0.9$), with various spring to initial specimen compliance ratios (C_m/C_{α_0}). 61
3.6 Dimensionless equilibrium load-displacement for series structure with compact tension (C(T)) standard specimen geometry, for increasing crack lengths ($\alpha_0 = 0.2 \rightarrow 0.9$), with various spring to initial specimen compliance ratios (C_m/C_{α_0}). Straight lines plotted from point $0, 0$ to peak dimensionless loads for illustration purposes. 62
3.7 Simple flow chart describing the series, displacement controlled model's algorithm/structure. 65
3.8 Load-Displacement for series structure with compact tension (C(T)) standard specimen geometry, for crack lengths ($\alpha_0 = 0.2 \rightarrow 0.9$), with non-compliant spring. Direct comparison between equilibrium states (Figure 3.6) and displacement control model. Straight lines plotted from point $0, 0$ to peak equilibrium load for illustration purposes. 68
3.9 Load-Displacement for series structure with compact tension (C(T)) standard specimen geometry, for crack lengths ($\alpha_0 = 0.2 \rightarrow 0.9$), with spring to initial specimen compliance ratio $C_m/C_{\alpha_0} = 2$. Direct comparison between equilibrium states (Figure 3.6) and displacement control model. Straight lines plotted from point $0, 0$ to peak equilibrium load for illustration purposes. 69
3.10 Load-Displacement for series structure model under displacement control with compact tension (C(T)) standard specimen geometry, for crack lengths $\alpha_0 = 0.2 \rightarrow 0.9$, with various spring to initial specimen compliance ratios (C_m/C_{α_0}). 70
3.11 Load-Displacement model results under displacement control for series structure with compact tension (C(T)) standard specimen geometry, for crack lengths $\alpha_0 = 0.2 \rightarrow 0.9$, with various spring to initial specimen compliance ratios (C_m/C_{α_0}). 70
3.12 Load-Displacement model results with compact tension (C(T)) standard specimen geometry, for crack lengths $\alpha_0 = 0.2 \rightarrow 0.9$, with spring to initial specimen compliance ratio $C_m/C_{\alpha_0} = 2$. Direct comparison between series structure in displacement control and parallel structure in load control. 71

4.1 Experimental specimens with dimensions. (a) Biaxial cruciform test specimen, (b) Uniaxial beam test specimen. All dimensions in mm, to scale. Thickness for both is 20 mm. Black dot represents the loading location. 76
4.2 Base structure drawing with cross-section, detail on the 10 mm roller positions, radius 7 mm and depth 2 mm. All dimensions in mm, to scale. 77
4.3 Overview of the experimental biaxial setup. 78
4.4 Load-Displacement graph for the uniaxial specimens, under displacement control, on the steel base structure. 80
4.5 Load-Displacement graph for the uniaxial specimens, under displacement control, on the aluminium base structure. 81
4.6 Load-Displacement graph for the uniaxial specimens, under displacement control, on the PMMA base structure. 81
4.7 Fracture path exhibited in all uniaxial specimens. 82
4.8 Load-Displacement graph for the biaxial specimens, under displacement control, on the steel base structure. 84
4.9 Load-Displacement graph for the biaxial specimens, under displacement control, on the aluminium base structure. 84
4.10 Load-Displacement graph for the biaxial specimens, under displacement control, on the PMMA base structure. 85
4.11 Fracture paths exhibited in the biaxial specimens. (a) Single path seen in 10 out of 12 experiments, (b) Branched path. . . . 85
4.12 Finite element simulation; quarter model contour plot of maximum principal stress for (a) Equibiaxial cruciform and (b) Uniaxial beam. A quarter of the roller supports and loading ball can be seen as well. Stress concentrated in the centre darker area. 86
4.13 Load-Strain (longitudinal surface strain) graph for the uniaxial specimens, on all base structures with the grey dashed line being the finite element model's prediction. 88
4.14 Load-Strain (longitudinal surface strain) graph for the biaxial specimens, on all base structures with the grey dashed line being the finite element model's prediction. Brighter grey denotes model with a lowered Young's modulus of 8 GPa. 88
4.15 Two parameter cumulative Weibull distribution of the flexural uniaxial and biaxial strength. Under uniaxial load: $\sigma_w = 23.20$ MPa, $m = 23.29$; equibiaxial load: $\sigma_w = 23.64$ MPa, $m = 22.86$ 90
4.16 Elastic modulus-Strain graph for all uniaxial specimens. 91
4.17 Elastic modulus-Strain graph for all biaxial specimens. 91
4.18 Design of base structure housing bars and specimen made from mild steel. All dimensions in mm, to scale. 94
4.19 Three bar structure configuration close up with PMMA outer bars and a Gilsocarbon graphite compact C(T) specimen. 95

4.20 Load-Displacement graph comparison between the three bar structure with a compact tension C(T) specimen and a single compact tension C(T) specimen. 96
4.21 Load-Displacement graph comparison between the three bar structure with a compact C(T) specimen and a single C(T) specimen. 97

5.1 ASTM Standard E399 compact tension specimen geometry, to scale, showing important geometrical dimensions: crack length, a; width, W; uncracked ligament length, $b = W - a$; and thickness B. Specific dimensions presented in Table 5.1. 107
5.2 Different sized Gilsocarbon graphite compact C(T) specimens. Largest specimen 125 mm in total width. 107
5.3 Overview of the experimental setup. 110
5.4 Close up of the experimental setup. 111
5.5 Load-crack mouth opening displacement, under displacement control, 1/2T size. Specimen 1/2T1 (single load) and specimen 1/2T4 (cyclic load), 14 cycles. 113
5.6 Load-crack mouth opening displacement, under displacement control, 1T size. Specimen 1T2 (single load) and specimen 1T4 (cyclic load), 13 cycles. 114
5.7 Load-crack mouth opening displacement, under displacement control, 2T size. Specimen 2T2 (single load) and specimen 2T6 (cyclic load), 17 cycles. 114
5.8 Load-crack mouth opening displacement, 1/2T size, all specimens. Cycles on the 8 specimens were removed for illustration purposes. 115
5.9 Load-crack mouth opening displacement, 1T size, all specimens. Cycles on the 8 specimens were removed for illustration purposes. 115
5.10 Load-crack mouth opening displacement, 2T size, all specimens. Cycles on the 8 specimens were removed for illustration purposes. 116
5.11 Discrepancy of specimen 1/2T2, single load to fracture. Crack initiation through a pore at about 70 % of peak load. Images of crack at various loads, 70 % of peak load, peak load, load at failure. Hair thin cracks displayed with red lines. 117
5.12 Discrepancy of specimen 1/2T8, cyclic loading to fracture. Pre-existing crack, due to manufacturing or mishandling of delicate specimen. Images of crack at various loadings, 10 % of peak load, load at failure. 117
5.13 Load-crack mouth opening displacement, 1T size. Specimen 1T7, graphical representation of the linear regression performed on the unloading part of the 13 cycles. Black dots represent the chosen windows. 118

5.14 Load-crack mouth opening displacement, 2T size. Specimen 2T8, graphical representation of the linear regression performed on the reloading part of the 15 cycles. Black dots represent the chosen windows. 119
5.15 Intercepts and slopes for the three specimen sizes. 120
5.16 Relative crack lengths-calibrated slopes for 2T, 1T and 1/2T sizes, top to bottom. Graphical representation in dashed line of E399 (5.1) and the inverse (5.3) from the experimental data. . . 123
5.17 Relative crack lengths-calibrated slopes for 2T, 1T and 1/2T sizes, top to bottom. Graphical representation in dashed line of E399 (5.1), the crack lengths from the interpolated calculated compliance and from the optical measurements. 124
5.18 Relative crack lengths from the interpolation of the unloading line compliance-difference between the elastic compliance crack length and the one used in the X axis, for all specimen sizes. . . 125
5.19 Relative crack lengths-K_{R}, 1/2T size. Graphical representation of K_{R} based on E399 K function. Peak cycle loads loads are used with respect to crack lengths from interpolation on the inelastic unloading compliance. 127
5.20 Relative crack lengths-K_{R}, 1T size. Graphical representation of K_{R} based on E399 K function. Peak cycle loads loads are used with respect to crack lengths from interpolation on the inelastic unloading compliance. 127
5.21 Relative crack lengths-K_{R}, 2T size. Graphical representation of K_{R} based on E399 K function. Peak cycle loads loads are used with respect to crack lengths from interpolation on the inelastic unloading compliance. 128
5.22 Crack length extensions $\alpha - \alpha_0$-K_{R}, all sizes. 129
5.23 Load-rolling Pearson correlation coefficient, for specimen 1/2T1. 131
5.24 Brittleness number-apparent fracture toughness for the different specimen sizes, left to right, 1/2T, 1T, 2T. Equivalent frontal zone length $c_f = 6.29\,\mathrm{mm}$ and $K_{\mathrm{I}f} = 1.50\,\mathrm{MPa\,m^{1/2}}$. 132
5.25 Relative crack lengths-calibrated slopes for 2T, 1T and 1/2T sizes, top to bottom. Graphical representation in dashed line of E1820 equation, the crack lengths from the interpolated calculated compliance and from the optical measurements. 133
5.26 Produced R-Curve for the 1/2T size specimens. Crack length estimates based on compliance interpolation. 134
5.27 Produced R-Curve for the 1T size specimens. Crack length estimates based on compliance interpolation. 135
5.28 Produced R-Curve for the 2T size specimens. Crack length estimates based on compliance interpolation. 135

List of Abbreviations

AGR	Advanced Gas-cooled Reactor
ASTM	American Society for Testing and Materials
CMOD	Crack Mouth Opening Displacement
C(T)	Compact (Tension)
CTOD	Crack Tip Opening Displacement
DIC	Digital Image Correlation
EDF	Électricité De France
ESPI	Electronic Speckle Pattern Interferometry
FE	Finite Element
FOIA	Freedom Of Information Act
FPZ	Fracture/Frontal Process Zone
LEFM	Linear Elastic Fracture Mechanics
M(T)	Middle (Tension)
PGA	Pile Grade A
SEM	Scanning Electron Microscope
SEN(B)	Single-Edge-Notched(Bend)
UoB	University of Bristol

List of Latin Characters

A	Cross sectional area of specimen
a	Crack length from load line
a_0	Initial crack length from load line
B	Empirical constant in size effect law
B	Compact (Tension) specimen thickness
b	Thickness of specimen
c	Process zone length
C_{α_0}	Initial specimen compliance
c_b	Bridging zone length
c_f	Process zone length in infinite size specimen
C_M	Outer spring compliance
C_m	Machine compliance
$\bar{d}$	Shape independent size of specimen
d	Characteristic size of specimen
d_0	Empirical constant in size effect law
E	Young's modulus of elasticity
G	Strain-energy release rate or crack driving force
G_{c}	Critical crack driving force
$\tilde{G}_{\mathrm{eq}}$	Critical crack driving force
J	Contour integral, parameter for fracture characterisation in non-linear materials
J_{Ic}	Critical Mode I value of J integral
K	Stress intensity factor

K_f	Stress intensity factor at fracture
K_{Ic}	Critical Mode I stress intensity factor
K_{Q}	Apparent fracture toughness
K_R	Stress intensity factor R-Curve
K_{s}	Steady-state fracture toughness
l_{br}	Length of critical bridging particle, maximum particle length
$\tilde{P}$	Dimensionless load
P	Load
P_f	Probability of failure
$P_{\max}$, P_u	Maximum load
R	Fracture resistance, R-Curve
R^2	Squared regression coefficient
U_e	Elastic stored energy
U_p	Plastic energy dissipation
V_m	Crack mouth opening displacement
W	Specimen width from load line
$Y(\alpha)$	Dimensionless specimen stress intensity function or shape factor
$z_{ll}(\alpha)$	Dimensionless load line specimen compliance function

List of Greek Characters

α	Normalised crack length
α_0	Normalised initial crack length
β	Brittleness number
γ_s	Surface energy
γ_{wof}	Work of fracture
$\tilde{\Delta}$	Dimensionless displacement
Δ	Displacement
Δ_c	Experimental crack mouth opening displacement
Δ_{int}	Displacement measured at the integral knife edge locations
Δ_T	Displacement of structure, total displacement
ν	Poisson's ratio
σ_{br}	Stress due to bridging particles
σ_c	Stress for microcrack formation
σ_f	Failure stress, strength
σ_N	Nominal stress at maximum load
σ_w	Weibull stress
σ_y	Yield strength
τ_N	Shape independent nominal stress at maximum load
ϕ_p	Plastic energy dissipation rate

Chapter 1

Introduction

1.1 Background

Manufactured graphite can be used in the core of a nuclear reactor to moderate fast neutrons emitted after fission of the fuel. The graphite blocks act as a moderator but also as a structural component, providing a channel for the coolant as well as the control and fuel rods. Older Magnox generation reactors, using Pile Grade A (PGA) graphite are now part of UK's nuclear history with Wylfa unit 1, the last operating reactor of its type, shutting down on 30 December 2015. Although the Advanced Gas Cooled Reactors (AGR) currently operating in the United Kingdom share similar core design, with larger bricks receiving the fuel and smaller square bricks carrying the control rods, they use Gilsocarbon graphite [1].

Radiolytic oxidation due to reaction with the CO_2 coolant, combined with neutron irradiation and thus dimensional changes and stresses can lead to the fracture of graphite bricks. This fracture could pose a serious threat to the structural integrity of the core and safety of the reactor as it may affect the function of the brick keying system or the cooling of the fuel.

Public concern to the structural integrity of AGR moderator graphite was first raised in July 2006, where during an inspection at Hinkley Point B bore cracks were found in two graphite bricks, as detailed by the newspaper article [2]. This is not the first incident of graphite cracks noted at Hinkley Point B, as FOIA obtained reports suggest a full length axial crack, the first of its type, was identified during a routine shut down inspection as early as 2003 [3]. Additionally, in 2014, keyway root cracks were reported in one of the cores of

the Hunterston B power station, yet, as stated by the station director, they were well within the expectations and model predictions and thus not affecting the safe operation of the reactor [4].

Despite the general attention, since 2005, life-extensions, which are to be considered at least three years before the scheduled date of closure, on all of the seven operating AGR power stations have been announced from British Energy (EDF Energy since July 2010). Each additional year of operation for the nuclear fleet could provide value in excess of £2.5 billion and prevent about 30 million tonnes of carbon dioxide from being emitted, compared to traditional fossil fuel energy production methods.

1.2 Research Aim & Objectives

The project's aim was to develop a greater understanding of the initiation and mostly of the thresholds of unstable fracture of nuclear graphite and more specifically IM1-24. It expands on the results of earlier projects, undertaken at The University of Manchester [5] and University of Bath [6] with a focus on stability in fracture of virgin graphite.

The objectives of the work were:

- to develop methods of estimating the stability of different specimen geometries and loading conditions or configurations;
- to examine the influence of a variety of factors contributing to fracture instability and assess the validity of linear elastic fracture mechanics techniques;
- to determine the fracture resistance and other fracture parameters of IM1-24 graphite for different sized specimens;
- to compare the above and derive size independent fracture parameters for the material.

1.3 Overview of dissertation structure

Having described the background and the main objectives of the thesis, Chapter 2 provides a brief literature review in the field of graphite fracture, fracture instability, resistance and size effects.

Chapter 3 underlines the parameters that contribute to the instability either by the use of a dimensionless method or an idealised benchmark model. Chapter 4 provides descriptions and results from two set of experiments to quantify the effect of elastic follow-up and to validate the idealised benchmark study.

Chapter 5 provides a detailed description and the results of the experiments performed to quantify fracture resistance. Additionally, effects of size are investigated, from the significant differences exhibited.

Finally, in Chapter 6 recommendations for further work are made and an overview of the conclusions is presented.

Chapter 2

Literature review

This chapter provides a review of the literature on the subjects of fracture in quasi-brittle materials and more specifically graphite. There is a discussion on graphite's basic properties, as well as a relevant background on the studies of fracture instability and resistance and size effects. In the first section, an overview of the structure and manufacturing of graphite is offered. Following, the second section provides relevant background on fracture mechanics and instability. The third section addresses the relevant studies on fracture resistance, including specific experimental procedures and closes with a summary on the broader context. The last section introduces Bažant's size effect and its previous application on graphite and discusses the applicability of statistical size effect in notched/cracked specimens.

2.1 Graphite

2.1.1 Structure

Graphite is an allotrope of carbon. It is composed of carbon atoms arranged in hexagonal arrays, as established by Bernal [7], on the initial proposal of Hull [8]. These atoms, as sets of hexagons, form planes often referred to as graphene sheets. While in plane the atoms are held by strong covalent bonds, with the individual planes held together by much weaker van der Waal bonds (about a hundredth of the strength) [9, 10]. Around 14 % of natural graphite has a rhombohedral cell structure, firstly detected in 1942 [11]. This structure at higher temperatures returns to the typical hexagonal structure [12], which

is the case for all artificial graphite grades as they undergo high temperature graphitisation processes.

2.1.2 Artificial graphite

Limited availability of suitable natural graphite and impurities such as high boron content affecting graphite's neutron absorption properties have made highly pure specifically tailored artificial graphite a necessity [10]. Thus, graphites used in most commercial applications, with nuclear being one of them, are manufactured.

Most artificial graphites are produced with processes based on the Acheson process [13], discovered by Edward Goodrich Acheson while working on methods to produce artificial diamonds. During the process used for nuclear graphite, a coke is used as a filler material. The coke is firstly calcined at about 1200 to 1400 °C to remove moisture and volatile materials while increasing density. After calcination, the coke is milled, screened, blended, crushed and grinded to a specified size and shape. Then the coke particles are bound with a liquid pitch and heated at about 160 to 170 °C while thoroughly mixed. This mixture is then pressed into a mould or extruded, and baked at about 750 to 1000 °C. During this stage the liquid pitch shrinks and is converted to binder coke. This shrinkage as well as the release of the volatiles and impurities in gas form, lead to the formation of a pore network. If the porosity after baking is greater than the one required, pitch is added again impregnating the pores and the baking process is repeated. Although this process greatly reduces porosity, it reaches a certain limit as some of the pores become enclosed and cannot be furtherly impregnated. After the baking process, the mixture is heated to graphitisation temperatures of around 3000 °C and becomes graphite. Some metallic impurities will remain even after graphitisation. The slightest change in the above process or the materials used can produce vastly different grades of graphite.

Pile Grade A graphite

Pile Grade A (PGA) graphite had been the moderator of the now shut down and under decommission Magnox reactors. It is graphitised from a mixture of needle-shaped coke particles of around 1 mm in length and coal tar pitch. Before graphitisation the mixture is extruded, thus exhibiting anisotropy due

to the alignment of the needle particles [14]. The elastic modulus in the direction normal to the extrusion is up to 50 % lower than that in the extrusion direction [15]. Porosity as a result of calcination cracking, gas evolution during the baking process and Mrozowski cracking [16,17] is at about 20 to 25 % with about 4 % being closed [18].

Gilsocarbon graphite

Gilsocarbon graphite is the nuclear graphite used in all of the UK's nuclear reactors currently moderated with graphite. These grades of graphite use Gilsonite asphalt from north-eastern Utah as a filler material after it has been distilled and coked into Gilsonite pitch coke. These filler coke particles are spherical (≈500 µm [19]) and their mixture with coal tar binder pitch is moulded rather than extruded. General isotropic characteristics are exhibited by the IM1-24 grade of Gilsocarbon due to the morphology of the filler particles and the crystallites within them. Porosity, due to the same as above reasons is at about 19 % with about 8.5 % being closed [20].

2.2 Linear elastic fracture mechanics

Based on Griffith [21], for the case of a brittle material loaded in uniform tension, the cracked body is to be regarded as a thermodynamic system. While in an equilibrium, the release of strain energy with crack extension is balanced to create a new surface area. Using the stress analysis done in earlier work by Inglis [22], Griffith showed the failure strength σ_f:

$$\sigma_f = \frac{\sqrt{\frac{2\gamma_s E}{\pi}}}{\sqrt{a}} \quad \text{or} \quad \sigma_f \sqrt{a} = C \tag{2.1}$$

where γ_s the surface energy or the energy consumed for the formation of the surfaces per unit area, with the 2 used as a convention for the creation of two surfaces, E the Young's modulus, a the crack length and C representing a material constant.

Irwin in his work [23, 24], underlying the balance between work done and the energy release rate with extension of the crack, named the strain-energy release rate G after Griffith [25]. He expressed that the energy needed to extend

a crack comes from the rate of loss in the strain energy of the elastic system and by calculating the difference in the area under the stress-strain curves for similar specimens with different crack lengths he was able to estimate the energy needed to extend the crack between these lengths. The critical value for the crack driving force or strain-energy release rate G was called G_c, a material property. The value of G_c was further used as $\sqrt{G_c E}$ based on the observations of Kies that the critical stress for a given crack was dependent on this value, thus giving his name to the stress intensity factor K [26].

$$K_{Ic} = \sqrt{G_c E} \tag{2.2}$$

Irwin [24], based on the work of Westergaard [27] characterising the stress field ahead of a crack, equated G, and by extension K, with the stress ahead of the crack tip which in a simplified expression using (2.2) can be written as:

$$K_I = Y\sigma\sqrt{\pi a} \tag{2.3}$$

with Y being a non-dimensional geometric factor of the specimen found in handbooks [28] and σ interchangeable with load depending on specimen geometry, normally omitting π inside the square root while adding the specimen width and breadth.

2.2.1 Instability

As expressed by Mai and Lawn [29], especially due to its misuse in the case of non-metals, the conditions of failure are not defined by the simple G_c. In the case of Griffith [21], the equilibrium state was unstable as the glass body was uniformly loaded so failure could be identified with G_c, although no insight is provided to whether the extension is stable or not. As shown by Barenblatt [30], many loading configurations exist where failure or the equilibrium states are stable, where, for further extension to occur an increase in the applied driving force is needed. Thus, although G_c is necessary for fracture, an additional instability requirement must be used.

$$G - R = 0 \quad \text{or} \quad G = G_c = R \tag{2.4}$$

(a) Displacement control fracture

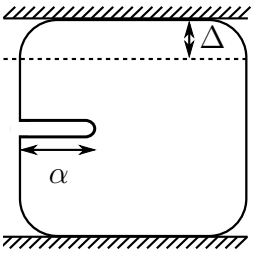

(b) Fixed displacement

Figure 2.1: Displacement control or fixed displacement, (b) reproduced from Anderson [31]

Equation (2.4) above describes the Griffith equilibrium at the point of crack extension with G being Irwin's energy release rate characterising the force driving the crack and R, for the ideally brittle material, the free surface energy $2\gamma_s$ increment. To determine whether the fracture is stable or not, the derivative of rate needs to be used and compared to zero.

$$\partial G/\partial A < \partial R/\partial A \quad \text{(stable)} \tag{2.5a}$$

$$\partial G/\partial A > \partial R/\partial A \quad \text{(unstable)} \tag{2.5b}$$

As can be understood from above, the rate of crack driving force is clearly a factor to stability. Prior to initial cracking ($G = G_c = R$), the rate of loading or the way the load is transferred to the specimen has no effect to the elastic strain energy of the system and thus no effect to its instability criterion (2.5). However, upon propagation, the energy available for the crack comes from work done by external forces and by the elastic strain energy stored and released from the system.

Under displacement control (Figure 2.1), no extra work is done from the applied load making it generally more stable than load control, as can be seen in Figure 2.3. For most specimen geometries the load drops to accommodate the increase in compliance with crack extension, decreasing the strain energy as well [32]. This underlines the importance of a sharp notch. Blunter notches will require higher load for initial fracture [33] and thus higher strain energy, making a specimen behave in a more unstable manner as the compliance function remains the same.

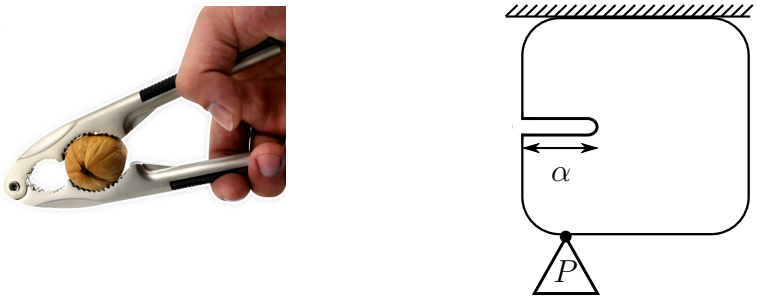

(a) Load control fracture (b) Fixed load

Figure 2.2: Load control or fixed load, (b) reproduced from Anderson [31]

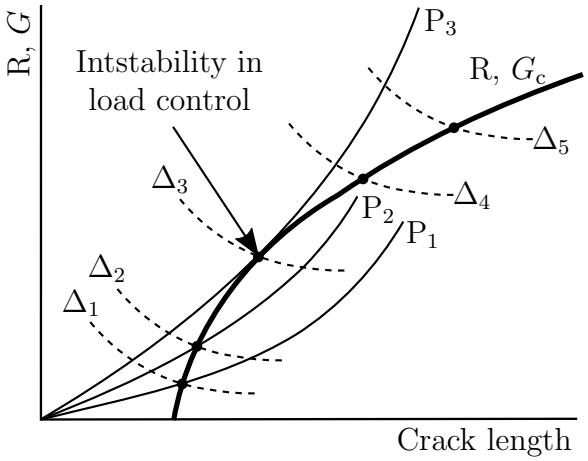

Figure 2.3: R curve and driving force comparing load control P and displacement control Δ, reproduced from Anderson [31].

Under load control (Figure 2.2), due to the contribution of the external load, a net increase in supplied strain energy and subsequently crack driving force is exhibited, leading to generally more unstable behaviour. As can be seen in Figure 2.3, for the case of a rising G_c or R-curve with respect to crack length, stability is lost for the fixed load P_3 where the increasing driving force is tangent to the G_c curve. For the case of displacement control Δ_1 to Δ_5, the displacement must increase for further crack growth, as the driving force rate is negative [31].

2.2.2 Structure compliance

Characteristics of testing machines can affect the boundary conditions set by the operator thus introducing experimental error. All testing machines will deflect under load, while storing strain energy, overestimating the displacement

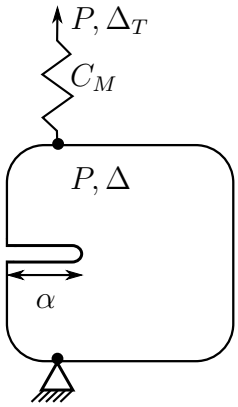

Figure 2.4: Structure with finite compliance, reproduced from Hutchinson and Paris [34].

in tension specimens and thus making clip gauges and extensometers a necessity. The energy stored in the testing machine will become available to "feed" the crack propagation (from the change in specimen compliance) and can introduce instabilities on stable specimen geometries. Clearly, stiffer machines are less likely to produce instabilities as they contain less energy for a given load [32].

Although problems can arise from compliant testing machines, one can analyse the equivalent in Figure 2.4 to account for their behaviour. Hutchinson [34] based on a report by Paris [35] showed for Figure 2.4 (derivation in appendix A):

$$\left(\frac{\partial G}{\partial a}\right)_{\Delta_T} = \left(\frac{\partial G}{\partial a}\right)_P - \left(\frac{\partial G}{\partial P}\right)_a \left(\frac{\partial \Delta}{\partial a}\right)_P \left[C_M + \left(\frac{\partial \Delta}{\partial P}\right)_a\right]^{-1} \tag{2.6}$$

where P the load (series load acting on specimen and spring), Δ the load point displacement of the specimen, Δ_T the displacement of the structure and C_M the compliance of the spring. The compliance of the spring defines the proximity to either load $C_M \to \infty$ (dead load) or displacement control $C_M \to 0$ (rigid test machine) thus providing a tool to evaluate instability in mixed boundary conditions.

The importance of understanding the effects of additional available strain energy is not limited to the case of a compliant testing machine. System and specimen compliance, or relative stiffness effects on instability will be examined in the next chapter following the works of Mai and Lawn [29], Sakai and Inagaki [36] and Bažant and Becq-Giraudon [37].

2.3 Fracture resistance

Although linear elastic fracture mechanics are adequate in characterising failure in brittle materials, this is not the case for a quasi-brittle material such as graphite. The failure mechanisms exhibited in these materials absorb some of the potential energy during loading making the energy for crack propagation higher than the energy for crack initiation [38,39]. Subsequently, even for load control, fracture of graphite can be stable until the energy absorption reaches a steady state, making the study of these mechanisms necessary for a better understanding of graphite's fracture behaviour.

Relevant studies on fracture resistance as well as the mechanisms affecting it are presented. The purpose of this section is not to cover the whole subject of fracture in graphite, which has been already reviewed in great detail [33, 40, 41], but to provide the background and the details of the studies done to measure the fracture resistance of IM1-24 and other grades, and underline their influence in the thesis.

2.3.1 Sakai 1983

This study by Sakai *et al.* [42] describes a graphical method to determine various fracture parameters from a load-displacement curve, based on the assumptions that the kinetic energy of the body is negligible due to the slowly applied load and that the residual elastic energy is negligible. Elastic and inelastic parameters $\widetilde{G}_{\mathrm{c}}$, R, ϕ_p and J_R are graphically defined. Based on previous work [24, 43, 44], the non-linear fracture toughness $\widetilde{G}_{\mathrm{c}}$ is described as

$$\widetilde{G}_{\mathrm{c}} = \frac{\partial}{\partial A}\left(W - (U_e + U_p)\right)_{\mathrm{c}} \tag{2.7}$$

the crack growth resistance R as

$$R = \frac{\partial}{\partial A}\left(W - U_e\right)_{c} \tag{2.8}$$

and the plastic energy dissipation rate ϕ_p as

$$\phi_p = \frac{\partial U_p}{\partial A} \tag{2.9}$$

with ∂A being the increment of the cracked surface area, W the work applied to the specimen, U_e the elastic stored energy and U_p the plastic energy dissipation.

In Figure 2.5 a specimen with a crack length a and a surface area A is loaded under displacement control up to point B. The initial crack has propagated and it is assumed that onwards there are no energy dissipation mechanisms related to the initial crack tip formation and propagation. If the specimen following the loading path to point B was unloaded, it would unload to point C in a straight line, assuming no plastic deformation or crack growth would occur during the unload, with point C being offset from O due to the plastic deformation during the loading OB. The specimen is loaded from point B to D, with the crack advancing quasi-statically by Δa (with the newly cracked area being ΔA). If the same unloading sequence as BC is applied to point D the specimen will intersect with the axis at the new point E. This point is offset from point C by Δu_p representing the additional plastic deformation during Δa. The area $BCDE$ represents the energy consumed for the propagation of the crack and the newly cracked area ΔA and with the division of the two representing R.

$$\frac{\Delta \pi_R}{\Delta A} = \frac{\Delta}{\Delta A} \left(W - U_e\right)_c \equiv R \tag{2.10}$$

The crack-growth resistance can be related to the work of fracture as,

$$2\,\gamma_{wof} = \frac{\int_0^S R\,(A)\,dA}{S} = 2\,\gamma_e + 2\,\gamma_p \tag{2.11}$$

with a graphical representation of the separation of γ_e and γ_p in Figure 10 of the original work. The area $BCDE$ can be portioned by shifting the line DE to the left, by the additional deformation Δu_p. The first one is area BCF or $\Delta \pi_G$

$$\frac{\Delta \pi_G}{\Delta A} = \frac{\Delta}{\Delta A} \left(W - (U_e + U_p)\right)_c \equiv \widetilde{G}_c \tag{2.12}$$

and the second one is area $BFCED$ or $\Delta \pi_p$, as $R = \widetilde{G}_c + \phi_p$,

$$\frac{\Delta \pi_p}{\Delta A} = \frac{\Delta U_P}{\Delta A} \equiv \phi_p. \tag{2.13}$$

The evaluation of J_R follows the same principle as the evaluation of $\widetilde{G}_c$, with the main difference being the curved loading-unloading paths as seen in

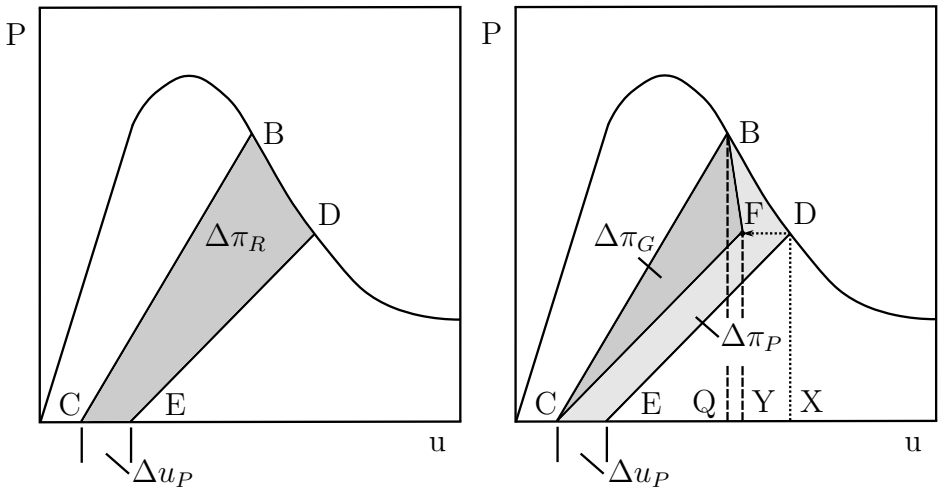

Figure 2.5: Schematic of loading and unloading paths BC, DE used to graphically determine fracture parameters, reproduced from Sakai *et al.* [42].

Figure 2.6. The curved paths according to Sakai are due to "energy dissipated by plastic deformation during the artificial loading-unloading" with the loading path being above the unloading. Based on Jenkins [45], during this hysteresis, the graphite remains elastic as subsequent cycles between the same stress limits produce identical loops. The curvature of these paths is a characteristic of graphite behaviour and no further explanations can be found in the bibliography.

The isotropic IG-11 graphite was used in the experimental part of the work. The faces of the chevron notched compact tension specimens were glued to two steel plates connected to the testing machine in order, as specified by Sakai, "to avoid plastic energy dissipation related to the normal slippage and indentation at the loading points". The specimen was loaded and unloaded after each subsequent Δa at a rate of $0.02\,\mathrm{mm\,min^{-1}}$. The crack increments needed for the calculation of R were determined by the compliance method as can be seen in Figure 6 of the original work.

The results of the experiment show falling crack resistance and fracture parameters $\widetilde{G}_\mathrm{c}$, ϕ_p and J_R with crack growth, contrary to the rest of the studies that demonstrate a rising-plateau or a less steep rising behaviour. More specifically, Kim *et al.* [46] observed a "rising R-curve behaviour" by the K_R values for IG-11, and studies for IG-110, a more purified version of IG-11, show a slight initial rise and plateau region [18]. As discussed by Hodgkins [5], this fall may be due to the unusual way the specimen was loaded with the use

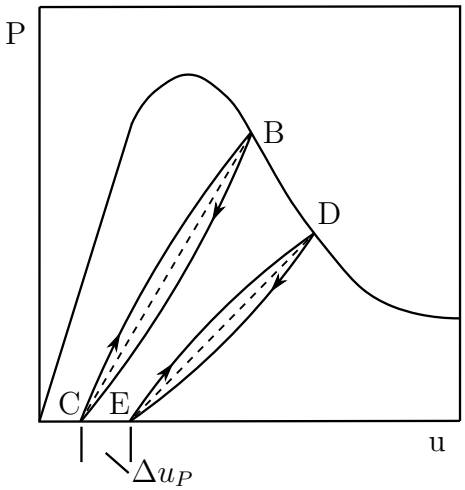

Figure 2.6: Curved loading and unloading paths BC, DE used to graphically determine J_R, reproduced from Sakai *et al.* [42].

of steel plates, as well as the shape of the ligament produced by the chevron notch, both of which affect the elastic compliance of the specimen.

Due to the above and the difficulties in determining crack and area increments for the calculation of R, as well as bridging zone inconsistencies, a specimen with uniform ligament thickness is suggested.

2.3.2 Sakai 1988

In this study, Sakai *et al.* [47] examined the contributions of micro-mechanical mechanisms to the rising R curve behaviour based on previous studies of ceramic materials [48–50]. Two mechanisms are underlined, the microcracking ahead of the crack tip [51] and the crack or grain bridging in its wake [52], and examined through the experimental procedure.

Compact tension specimens made from the isotropic IG-11 graphite were used with notches ranging from $a_0/W = 0.3$ to $a_0/W = 0.9$. The specimen design was according to ASTM-E399 standard from 1981 [53]. The notches were initially machined by a 0.8 mm thick diamond wheel and then extended by 1 mm using a razor blade resulting in a notch tip radius of about 10 µm. The specimens were loaded at a rate of $0.05\,\mathrm{mm\,min^{-1}}$ with the displacement being measured at the load line by a clip gauge and the crack extension with a travelling microscope.

The specimens were unloaded and renotched following a crack extension

of about 2 mm, while monitoring the K_R behaviour under a quasi-static crack growth. The renotching was done in order to ensure the full removal of any bridging particles in the wake of the crack tip. The K_{R} values were calculated using (2.14) from ASTM-E399 [53], with $Y\,(a/W)$ the specimen geometry factor of the standard, P_c the fracture load, B the breadth and W the width of the specimen.

$$K_R = \frac{P_c}{B\,W^{1/2}}\,Y\left(\frac{a}{W}\right) \tag{2.14}$$

The results, as can be seen in Figure 5 of the original work, show a rapidly rising K_{R} in the initial stage of every renotched crack length, even at $a_0/W = 0.9$, ending with a falling behaviour as the crack extended close to the back side of the specimen. The K_{c} at crack initiation also showed a similar falling behaviour for $a_0/W > 0.6$ (uncracked ligament of about 16 mm) due to the same process.

The two mechanisms considered responsible for the behaviour of the R-curve were also examined with the use of scanning electron microscopy. The scans show the formation of microcracks in the frontal process zone as well as their partial closure in the wake of the crack, evidence of residual strain in the wake region. The existence of grain bridges can also be observed with scans of the rough fracture surface as seen in Figure 7 of the original work. Comparisons between the strain attributed to the partial closure of microcracks in the wake of the crack and the grain bridging tractions, as well as the validation of the experimental renotching results, show the grain bridging as the most dominant toughening process, also validated by the work of Ahlborn *et al.* [54].

The bridging stress due to the development of the crack bridging zone was calculated using (2.15), with the assumption of the stress being uniformly distributed through the length of the zone, based on the Dugdale model [55]. K_c^{init} being the fracture toughness at crack initiation, σ_{br} being the bridging stresses and a_{br} the length of the bridging zone, which is assumed to be same as the crack extension up until the start of the plateau. The bridging stress which was found to be approximately 12 MPa, about half of the tensile strength of the graphite tested, showed agreement with the characteristic stress for microcrack formation ($\sigma_c \approx 15$ MPa), a value which is not cited in the original work.

The critical bridging particle length was also estimated using (2.16), based on the equation for the calculation of the crack opening displacement [56] and thus although not directly stated, calculating the maximum particle length in order to have an interaction between the surfaces. The resulting value

of $l_{br} \approx 12\,\mu m$ agrees with the dimension of the coke fillers of the specific graphite grade ($15\,\mu m$). Based on the above, Sakai *et al.* argue that each bridge comprises of a single coke particle.

$$K_{R(n)} = K_c^{init} + 4\,\sigma_{br}\left(\frac{a_{br}}{2\,\pi}\right)^{1/2} \tag{2.15}$$

$$l_{br} = \frac{8}{E}\left(\frac{a_{br}}{\pi}\right)^{1/2}\left(\frac{K_c^{init}}{\sqrt{2}} + \sigma_{br}\left(\frac{a_{br}}{\pi}\right)^{1/2}\right) \tag{2.16}$$

2.3.3 Ouagne 2002

Ouagne, as part of his PhD [6, 57], performed experiments based on the Sakai load-unload method [42], on IM1-24 and PGA graphites. Compact tension specimens of two different sizes were used, although the presented results throughout the work were from the smaller sized C(T). The specimen design and more particularly the height and the breadth of the specimens were not according to the current, at the time of the work, but to the older ASTM-E399 standard from 1981 [53], same as the one used in the work done by Sakai [47]. Although not perfectly scaled (larger C(T) specimens about 150 % of the smaller in almost all dimensions), both of them had an initial crack of 20 % of their width ($a_0/W = 0.2$). Both sizes of specimens were loaded at a rate of $0.5\,mm\,min^{-1}$ with load and displacement measured at a rate of 2 Hz, with the crack mouth opening displacement also being measured at the same rate with a clip gauge.

The crack lengths-extensions were either measured manually with a graduated scale over the width of the specimen, which was sprayed red to enhance contrast, or in some cases with the use of a video camera. Ouagne, argues the validity of the compliance method in evaluating the advancing crack length, as the method showed significant deviation between the measured and the calculated crack lengths on lengths of over 25 mm ($a/W > 0.5$, for the case of the smaller C(T)), also discussed by Fett in earlier work [58]. This above method, also used in [59, 60], can be seen in (2.17), with a the crack length, C the compliance, W the width of the specimen and n the current unloading cycle. Deviations between crack length measurement methods and the proposed method used in this work will be examined in section 5.3.2 and discussed in section 5.4.2.

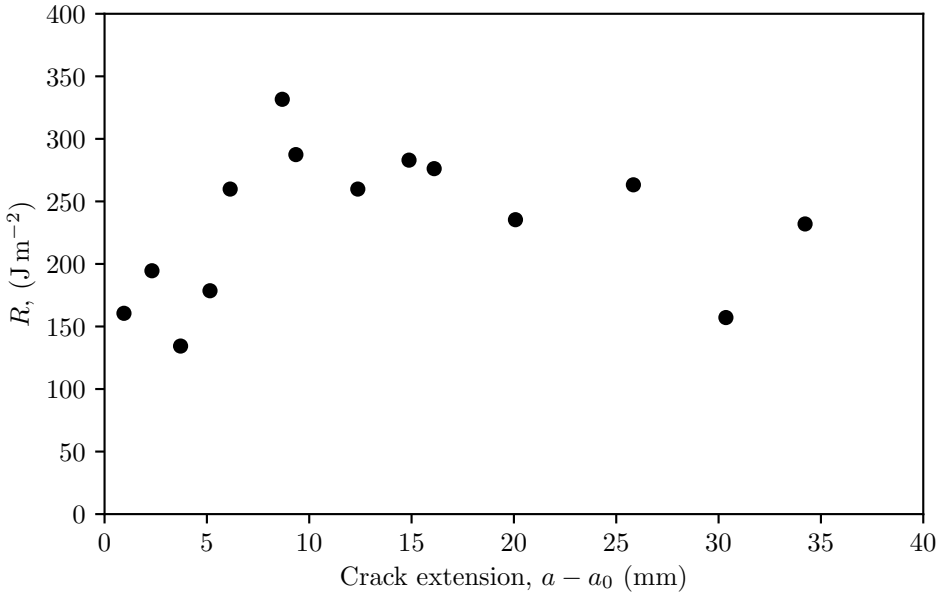

Figure 2.7: R-curve values for IM1-24 compact tension (C(T)) specimen, crack increment measurements taken with video camera, reproduced from results of Ouagne *et al.* [57]

$$a_n = a_{n-1} + \frac{W - a_{n-1}}{2} \frac{C_n - C_{n-1}}{C_n} \tag{2.17}$$

For the determination of R, Ouagne used Sakai's method found in (2.10). The K_{R} values were calculated based on (2.14). The J_{R} values were calculated based on the methodology in ASTM-E813-81, currently E1820-15a [61] as,

$$J_R = \frac{U_J\,(n)\, f\,(a\,(n)\,/W)}{B\,(W - a\,(n))} \tag{2.18}$$

where U_J the area under the load-displacement graph up to the peak load of each cycle and $f\,(a\,(n)\,/W)$ a correction factor based on specimen geometry. For the work of fracture γ_{wof} and plastic energy dissipation ϕ_p (2.11) and (2.13) were used.

The results for the R-curves of the smaller compact tension specimen, although quite scattered, show a rise in the initial 10 mm of the crack extension, followed by a relative plateau region for about 20 mm and then a decrease for the remaining crack length. This can be seen in Figure 2.7, where measurements for the crack length increment were taken with a video camera.

The bridging stress due to the crack bridging zone was evaluated using (2.15)

and the bridging particle length using (2.16). The estimation of the bridging stresses for the two grades of graphite are significantly lower compared to their tensile strength [62]. More specifically, 2.9 MPa compared to 14 MPa for the IM1-24 and 2.6 MPa compared to 11 MPa for the PGA. The bridging particle sizes for the two grades were also found to be much smaller compared to the filler particles and approximately the same value, thus partially validating Allard's observation on grains not being bridging constituents in anthracite materials [59].

Analysis of the K_{R} graphs showed that crack bridging contributed approximately 0.4 MPa $\mathrm{m}^{1/2}$ to the toughness of both graphites as well as about 20 % to the work of fracture. The above analysis was based on the assumption that the initial crack length α_0 was small enough to accommodate the initial rise and plateau without interaction with the back face of the specimen while being in these two regions. PGA, compared to the IM1-24, showed higher energy absorption during the development of the crack bridges, presumably due to its coarser microstructure, as stated by the author. Fracture toughness K_{R} was found to be about 40 to 50 % greater for IM1-24 and work of fracture γ_{wof} about 20 % greater for PGA. More specifically, during the rising R part of the fracturing process the PGA γ_{wof} was found to be about 50 % greater than that of the Gilsocarbon. This illustrates the differences between the two grades, with PGA being more resistant due to the higher degree of plastic energy dissipation mechanisms such as microcracking and crack bridging and to a lesser extent crack branching [63]. The above underlines the importance of the use of both energy and stress crack growth resistance estimations and is to be examined further.

2.3.4 Hodgkins 2006

Hodgkins, as part of his PhD [5, 64], examined the mechanisms responsible for the resistance behaviour of IM1-24 graphite. The performed experiments were based on the Sakai load-unload method [42], coupled with the use of X-ray microtomography (XRμT) and Electronic Speckle Pattern Interferometry (ESPI), for the first loading cycles of the method.

This study used compact tension specimens that were modified from the standard as to maximise the spatial resolution of the X-ray microtomography. The specimen thickness was decreased from 50 mm of the early set of tests

to 10 to 30 mm for the latter ones and the width of about half of them was increased in order to allow cracks to extend up to 100 mm. Also, in order to control the tendency for cracks, specifically for the case of the longer and thinner specimens, to propagate out of plane of the notch, single or double side grooves were added. The specimens were loaded at a rate of $0.05\,\mathrm{mm\,min^{-1}}$ while measuring load and load line displacement.

The crack lengths-extensions were measured manually with a vernier gauge and also with the use of digital surface photography, that was also validated with ESPI, over the first 10 mm of the extension. The author also examined theoretical compliance methods for crack measurement such as the one proposed by ASTM-E1820 as well as the theoretical compliance method found in (2.17).

Results showed an R-curve with rising resistance over the initial 10 to 15 mm of crack propagation, followed by an almost plateau region with a resistance slowly increasing over the next 15 to 20 mm. Following these two regions, the shape of the curve varied with the different specimen geometries. The shorter specimens exhibited a fall as seen in the previous studies [47, 57]. For the case of the longer specimens, there was a subsequent rise following the plateau region in over 40 mm of crack growth. The above can be seen in Figure 2.8.

X-ray microtomography observations showed a region of microcracks 10 mm ahead of the crack tip, which remained partially open once in its wake and under load. Following the removal of the load, all microcracks closed to the point of not being visible by the X-ray. Bridges were also observed up to 40 to 45 mm, far greater than any previous studies, behind the crack tip with the majority of these being in the matrix of the material. Hodgkins, based on these observations argues the difficulty of estimating a maximum length for the bridging particles and the zone itself. Subsequently, the possibility of cracks in the graphite bricks being bridged through their entire length is also expressed.

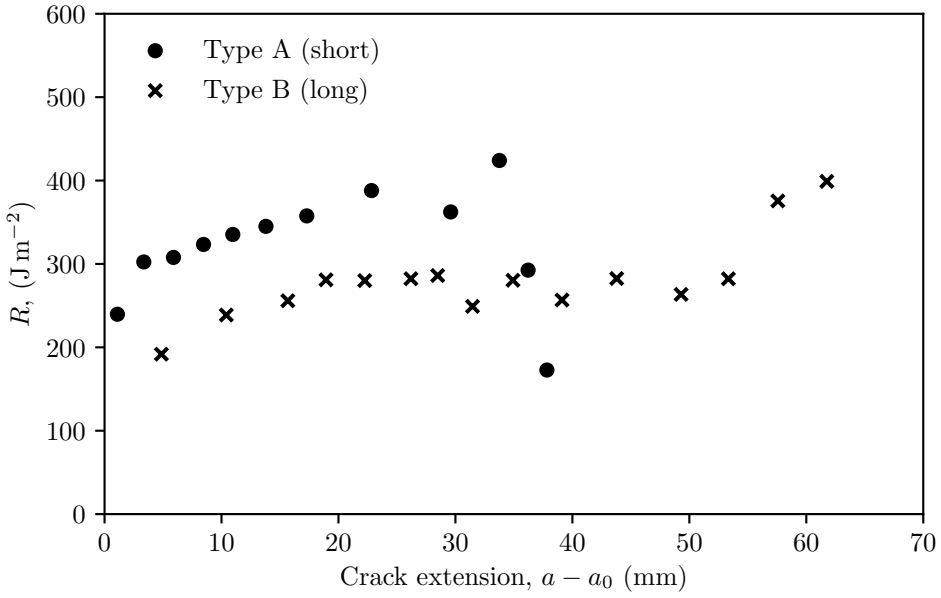

Figure 2.8: R-curve values for Type A (short) and Type B (long) IM1-24 non-standard compact tension (C(T)) specimens, crack increment calculation from compliance, reproduced from results of Hodgkins [5].

2.3.5 Other studies

Fazluddin 2002

Fazluddin, as part of his PhD [18], used SEN(B) and C(T) specimens to measure the linear elastic fracture properties ($K_{\mathrm{Ic}}, G_{\mathrm{Ic}}$) of 3 graphite grades (IM1-24, IG110, UcarC), based on an equivalent single load cycle. The specimens were loaded at a rate of $0.05\,\mathrm{mm\,min^{-1}}$ and the crack lengths were measured using a potential drop method, the theoretic linear elastic compliance and in a handful of cases optical methods. K_{R} - crack length curves for both specimen types of IM1-24 using the elastic compliance and optical methods showed some discrepancies, presumably due to the overestimation of crack length in the elastic compliance method or the uncertainty of the elastic modulus, but with the common, although not particularly distinctive trend of the typical 3 stages of the curve.

A falling K_{R} curve was exhibited by the curves with the ACPD (alternative current potential drop) crack measurement as the crack lengths were greatly underestimated due to contact "shorting" in the bridging zone. These variations between the ACPD measurements and the two other methods were

used to approximate the length of the bridging zone as can be seen in Figure 7.4 of the original work. Results of these approximations show 3 stages of the bridging zone, a rise, a small plateau ($0.65 \leq a/W \leq 0.85$) and a fall in both specimens. At the plateau region, the bridging zones for IM1-24 were estimated at 6 to 8 mm and 2 to 2.5 mm for the compact tension and the SEN(B) respectively. Despite the assumption that the bridging particles were uniformly distributed, the results point out the differences in the bridging zone sizes and thus the R or K_{R} curves between specimen geometries.

Li 2013

Li *et al.* [65] examined the fracture behaviour of NBG-18, a newer molded graphite grade with a medium sized grain ($\sim$1.6 mm) [66]. Three-point bend tests on single edge notched beams of 3 different sizes were performed coupled with digital image correlation and acoustic emission sensors. The specimens were close to the standard [67] with an increased width, W and breadth, t, presumably for ease of crack length measurements and a reduced span to width ratio S/W of $4-5$. The a_0/W ratio of 0.4 was kept constant between specimen sizes. The specimens after an initial stroke or displacement control of 0.005 to 0.02 mm min^{-1} were loaded in CMOD control at stroke control equivalent rates of about 0.08 to 0.15 mm min^{-1}, varied with specimen size. The K_{Ic} or K_{R} values were calculated based on a single load cycle to failure, with the use of the ASTM-D7779 [67] equations (for $S/W = 8$), found in (3) and (4) of the original work, which can be used on specimens with $0.35 \leq a/W \leq 0.6$ and $5 \leq S/W \leq 10$, not for the experimental span to width ratio [67]. Pictures of the speckle sprayed surface were taken at a rate of 7.5 Hz and based on the spacial resolution of the each specimen, separate ϵ_{th} threshold values were chosen to measure crack length through DIC.

The K_{R} - crack length curves were in agreement with the typical 3 stage R-curves, with the two largest size groups exhibiting a length of 8 to 9 mm for the third stage and thus the FPZ based on the previous assumptions. Results for the smallest of the group (initial ligament of 6 mm) showed a much shorter length for the 3 stages for the curve, exhibiting the same behaviour as presented by Sakai in the renotching C(T) experiment [47]. K_{Ic} values at peak load showed a clear size effect, with an increase of about 33 % in K_{Ic} from the smaller to the largest specimen and the Weibull modulus m was

calculated for each specimen size, showing increasing variability for a decrease in specimen size. Additionally, size effect analysis was done based on Bažant's size effect law and although $\bar{d}$ was mistaken as the specimen width, $K_{If} = 1.76\,\mathrm{MPa\,m^{1/2}}$ and $c_f = 9.74\,\mathrm{mm}$ were calculated. Interestingly, K values corresponding to the initial AE event at each group were very consistent (0.85 to $0.88\,\mathrm{MPa\,m^{1/2}}$), indicative of the material's behaviour. Both Bažant's size effect and the applicability of Weibull's theory will be discussed in the next section (2.4 and 2.4.2).

2.3.6 Summary

Past studies and experimental procedures on fracture resistance and relevant fracture properties have been presented. These studies show the plethora of measuring techniques but also reveal their limitations.

K_R or stress based methods, although much simpler in execution, are not without shortcomings. The single load to fracture calls for excellent crack measurement methods such as a high speed camera or a travelling microscope [47,68], which can be prone to misinterpretation due to irregular crack tip patterns [69,70] and cannot be reliant upon linear compliance methods [57,71] for the case of nuclear graphite [57,72]. Additionally, the specimen tested must follow the requirements of the appropriate standards [5, 65] as else the use of the K_I or K_R function must be accompanied by FE analysis to determine the new functions. Fracture instability can also pose a challenge as the load points picked may have little to no use and evaluating the threshold of instability, coupled with the available crack measuring techniques can be erroneous [65].

The energy based method for the estimation of the R-curve [42] answers most of the problems presented above, albeit introducing others. During the machine unloading after a crack extension, a necessary requirement for its validity, damage or other irreversible processes may act upon the bridging particles thus affecting the behaviour of which they are mostly responsible for [42, 47]. Thus, a partial unload up to a percentage of the peak cycle load ($\sim$10 %) during this process is crucial.

Results from the past studies show a clear rising crack resistance, especially in the case of IM1-24 for the first 8 to 15 mm of crack extension for standard and modified compact tension specimens [5, 18], although some of them quite scattered [6, 57]. After the initial rise however, results become quite diverged

with some exhibiting a clear plateau region [6, 57] and others a continuous but much shallower rise [5, 18, 72]. On the third stage results become quite irregular with most energy based measurements showing a clear fall [5, 6, 18] and some K_{R} curves exhibiting a very steep rise [6, 57, 59] presumably due the a_0/W limitations of the K function used in the calculations, underlying another shortcoming of the stress method, also noted in the works of Mazzei *et al.* [73, 74].

Other than the fracture properties and especially fracture resistance, the above studies draw attention to the mechanisms responsible for the fracture behaviour of graphite. The onset of the apparent main crack extension, even minimal, is generally at a lower load than the peak [47]. A damaged zoned (or fracture process zone, FPZ) ahead of the crack tip can be responsible for that effect by shrouding the crack as it forms, with the formation of well-documented microcracks, at approximately 50 to 60 % of the fracture load [5, 47].

The rising resistance behaviour exhibited at the first stage of the R-curve can be attributed to the frictional contact caused by the formation of a bridging zone in the cracked area [18, 47, 57]. The above was observed by thorough examination of the surface with a travelling microscope [42,47] and with X-ray microtomography [5, 64]. This is consistent with previous observations where renotching a specimen, thus destroying any bridging that might have occurred at the crack wake, would produce a similar rising resistance [47]. Although bridges may be formed in graphite grades by finer filler particles, such as the IG110 or the similar IG11 as exhibited in earlier studies [47], this is not the case for coarser graphite grades. Measured bridge particles from studies in PGA and IM1-24 show them being much smaller than whole filler particles and thus compromising of broken ones [5] or parts of the binder phase [57].

As the bridging zone reaches a stable state after several millimetre of initial crack extension, the R-curve reaches its plateau value [18]. The extension needed to reach the stable state, based on the above studies, was found to be 7 to 15 mm for the compact tension specimen [18, 57, 64] and 0.5 to 2.5 mm for the SEN(B) [18, 65], underlying the significance of specimen size, geometry and initial crack length. Crack growth during this steady state is associated with the stable propagation of both the damage zone ahead and the bridging zone in the wake of the crack tip.

The falling resistance in the last stages of the R-curve is believed to be due to the interaction of the damaged zone ahead of the crack with the back face of the specimen [47]. As the density of damage is decreased further from the crack tip, progressively less energy is required to propagate the crack through the immobile damaged zone [72]. During the last stage of the process further resistance reduction is expected as the crack and the shrinking bridging zone propagate through the immobile damage zone. Based on the above, this interaction between the damaged zone and the back face of the specimen, can provide the means of calculating its length, unfortunately with added uncertainty due the limitations of the fracture resistance methods explained earlier [65]. The size of the FPZ can vary with specimen geometry and is reported, for IM1-24, to be approximately 5 to 10 mm for the compact tension specimens [5,6], 2 to 3 mm for the SEN(B) specimen [18] and 8 to 10 mm for the double torsion specimen [72]. Sakai and Kurita [75] state that only when the width and the length of the fracture process zone are small compared to the specimen, the R-curve becomes a material constant.

The differences exhibited by different sized specimens, either of the same or various types, will be explored in the next section.

2.4 Size effect

The mechanisms that contribute to graphite's fracture behaviour and especially the formation and progression of the process zone as well as the efforts to measure its size, underline an important aspect of quasi-brittle materials. Although the process zone size is, in infinite size specimens, a material constant directly defined by the inhomogeneities and properties of the microstructure [76], its intricacies in different sizes and geometries of specimens as well as during loading stages need to be examined.

The premise of the size effect law as outlined below is that when the size of the zone is relatively small to the dimensions of the specimen or the structure, LEFM (linear elastic fracture mechanics) is adequate in characterising the failure through K_{Ic} and G_{c} as nearly the entire structure is in an elastic state [77]. In the case where the zone covers most of the specimen, strength of materials may be a more accurate descriptor of failure. For the case where the process zone is somewhere between these two extremes, traditional fracture

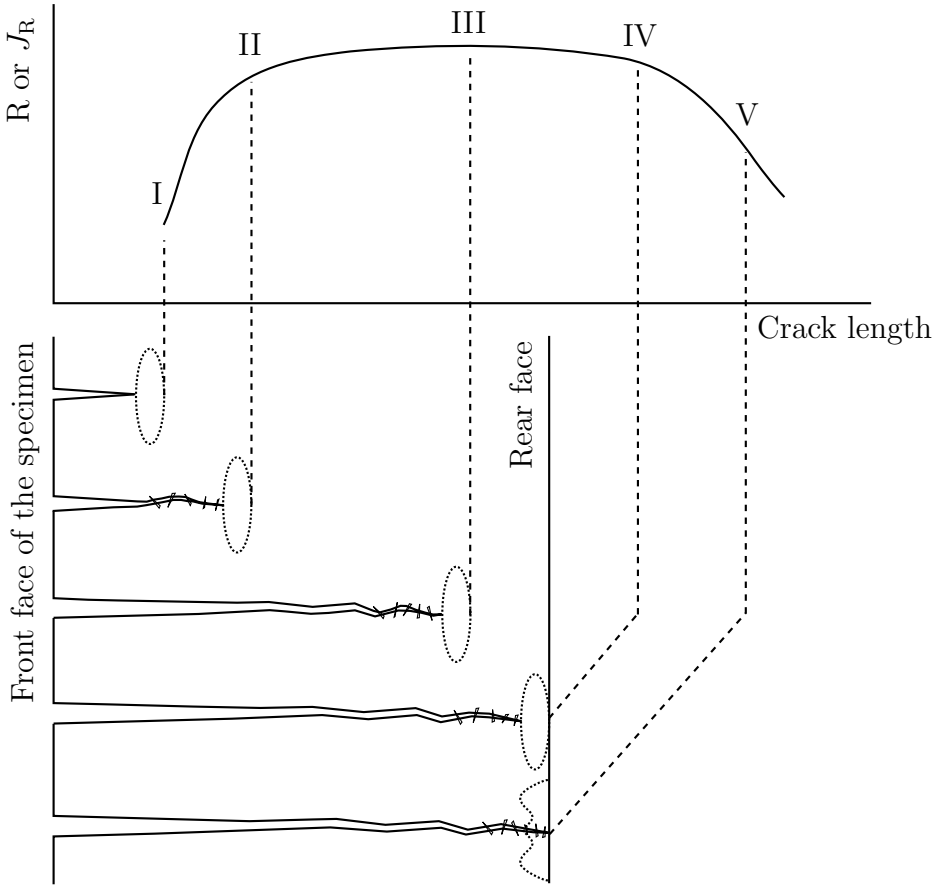

Figure 2.9: Diagram of the R-curve and the mechanisms associated with each stage to crack length increase, reproduced from Hodgkins [5].

mechanics offer no solution and the size effect due to the process zone must be considered [78, 79].

Size effect, as described by Bažant, is the seeming reduction in nominal strength with increase in size on geometrically identical specimens and formulated as follows, based on the assumption that a crack and subsequently a fracture process zone of finite size is formed in a stable manner.

The nominal stress at maximum load P_u, in geometrically similar specimens with an initial crack can be written as

$$\sigma_N = c_n \frac{P_u}{bd} \text{ (for 2D)} \quad \text{or} \quad \sigma_N = c_n \frac{P_u}{d^2} \text{ (for 3D)} \tag{2.19}$$

where b the thickness of the specimen in a two dimensional similarity, thus being the same for all different sizes, d the characteristic size of the specimen and c_n a factor introduced for convenience, a constant for geometrically similar specimens.

Although, under a stress criterion, failure for geometrically similar specimens exhibits no size effects this is not the case for fracture mechanics. Potential energy of the form, for two dimensional similarity, $U = (\sigma^2/2E')\, bd^2 f(\alpha)$, where $\sigma = c_n P/bd$, $f(\alpha)$ a function of the relative crack length and dependant on the geometry of the specimen, $\alpha = a/d$, a the crack length, $E' = E$ for plane stress and $E' = E/(1-\nu^2)$ for plane strain, E the Young's modulus and ν Poisson's ratio. The energy release rate is $G = -(\partial U/\partial a)/b = -(\partial U/\partial \alpha)/bd = -d(\sigma^2/2E')\, f'(\alpha)$, from which,

$$G = \frac{P^2 g(\alpha)}{E' b^2 d} \tag{2.20}$$

$$K_I = \sqrt{GE'} = \frac{P k(\alpha)}{b\sqrt{d}} \tag{2.21}$$

where K_I the stress intensity factor, $f'(\alpha) = df(\alpha)/d\alpha$, $g(\alpha) = -f'(\alpha)\, c_n^2/2$ and $k(\alpha) = (g(\alpha))^{1/2}$, with $k(\alpha)$ the dimensionless, geometry specific, function found in handbooks [28, 31, 32]. From (2.21) above, it is shown that for LEFM, $\sigma_N \propto d^{-1/2}$.

For the case of quasi-brittle materials, where $a = a_0 + c$, with c the LEFM size equivalent of the process zone, as $d \to \infty$, $c \to c_f$, G_f the corresponding value of G, $c_f/d \to 0$ and thus $\alpha \to \alpha_0 = a_0/d$, $G_f = \lim G_c$, which is also equal to $\lim (K_{Ic}^2/E')$ for $d \to \infty$, calculated at peak load P_u and crack length

a_0 using the traditional LEFM equations.

The value of c at $P = P_u$ determines the value of α and thus the value of $g(\alpha)$ at failure so the ratio $G/g(\alpha)$ at maximum load is approximately equal to $G_f/g(\alpha_f)$ as can be seen from (2.20). Therefore, $G \approx G_f g(\alpha)/g(\alpha_f)$ and substituting into (2.20) with the Taylor expansion (continuous and smooth),

$$g(\alpha) \approx g(\alpha_0) + g'(\alpha_0)(\alpha - \alpha_0) \tag{2.22}$$

for $\alpha = \alpha_f = \alpha_0 + c_f/d$ and $g'(\alpha_0) = dg(\alpha_0)/d\alpha$ and further from (2.19), we obtain the following size effect law:

$$\sigma_N = c_n \left(\frac{E' G_f}{g'(\alpha_0) c_f + g(\alpha_0) d} \right)^{1/2} \tag{2.23}$$

or rewritten as,

$$\tau_N = \left(\frac{E' G_f}{c_f + \bar{d}} \right)^{1/2} \tag{2.24}$$

where,

$$\tau_N = \frac{P_u}{bd} \sqrt{g'(\alpha_0)} \quad \text{and} \quad \bar{d} = \frac{g(\alpha_0)}{g'(\alpha_0)} d \tag{2.25}$$

with τ_N being the shape independent nominal stress at failure and $\bar{d}$, sometimes expressed as D by the author, the shape independent size of the specimen, achieved due to the shape factors $g(\alpha_0)/g'(\alpha_0)$.

The above law has also been derived by using the method of energy release zones as well as by dimensional and similitude analysis [80], expressed as:

$$\sigma_N = \frac{B f_u}{\sqrt{1+\beta}} \quad \text{with} \quad \beta = \frac{d}{d_0} \tag{2.26}$$

where f_u an arbitrary measure of the material strength, B and d_0 two empirical constants and β, as described by the author, the brittleness number.

The above equation is derived for two and three-dimensional analysis and can also be used in unnotched specimens, although with the condition, that a macro-crack forms in a stable manner before the failure load. Equation (2.26) describes the relation between σ_N and the brittleness number β where, as shown in Figure 2.10, for large β such as $\beta = 10$ it approximates $\sigma_N = B f_u \beta^{-1/2}$, with an error of about 4.9 %, equivalent to the LEFM size effect as shown earlier. Smaller values such as $\beta = 0.1$, with the same error as

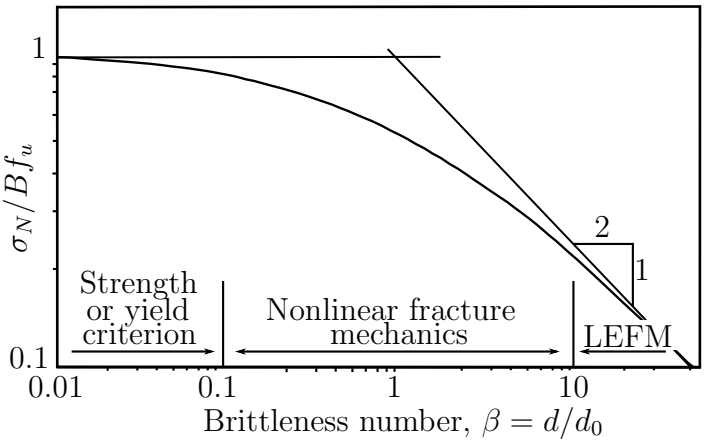

Figure 2.10: Size effect law asymptote, reproduced from Bažant [80].

above, yield no size effects with the failure load being proportional to the strength of the material ($\sigma_N = Bf_u = \text{constant}$). The figure referenced above and this basic transition size effect curve was conceived earlier to the works of Bažant, although without any formulation [81].

From (2.20), where at maximum load $P_u = bd\sigma_N/c_n$ and using (2.26) for σ_N, noting that $\lim \alpha = \alpha_0$ as $d \to \infty$, we get the formula [82],

$$G_f = \lim_{d\to\infty} \frac{P_u^2 g(\alpha)}{E' b^2 d} = \frac{B^2 f_u^2}{c_n^2 E'} \lim_{d\to\infty} \frac{d}{1 + d/d_0} \lim_{\alpha\to\alpha_0} g(\alpha) \tag{2.27}$$

which yields,

$$G_f = \frac{B^2 f_u^2}{c_n^2 E'} d_0\, g(\alpha_0) \tag{2.28}$$

Based on (2.28) and (2.20), knowing that $G \to G_f$ as $d \to \infty$, with $P = P_u$ and σ_N as above, their difference yields

$$d_0\, g(\alpha_0) = \frac{d}{1 + d/d_0} g(\alpha) \tag{2.29}$$

substituting $g(\alpha)$ from (2.29) into (2.22) with $c \to c_f$, where α close to α_0, $\alpha - \alpha_0 = c_f/d$ we get the following expression for the effective fracture process zone length

$$c_f = \frac{g(\alpha_0)}{g'(\alpha_0)} d_0. \tag{2.30}$$

The brittleness number β can therefore, from (2.25) and (2.30), be expressed

as

$$\beta = \frac{\bar{d}}{c_f}. \tag{2.31}$$

In conventional testing, K_{Ic}, normally found from LEFM, is used with no regard towards the length of the process zone and its variations as $\alpha = \alpha_0$ ($a = a_0$, $c = 0$) at the failure load. For this case, from (2.20) and (2.26), with $P^2 = P_u^2 = (bd\sigma_N/c_n)^2 = (bdBf_u/c_n)^2\, d_0/(d + d_0)$ and expressing Bf_u as G_f from (2.28) one gets

$$G_{\mathrm{c}} = G_f \frac{d}{d + d_0} = G_f \frac{\bar{d}}{\bar{d} + c_f}. \tag{2.32}$$

Since $K_{\mathrm{Ic}} = (EG_{\mathrm{c}})^{1/2}$ the apparent fracture toughness can be written as

$$K_{\mathrm{Ic}} = K_{\mathrm{I}f} \left(\frac{\bar{d}}{\bar{d} + c_f} \right)^{1/2}. \tag{2.33}$$

The above can be rearranged in the form of $Y = AX + C$ with

$$X = \frac{1}{\bar{d}} \qquad Y = \frac{1}{K_{\mathrm{Ic}}^2} \qquad A = \frac{c_f}{K_{\mathrm{I}f}^2} \qquad C = \frac{1}{K_{\mathrm{I}f}^2}. \tag{2.34}$$

Equation 2.24 can be algebraically rearranged in the same manner as above with

$$X = \bar{d} \qquad Y = \frac{1}{\tau_N^2} \qquad A = \frac{1}{K_{\mathrm{I}f}^2} \qquad C = \frac{c_f}{K_{\mathrm{I}f}^2}. \tag{2.35}$$

With the linear regression of either plot from (2.34) or (2.35), an estimation of the slope and intercept can be made i.e. the values of $K_{\mathrm{I}f}$ and c_f. Based on the equivalent fracture process zone c_f, the brittleness number range can be calculated and subsequently used in further comparing different materials rather than simply by specimen size.

Bažant also showed a clear effect of size (slenderness) to stability [37], based on his early study on ductility [83], which in this case is defined as the ratio of displacement at the loss of stability (vertical load-displacement tangent) during fracture to the elastic part of the displacement at maximum load. This effect will be examined further in the next chapter.

2.4.1 Sakai 1995

Sakai and Kurita [75] used Bažant's size effect law seen above to estimate the fracture toughness as well as the dimensions of the LEFM equivalent fracture process zone of the isotropic IG-11. Geometrically similar SEN(B) specimens of different sizes with width (W) in the range of 20 to 90 mm and $\alpha_0 = 0.5$ (although with a fixed depth of 10 mm) and fixed size SEN(B) and C(T) specimens with different initial notches ($\alpha_0 = 0.3 - 0.7$) were used to examine their apparent toughness K_{Ic}, or as nominated by Sakai and Kurita K_{Q} and extrapolate the value of $K_{\mathrm{I}f}$ (K_{c} and K_{s} by Sakai and Kurita). By modifying Bažant's expression and using the width of the specimen W as the characteristic size d to account for crack propagation in order to further determine the contributions of both the frontal process zone and crack bridging region to the fracture process zone, the authors came up with the following equivalent relationships:

$$\bar{\alpha_0} \equiv \bar{W} \quad \text{and} \quad \hat{\tau_c} \equiv \tau_c \tag{2.36}$$

with $\bar{\alpha_0}$ based on $K = Y\sigma\sqrt{\pi a_0}$ as seen in (2) to (7) of the original work, $\bar{W} = \bar{d}$ and $\tau_c = \tau_N$ from (2.24) and (2.25). Based on the above Sakai and Kurita managed to incorporate the initial crack length as a size variable thus involving non-geometrically similar specimen (different α_0) in this size effect study. The equivalent crack length extension $\Delta\bar{a}$ was also used ($\bar{a} \equiv \bar{\alpha_0} + \Delta\bar{a}$) to determine the length of the crack bridging region at the plateau toughness during the steady state, with the following algebraic arrangement, similar to the one seen in 2.35.

$$\frac{1}{\tau_s^2} = \frac{1}{K_s^2}\bar{a} + \frac{c}{K_s^2} \tag{2.37}$$

Where notably, $c_f \rightarrow c(= c_f + c_{\mathrm{b}})$ to include the size of the bridging zone c_{b} after it forms during the steady state s.

Results for the case of the geometrically similar SEN(B) specimens showed an increase in apparent toughness K_{Ic} (K_{Q}) with respect to specimen width W. The SEN(B) and C(T) specimens showed a decrease in apparent toughness with increase in α_0. With the use of the modified size effect law to incorporate all the experimental data, with the introduction of additional error [84], the linear relations between the intrinsic strength τ_N (τ_c) and $\bar{\alpha_0}$ or $\bar{W}$ gave a $K_{\mathrm{I}f} = 0.82\,\mathrm{MPa\,m^{1/2}}$, as seen converging in Figure 2.11, and a $c_f = 620 \pm 50\,\mu\mathrm{m}$. Using (2.37) with the same method as above, Sakai found the steady-state

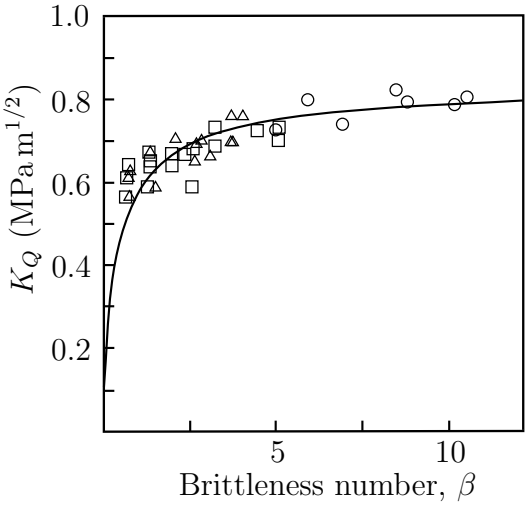

Figure 2.11: Size effect plot of apparent toughness K_Q of different specimen types versus the brittleness number β, where ○ geometrically non-similar C(T) specimens, □ similar SEN(B) specimens and △ non-similar SEN(B) specimens; reproduced from Sakai and Kurita [75].

$K_s = 1.17\,\mathrm{MPa\,m^{1/2}}$ and the bridging zone $c_b = -560 \pm 50\,\mu\mathrm{m}$, based on the assumption that the formation of the bridging zone has minimal effect to the frontal zone size, using the minus sign to emphasise its presence behind the crack tip.

Sakai and Kurita on a follow-up study [85], used the data acquired from the study above in addition to experimental data from carbon felt composite (CFC) compact tension specimens. Results on the measurement of the FPZ showed agreement with what was previously published [47].

2.4.2 Statistical size effect

> A long rope and a short rope always support the same weight unless that in a long rope there may happen to be some faulty place in which it will break sooner than in a shorter.

Mariotte's observation documented in his work *Traité du mouvement des eaux et des autres corps fluides* (1686), as seen translated from the original by Bažant [84], served as the basic idea behind the statistical size effect theory and subsequently the work of Weibull [86, 87]. Through the Weibull distribution one can relate the implication that an increase in specimen size increases the

probability of a critical flaw and subsequently failure.

$$\frac{\sigma_1}{\sigma_2} = \left(\frac{V_2}{V_1}\right)^{1/m}. \tag{2.38}$$

For different specimen volumes V_1, V_2 and $m > 1$ (based on the above assumption), the Weibull modulus or shape parameter, which is a measure of the scatter (higher m, less scatter), produced by a Weibull distribution fit on the original data.

Brocklehurst [40] and Bažant *et al.* [88] have underlined the limitation of Weibull's theory to consider the stress redistribution caused by the formation of a large crack at loads prior to the maximum load, thus also introducing a geometry parameter. Also, in its classical application, the theory disregards failure mechanisms and geometry as every specimen is considered equivalent to a uniaxial bar which does not account for stress gradients and the probability of "small defects" on the highly stressed volumes [89].

Even though studies considering modifications to the classic theory either by different parameters [90, 91] or considering the effects of different stress gradients [92, 93] show promise, for the purpose of this study, size effects will be studied using Bažant's law. This involves comparing the apparent fracture toughness K_{Ic} (K_{Q}) of the different sized specimens, of a similar type, to extrapolate and determine the $K_{\mathrm{I}f}$ and c_f which respectively are material constants for the fracture toughness and process zone in an infinite sized specimen.

Chapter 3

Instability and boundary conditions

Often, as expressed by Mai and Lawn [29], the simple failure conditions as the $G = G_c$ are not enough to characterise fracture. Instability, especially for the case of graphite and other quasi-brittle materials, with such a narrow window for stable fracture, is a battle between energy release rate or crack driving force G and fracture resistance R. The energy release rate is an important parameter to examine and being more theoretical than its resistance counterpart, it can be studied initially without the need for an experiment, with its understanding being crucial to the experimental work.

The aim of this chapter is to underline the parameters that contribute to the instability of the specimen and by extension the structure by altering the energy release rate or the energy available for the extension of the crack. This is often overlooked in favour of the more intricate fracture resistance but it is part of the same stability equation as seen in Subsection 2.2.1 and thus equally important. The above aim will be achieved by the introduction of a model and dimensionless load and displacement method. These two will be utilised comparing the stability behaviour of different specimens as well different loading conditions and stiffness configurations.

Firstly, a review of the specimen types and how to evaluate their stability profile based on a dimensionless load and displacement method will be presented. Following, a discussion will be held on the boundary conditions and the equivalent experimental structures that can be used to approximate the real-world scenarios. Through the model introduced, examples on how boundary

conditions can affect the stability behaviour of a specimen will be presented.

3.1 Instability

Sakai and Inagaki [36] proposed the use of dimensionless load-displacement to examine how different specimen geometries and thus compliance and stress intensity functions perform with crack propagation. By reshaping the load and displacement functions for a specimen as seen below, only the compliance and stress intensity functions are used. As the energy accumulated by the specimen is a function of both of the above, instability of a specimen can be assessed without the need for specific dimensions. This way to evaluate specimen instability in the absence of specific dimensions will be examined, although dimension ratios (such as crack to width, span to width or length to width) will be assumed. This method will be used as can be more flexible and efficient in offering an insight into specimen stability with varying geometries. By recasting specific dimensions on the formulas, real resistance measuring problems can be assessed.

3.1.1 Dimensionless load and displacement

To quantify the dimensionless instability of a specimen, firstly the dimensionless load and displacement must be introduced. The fracture load of a specimen can be written as,

$$P_c = K_c \frac{BW^{1/2}}{Y(\alpha)} \tag{3.1}$$

and the displacement,

$$\Delta_c = z_{\text{ll}}(\alpha) \frac{P_c}{BE} \tag{3.2}$$

with $Y(\alpha)$ the dimensionless stress intensity function or shape factor, $z_{\text{ll}}(\alpha)$ the dimensionless load line compliance function [31] and α the relative crack length ($= a/W$). The dimensionless load $\tilde{P}$ and displacement $\tilde{\Delta}$ can be written as follows, with the use of critical load P_c and displacement Δ_c,

$$\tilde{P} = \frac{P_c}{K_c BW^{1/2}} \tag{3.3}$$

$$\tilde{\Delta} = \frac{\Delta_c E}{K_c W^{1/2}}. \tag{3.4}$$

Based on the compliance and stress intensity functions, seen in (3.2) and (3.1), with the assumption no other energy dissipation mechanisms and constant values of K and E, (3.3) and (3.4) can be written as:

$$\tilde{P} = \frac{1}{Y(\alpha)} \tag{3.5}$$

$$\tilde{\Delta} = \frac{z_{ll}(\alpha)}{Y(\alpha)}. \tag{3.6}$$

The load-displacement relationship, if plotted with respect to crack length, will essentially describe the fracture behaviour of the specific specimen type irrespective of material properties (LEFM) and dimensions, with the only requirement it follows the specimen standards used for the formulation of its compliance and stress intensity functions. The above dimensionless relationship can be seen in Figure 3.1 where it is plotted for the compact tension and single edge notch beam geometries with a crack propagating from $\alpha_0 = 0.2$ to $\alpha = 0.9$, following the ASTM-E399 [94] and ASTM-E1820 [61] standard specimen functions.

For the case of the SEN(B) the span to width ratio must be incorporated in the functions as to be able to graphically compare them to the C(T) specimen based on the dimensionless $BW^{1/2}$ instead of $S/BW^{3/2}$ that is present outside the function expressed by the standard. For the following figures a $S/W = 4$ ratio according to standard is used.

Sakai and Inagaki [36], for the case of the SEN(B), propose the integration of the $Y(\alpha)$ function to determine the compliance at a specific relative crack length point of equilibrium. This may lead to errors mainly due to two reasons. Firstly, an error can be introduced as the method requires the compliance of the specimen without a notch which can be difficult for the case of complex specimen geometries. Secondly, the integration of the SEN(B) $Y(\alpha)$ function over the relative cracked length $(0 \rightarrow \alpha)$ will lead to errors as the function itself is valid for ratios between 0.2 and 0.9.

3.1.2 Dimensionless total energy

To evaluate the stability of a dimensionless specimen geometry, a dimensionless function for its total energy with respect to relative crack length and thus its energy release rate must be introduced. The total energy of the specimen, in

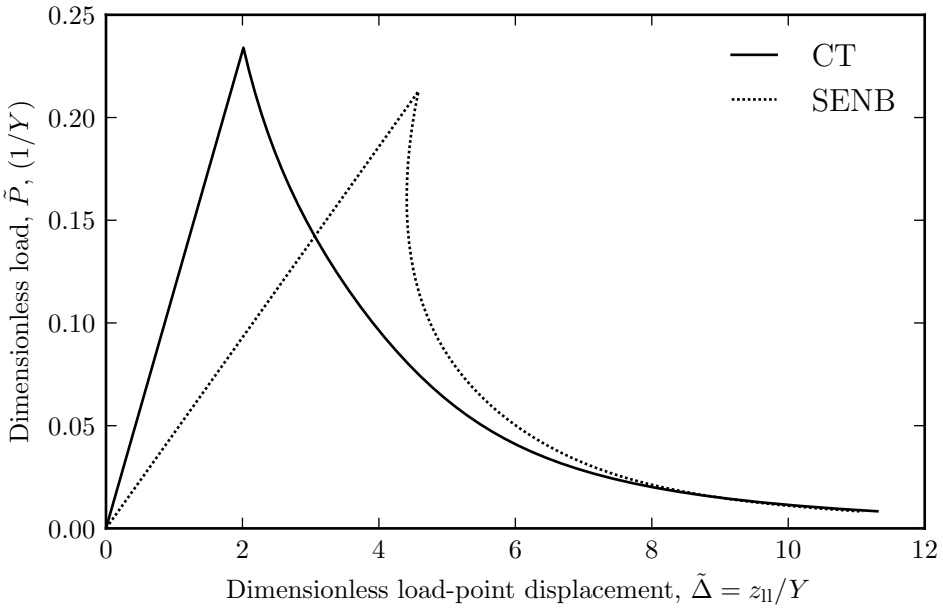

Figure 3.1: Dimensionless equilibrium load-displacement showing the relationship of dimensionless compliance z_{ll} and shape factor Y, for increasing crack lengths ($\alpha_0 = 0.2 \rightarrow 0.9$) in compact tension (C(T)) and single edge notch beam (SEN(B)) standard specimen geometries. Straight lines plotted from point $0, 0$ to peak dimensionless loads for illustration purposes.

equilibrium, during static crack extension is the sum of its potential (elastic energy on the specimen) and the fracture surface energy [36]:

$$G_{\text{eq}}(\alpha) = U_{s_{\text{eq}}}(\alpha) + 2\gamma_s (A - A_0). \tag{3.7}$$

The above essentially describes the total work done to elastically strain the specimen and by extension, with crack propagation, create or extend the crack surface.

The function $G_{\text{eq}}(\alpha)$ with (α) can properly describe the change in energy of the specimen at the equilibrium of fracture on crack initiation and propagation. If the change in total energy $G_{\text{eq}}(\alpha)$ on the equilibrium is positive ($G_{\text{eq}}(\alpha_1) < G_{\text{eq}}(\alpha_2)$, with $\alpha_1 < \alpha_2$), the specimen in equilibrium requires extra work to propagate the crack, thus exhibiting stable characteristics. For the case where $G_{\text{eq}}(\alpha_1) > G_{\text{eq}}(\alpha_2)$, the excess energy would provide means that can lead to unstable fracture.

The above can be used to theoretically examine the stability profiles of different specimen geometries in a dimensionless fashion. Using $\tilde{G}_{\text{eq}}(\alpha) = G_{\text{eq}}(\alpha)/BW(2\gamma_s)$, as expressed by Sakai [36], we can specify the dimensionless form of the energy. With the substitution of (3.3) and (3.4) as well as Irwin's formulation of K, ($K_c^2 = 2\gamma_s E$), we arrive in the following form:

$$\tilde{G}_{\text{eq}}(\alpha) = \frac{1}{2}\tilde{P}\tilde{\Delta} + \frac{(A - A_0)}{BW}. \tag{3.8}$$

Where $(A - A_0)/BW$ can be expressed as $\alpha - \alpha_0$, the difference in relative crack length, thus providing a dimensionless (3.8) as seen below,

$$\tilde{G}_{\text{eq}}(\alpha) = \frac{1}{2}\tilde{P}\tilde{\Delta} + \alpha - \alpha_0. \tag{3.9}$$

Using the empirical compliance and stress intensity functions, as seen in equations 3.5 and 3.6, one can plot the dimensionless total energy $\tilde{G}_{\text{eq}}(\alpha)$ to the relative crack length a/W and graphically evaluate $dG/d\alpha$. The values of dimensionless $\tilde{G}$ in equilibrium to relative crack length for three specimen types are plotted in graphs 3.2 and 3.3. The SEN(B) specimen shows initial unstable equilibriums ($d\tilde{G}/d\alpha < 0$) up to $\alpha \approx 0.4$ where it reaches a stable state with increasing crack lengths. The C(T) is exhibiting stable equilibrium states ($d\tilde{G}/d\alpha > 0$) throughout the same relative crack length area making it ideal

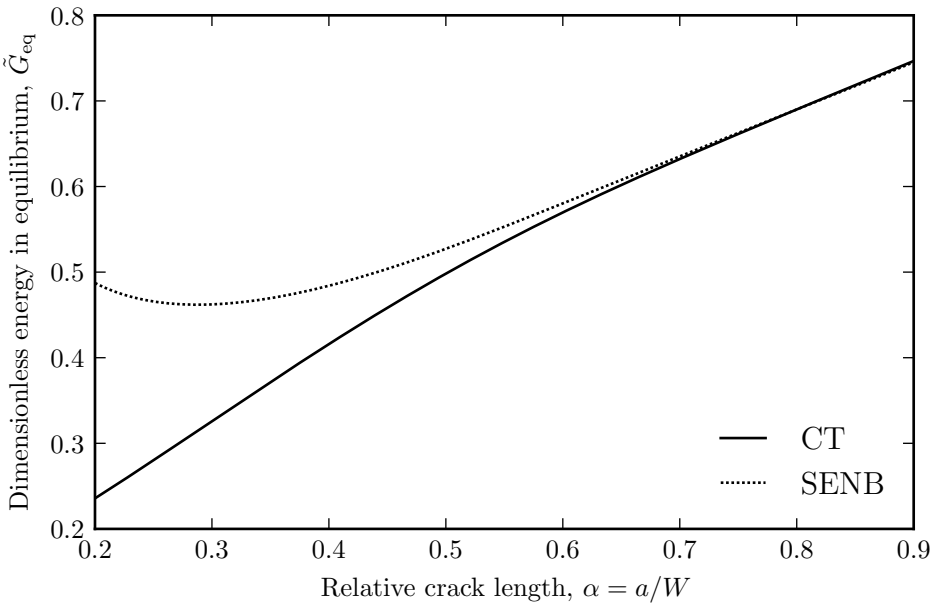

Figure 3.2: Dimensionless equilibrium total energy with relative crack length showing the fracture behaviour of compact tension (C(T)) and single edge notch beam (SEN(B)) standard specimen geometries for increasing crack lengths ($\alpha_0 = 0.2 \rightarrow 0.9$).

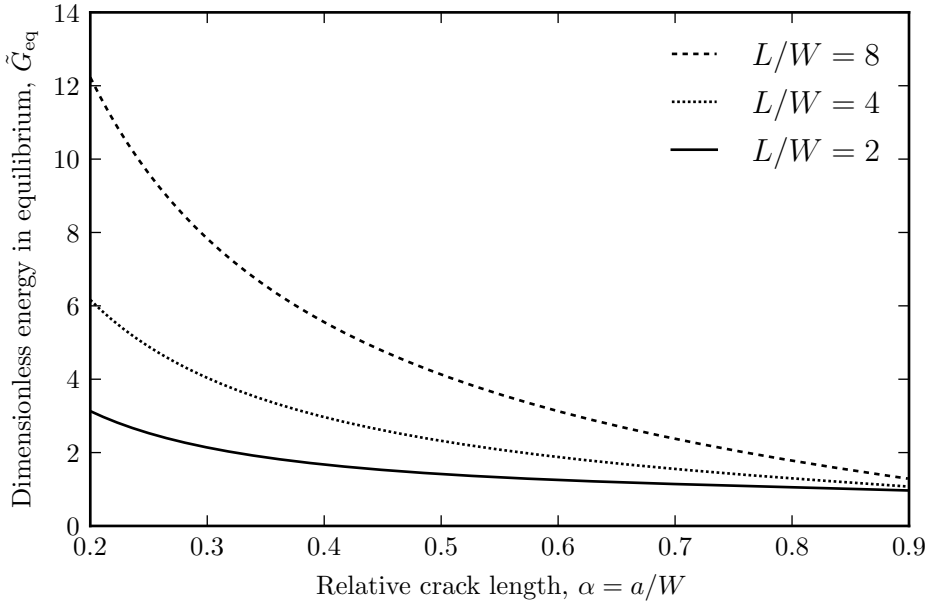

Figure 3.3: Dimensionless equilibrium total energy with relative crack length showing the fracture behaviour of middle tension (M(T)) standard specimen geometry, for increasing crack lengths ($\alpha_0 = 0.2 \rightarrow 0.9$), with various length to width ratios (L/W).

for experimental testing on resistance.

The middle tension specimen behaves in an unstable manner as $d\tilde{G}/d\alpha < 0$ for the entirety of the cracking (Figure 3.3), on every case. Also, with the increase in L/W ratio, a greater decrease in $d\tilde{G}/d\alpha$ is exhibited showcasing the importance of additional energy accumulation. This difference can be attributed to the relatively larger volume and thus elastic energy that can contribute to the cracking process after crack initiation as also acknowledged by Chell [95, 96]. A way to extrinsically describe this effect will be discussed below.

3.2 Elastic follow-up

The energy contribution of the crack surrounding material, as seen in Figure 3.3, on the specimen can drastically affect its fracturing behaviour. A simplified concept of elastic follow-up (EFU) will be introduced as it can offer a way to describe this contribution.

Elastic follow-up is a phenomenon initially examined from the difference in creep behaviour of bolts between a rigid and a more compliant flange and described as follow-up elasticity [97, 98]. Roche [99, 100], described this as a spring effect and used two identical wires in fixed displacement and fixed load respectively to define it. The difference in elastic energy follow-up, and equivalently stability, can be thought of as a divergence from displacement control to a value between the extremes of load and displacement control [98].

Elastic follow-up will be considered as the elastic energy contribution after crack initiation and extension due to the change in relative stiffness. This energetic follow-up, may affect the stability behaviour of the specimen or structure [101]. The section below will examine two of the structure types (Figure 3.4) used to approximate this intermediate boundary condition, and thus elastic follow-up, in case of pure loading and displacement control and quantify how it approaches these two extremes, serving as a precursor to the experimental part of the work.

3.2.1 Series

As discussed in the literature review, Hutchison [34], used a spring in series with the specimen to describe machine compliance and quantify its effect (Fig-

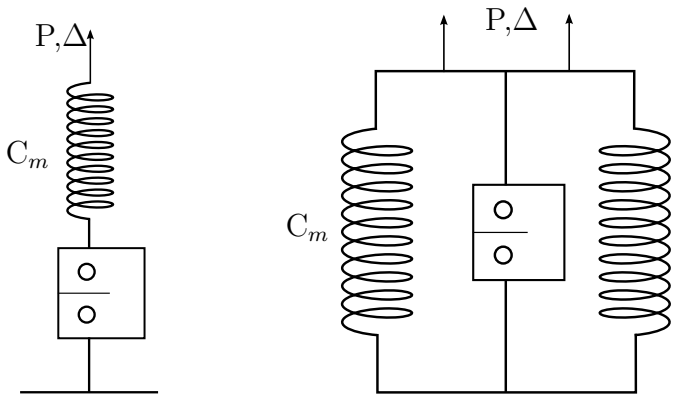

(a) Series (b) Parallel

Figure 3.4: Simple element models. (a) Series model, (b) Parallel or three bar model.

ure 3.4a). It can be said that for the case of load control, this series structure will behave exactly as the specimen by itself would. This can be understood from the fact that specimen and spring when in series share the same load as equivalently two springs in series. If the load is held constant after crack initiation, the spring compliance would have no effect in the stability of the specimen as the load is the same between them. The change in specimen compliance will have no additional effect to its stability behaviour as there is no added contribution from the spring to the specimen.

For displacement control, spring compliance is a key factor to the behaviour of the specimen. During crack initiation and extension, the displacement is held constant between specimen and spring, meaning that the decrease in load in the specimen with the increase in compliance must be accommodated in the same manner by the spring. The excess energy stored in the compliant spring will be released due to the load drop on the specimen, resulting in an intermediate behaviour between load and displacement control. The degree of proximity to these two extremes and thus the energy released can be quantified by (2.6), based on the initial assumption of shared load between spring and specimen, not the case for the three-bar structure. In the case of a non-compliant spring, the structure behaves in pure displacement control.

3.2.2 Parallel

The parallel structure (Figure 3.4b) is mostly used in relation to residual stresses and their relaxation with respect to an event (creep, yield, crack initiation) [102]. It is used as a local idealised structure, with three bars in parallel and the middle one being the specimen, where the processes affecting the cracked area share the displacement with the rest of the structure. A misfit is normally used for the middle bar to simulate the residual stresses on the specimen and quantify their behaviour after the event [98].

In load control, theoretically, the structure will behave in a more stable manner compared to the series model. This is achieved by the load being shared between the bars, as springs in parallel share the load while having the same displacement. By sharing the load, even for the case of pure load control, theoretically infinitely stiff outer springs will 'shield' the specimen in the middle and would provide displacement dictated by their own high stiffness. During crack initiation and extension, the increasing compliance of the specimen will lead to a drop in its load which will be accommodated by the outer bars to an equilibrium.

In displacement control, the three-bar structure and the specimen in the middle will always behave as in pure displacement control. This is irrespective of outer spring stiffness due to the specimen sharing the same displacement with the machine.

The ratio of stiffness or compliance between the outer and the inner, or in reality the cracked area to the rest of the structure quantify the EFU. Generally, the higher the stiffness ratio, the more stable the behaviour of the specimen. Further formulation for the EFU, specifically with the introduction of a misfit, although not in the scope of this work can be found in the work of Aird *et al.* [102].

3.2.3 Dimensionless total energy, load and displacement

As can be seen in (3.7), the total energy is a sum of the elastic and fracture surface energy. For the equation above, only the specimen elastic energy is considered. In order to account for the contribution of the spring (Figure 3.4a) its elastic energy must be considered as well. The total stored elastic energy $U_{tot_{\mathrm{eq}}}(\alpha)$ at the equilibrium for the specimen in series with the spring can be

written as,

$$U_{tot\text{eq}}(\alpha) = U_{s\text{eq}}(\alpha) + U_{m\text{eq}}. \tag{3.10}$$

Knowing that, for the series configuration, the load between spring and specimen is shared and that subsequently the total compliance of the structure is the sum of the individual compliances ($C_{tot}(\alpha) = C_s(\alpha) + C_m$) the total elastic energy can be written as,

$$U_{tot\text{eq}}(\alpha) = \frac{1}{2} C_{tot}(\alpha) P_c^2. \tag{3.11}$$

Based on (3.11) and (3.9) the total dimensionless energy in equilibrium for a specimen in series is

$$\tilde{G}_{\text{eq}}(\alpha) = \frac{1}{2} C_{tot}(\alpha) \tilde{P}^2 + \alpha - \alpha_0. \tag{3.12}$$

With a ratio of machine or spring to specimen dimensionless compliance used in (3.12) and the use of (3.5) and (3.6) the total dimensionless energy in equilibrium is

$$\tilde{G}_{\text{eq}}(\alpha) = \frac{1}{2} \left(z_{\text{ll}}(\alpha) + \frac{C_m}{C_{\alpha_0}} z_{\text{ll}}(\alpha_0) \right) \left(\frac{1}{Y(\alpha)} \right)^2 + \alpha - \alpha_0. \tag{3.13}$$

The dimensionless compliance of the specimen at the initial crack length $z_{\text{ll}}(\alpha_0)$, will be written as C_{α_0} and will serve as a reference for the ratio used in the equation above which subsequently, if specific dimension were to be recast, would determine the spring or machine compliance C_m.

As the load is shared between machine and specimen it remains unaffected by the different ratios. The total dimensionless displacement in equilibrium, with the addition of machine to specimen ratio can be written as,

$$\tilde{\Delta} = (z_{\text{ll}}(\alpha) + C_m) \frac{1}{Y(\alpha)}. \tag{3.14}$$

The equilibrium load-displacement of the specimen itself would be the same regardless of ratio, following its compliance relationship. As the equilibrium load-displacement is solely snapshots of the functions for each crack length with the addition of spring compliance, the effect of snap-back can be seen (Figure 3.6). This behaviour, where there is a vertical tangent ($d\tilde{\Delta}/d\tilde{P} = 0$), signifies the stability limit in displacement control. This limit can also be seen,

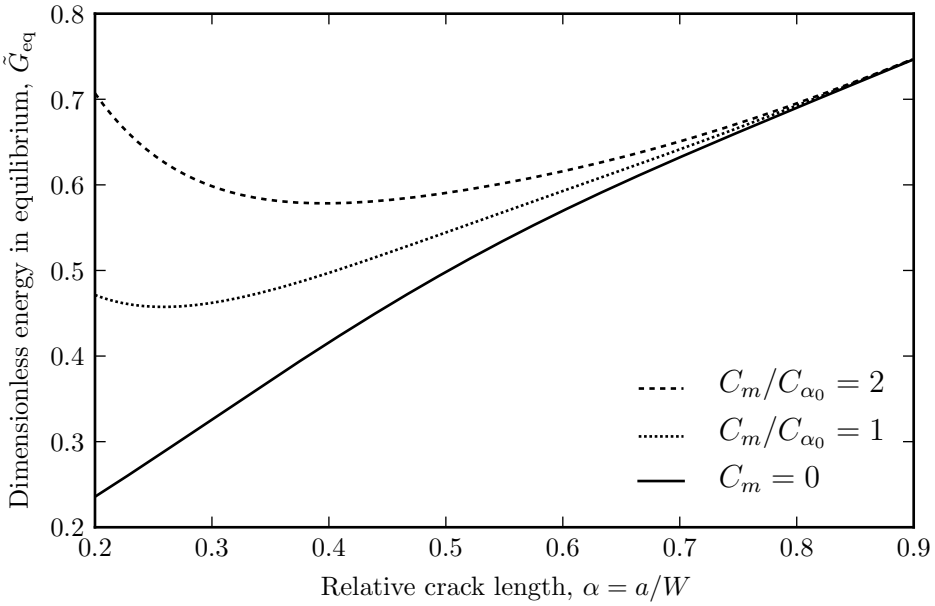

Figure 3.5: Dimensionless equilibrium total energy with relative crack length showing the fracture behaviour of compact tension (C(T)) standard specimen geometry, for increasing crack lengths ($\alpha_0 = 0.2$ and $\rightarrow 0.9$), with various spring to initial specimen compliance ratios (C_m/C_{α_0}).

as shown earlier, where $d\tilde{G}/d\alpha < 0$ in Figure 3.5. Bažant [37] graphically expressed this snap-back on a structure by superposition of different elements (specimen, compliant and stiff spring) and quantified this effect as structure ductility. Although, as Bažant argues, this snap-back behaviour may be crucial to the energy absorption of a structure under impact, blast or seismic loads, it is not in the scope of this research and will not be examined further.

As Figure 3.6 is not indicative of specimen behaviour under static loads, a model will be required to examine the load-displacement behaviour under displacement control in series. Load control is not to be regarded as stability loss, for the case of the examined specimens, occurs at the peak load.

3.3 Series model

As expressed in the previous section, a model, instead of the equilibrium states is essential to express a load-displacement relationship under displacement control. As the specimen and spring are loaded, there may be "jumps" in-between consecutive (as defined by $d\alpha$) equilibrium states. These "jumps"

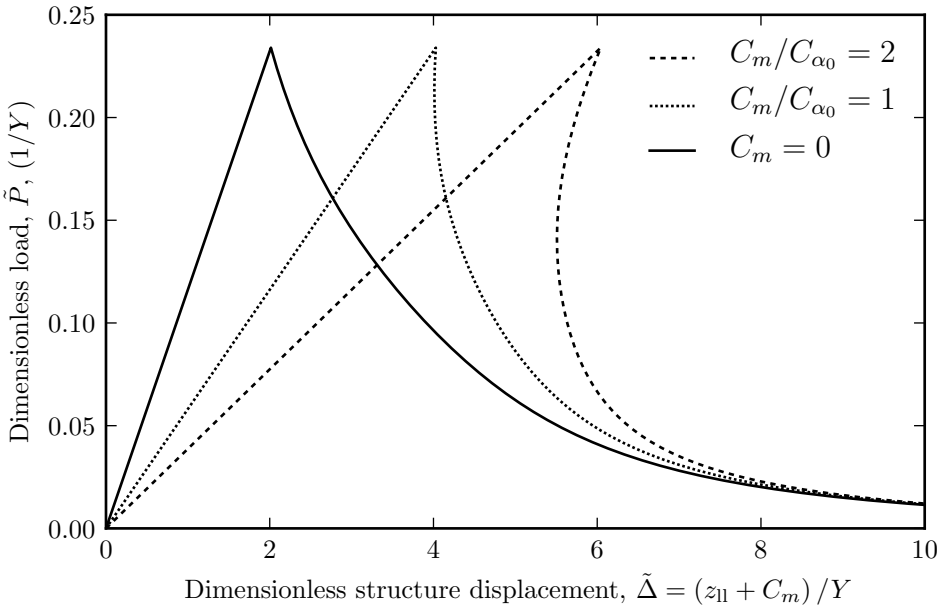

Figure 3.6: Dimensionless equilibrium load-displacement for series structure with compact tension (C(T)) standard specimen geometry, for increasing crack lengths ($\alpha_0 = 0.2 \rightarrow 0.9$), with various spring to initial specimen compliance ratios (C_m/C_{α_0}). Straight lines plotted from point $0, 0$ to peak dimensionless loads for illustration purposes.

cannot be captured by the relationship seen in Figure 3.6, although hinted by the dimensionless equilibrium energy (Figures 3.2, 3.3, 3.5).

3.3.1 Variables and structure

The variables of the model as well as its structure are presented below.

Specimen

A standard compact tension specimen is selected due to its theoretically stable behaviour throughout its length, compared to the SEN(B), as seen in Figure 3.2. The compliance $z_{\mathrm{ll}}(\alpha)$ and stress intensity function $Y(\alpha)$ remain the same as in the previous section. Specimen dimensions follow the current compact tension standards [94] and are presented in the table below. As can be seen, an α_0 (a_0/W) of 0.2 was chosen in order to be directly compared with the equilibrium states of the section 3.2.

Table 3.1: Model specimen geometry variables

C(T) Specimen		
Specimen Thickness	B	25 mm
Specimen Width	W	50 mm
Initial Crack Length	a_0	10 mm

Material

The material properties used are equivalent to those of Gilsocarbon IM1-24, based on approximations from [57,103]. These values can be seen in table 3.2.

Table 3.2: Model specimen material variables

IM1-24 type graphite		
Poisson's Ratio	v	0.22
Young's Modulus	E	10 GPa
Critical SIF	K_{Ic}	1.2 MPa $\mathrm{m}^{1/2}$

Structure

After the initial specimen dimensions, material properties and compliance calculations, the structure is loaded at a rate of 0.0001 mm/iteration. At the end of each iterative displacement the load on the specimen is calculated based on the displacement of the structure and the ratio in compliance for spring and specimen. The specimen compliance is calculated based on the crack length through the $z_{\mathrm{ll}}(\alpha)$ function. By knowing the total compliance, $C_{tot}(\alpha) = C_s(\alpha) + C_m$, and the structure displacement the load on the specimen follows Hooke's law. With the specimen load value, a calculation check is done on the stress intensity factor based on the $Y(\alpha)$ function. If the value exceeds or is equal to the critical intensity factor the crack is extended by an increment of $W/10^4$ and every value is calculated again in the same fashion. This will either result in further crack extension or in the case of $K < K_{\mathrm{Ic}}$ to another incremental increase of the structure's displacement. The model stops when a normalised crack length of $\alpha = 0.9$ is reached. The values of load, specimen and structure displacement on corresponding crack lengths are stored throughout.

The model's algorithm is depicted in the flow chart presented in Figure 3.7.

3.3.2 Assumptions and conventions

Below are presented the several assumptions made for the displacement control series model.

- Crack propagation is defined as stable where theoretically there is a single unitary crack extension (numerically defined as da or $d\alpha$) following a unitary displacement (defined as $d\Delta$). Cracking is considered unstable when following a unitary displacement the crack extends further than the unitary in order to reach an equilibrium state.

- The model is linear elastic, all of the energy absorbed by the specimen is elastic and directly consumed for propagating the crack.

- The loading is applied in very small increments, comparable to an actual loading of 0.01 mm min^{-1}. The kinetic energy of the specimen and spring are negligible.

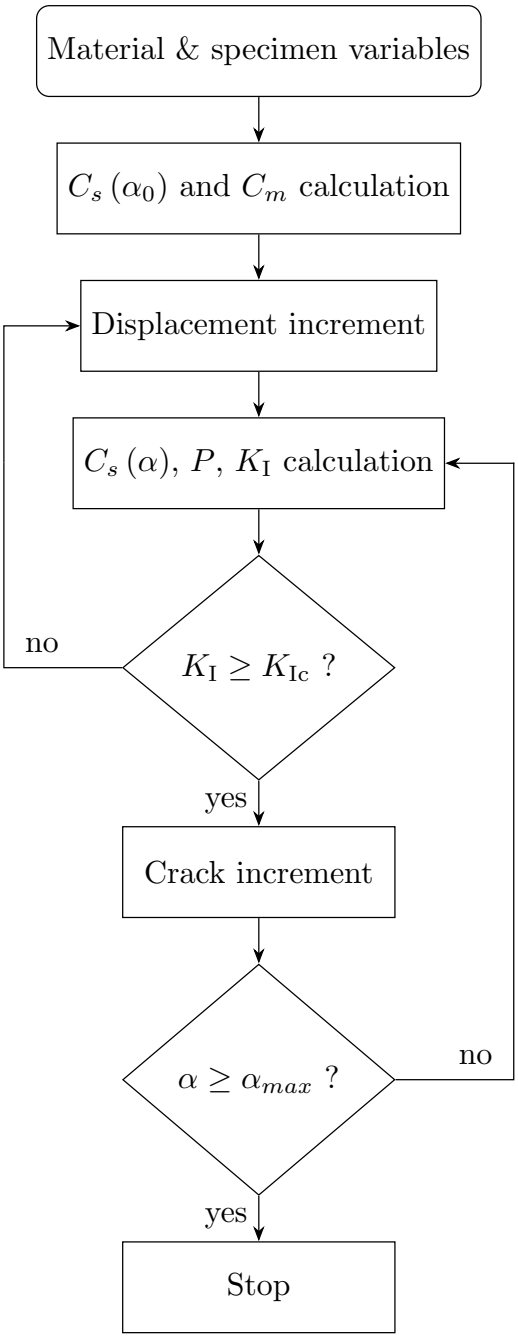

Figure 3.7: Simple flow chart describing the series, displacement controlled model's algorithm/structure.

- Crack propagation takes place in a loop when the stress intensity factor reaches or exceeds a constant critical value, with the displacement being held constant.
- Critical stress intensity factor K_{Ic} and Young's modulus E are held constant throughout the cracking process. This enables direct comparisons with the dimensionless load and displacement method.

The above assumptions underline the balance between da and $d\Delta$ and their importance to the model. High rates of displacement would introduce instabilities to the model by providing excess energy and thus facilitating larger equilibrium jumps. Larger unitary crack extensions may lead to conservative results as smaller instabilities could be masked. Essentially, the most valid instability assessment without regard to load and displacement is provided by the equilibrium total energy as seen in Figures 3.2, 3.3 and 3.5.

3.3.3 Results and comparison

A direct comparison between the model and the applied equilibrium technique will be presented below. The dimensionless load $\tilde{P}$ and displacement $\tilde{\Delta}$ cannot be plotted against the values of the model without being applied on specific material and specimen variables. The applied load based on the dimensionless can be calculated as $P = \tilde{P}\,(K_{\mathrm{Ic}}BW^{0.5})$ as can be seen from (3.3). From (3.4), the dimensionless displacement can be applied as $\Delta = \tilde{\Delta}\,(K_{\mathrm{Ic}}W^{0.5}/E)$. The above variables used the same values as presented in the tables of subsection 3.3.1.

The comparison of load and structure displacement for the simple case without a spring, or the equivalent of zero compliance on the structure par the specimen, can be seen in Figure 3.8. The figure, as stated above is of a C(T) specimen with initial normalised crack length of $\alpha_0 = 0.2$, the case for all subsequent results. As expected, the continuous and dashed line, i.e model and equilibrium states coincide. Also, after the peak load, the reloading process after each crack extension and load drop can be seen as a jagged line. The specific figure was calculated and plotted with a rate of 0.002 mm/iteration. By increasing the loading increment, it can be easily shown that each of these loading lines, if extended, pass through the origin, true to the model's linear elastic nature.

A more compliant structure with a ratio $C_m/C_{\alpha_0} = 2$ can be seen in Figure 3.9. As was expected with the introduction of a compliant spring, equilibrium states and model differ from the peak load onwards, or the initial unstable cracking until a point where stable cracking occurs. This difference occurs during the presence of instability as can be seen in Figure 3.5 where for the same compliance ratio, the specimen shows unstable behaviour as explained earlier. The model coincides with the equilibrium states at about 0.016 mm, 400 N point of structure displacement and load, or $\alpha = 0.65$ onwards. The above can be easily verified by a structure displacement plot with respect to crack length. The model of the structure behaves in a truly displacement controlled manner, compared to the equilibrium states which show comparable behaviour to Bažant's superposition [37].

Figure 3.10 shows the response of the structure according to the model. The area under the graph for the first two cases (no spring and ratio of 1) is about the same, as expected with the minimum amount of instability shown at $C_m/C_{\alpha_0} = 1$. The area for the case of $C_m/C_{\alpha_0} = 2$ is about 10 % greater. For the case of a ratio of 4 (not shown in the figure), the area under the graph, or the available elastic energy as it is mostly unstable after the peak load is approximately 50 % greater compared to the non-compliant structure.

Figure 3.11 shows a direct comparison of the specimen behaviour based on the different compliance ratios, with the fundamental case of no spring. In the two cases (ratio of 2 and 4), unstable cracking occurs from the peak load until about $\alpha = 0.65$ and $\alpha = 0.85$ respectively.

A direct comparison is drawn in Figure 3.12. A similar model is used to calculate the load and displacement under load control (1 N/iteration) where the springs are in parallel to the specimen i.e. sharing the same displacement. By using the same ratio of spring to specimen compliance, parallel and series load-displacement coincide and are unstable until about $\alpha = 0.65$ as previously seen.

3.4 Discussion

As can be seen from the model above and the equilibrium states of a specimen, results differ when cracking is unstable. Although difficult to capture this difference in the C(T) specimen with a non-compliant spring, as the geometry

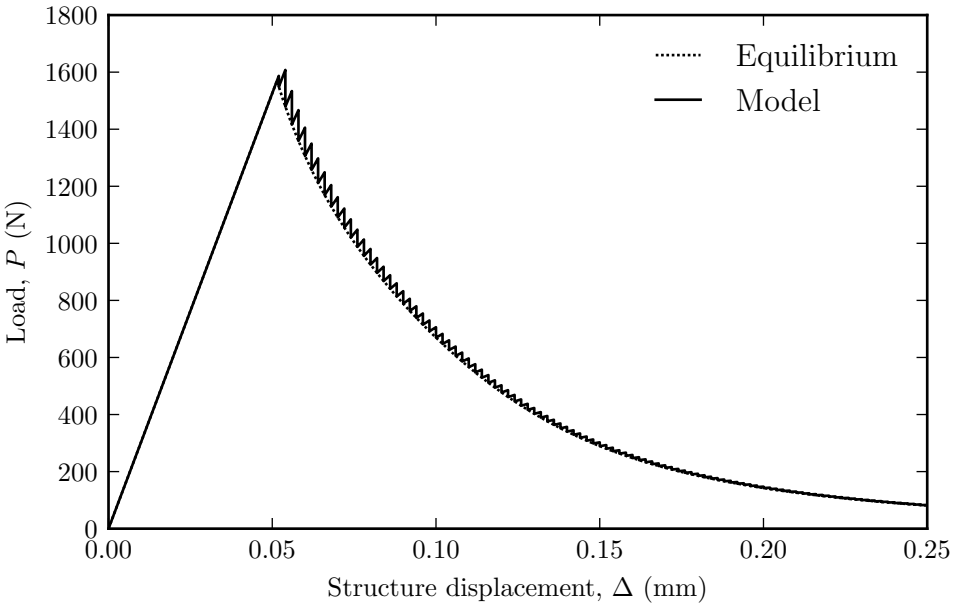

Figure 3.8: Load-Displacement for series structure with compact tension (C(T)) standard specimen geometry, for crack lengths ($\alpha_0 = 0.2 \rightarrow 0.9$), with non-compliant spring. Direct comparison between equilibrium states (Figure 3.6) and displacement control model. Straight lines plotted from point $0, 0$ to peak equilibrium load for illustration purposes.

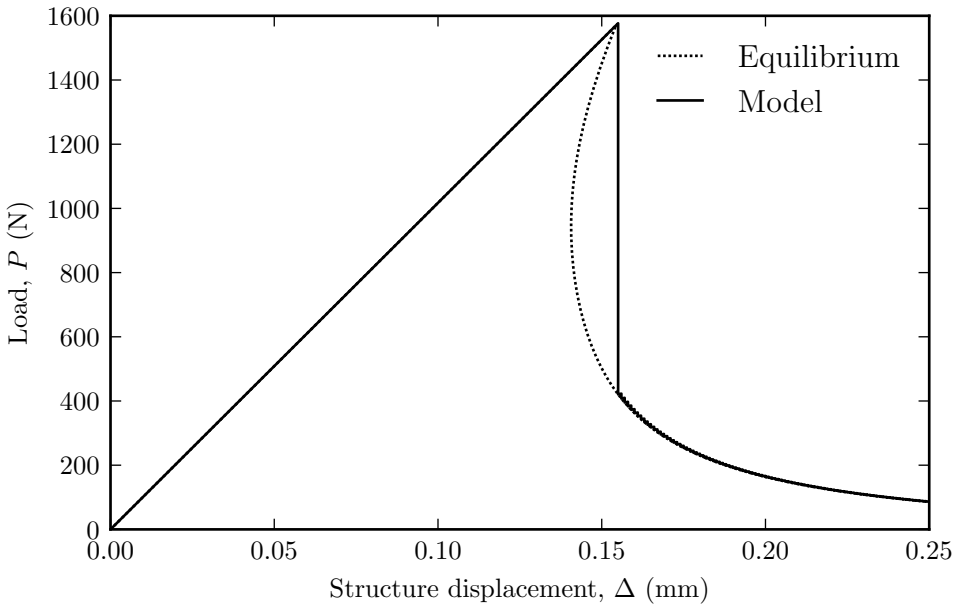

Figure 3.9: Load-Displacement for series structure with compact tension (C(T)) standard specimen geometry, for crack lengths ($\alpha_0 = 0.2 \rightarrow 0.9$), with spring to initial specimen compliance ratio $C_m/C_{\alpha_0} = 2$. Direct comparison between equilibrium states (Figure 3.6) and displacement control model. Straight lines plotted from point $0, 0$ to peak equilibrium load for illustration purposes.

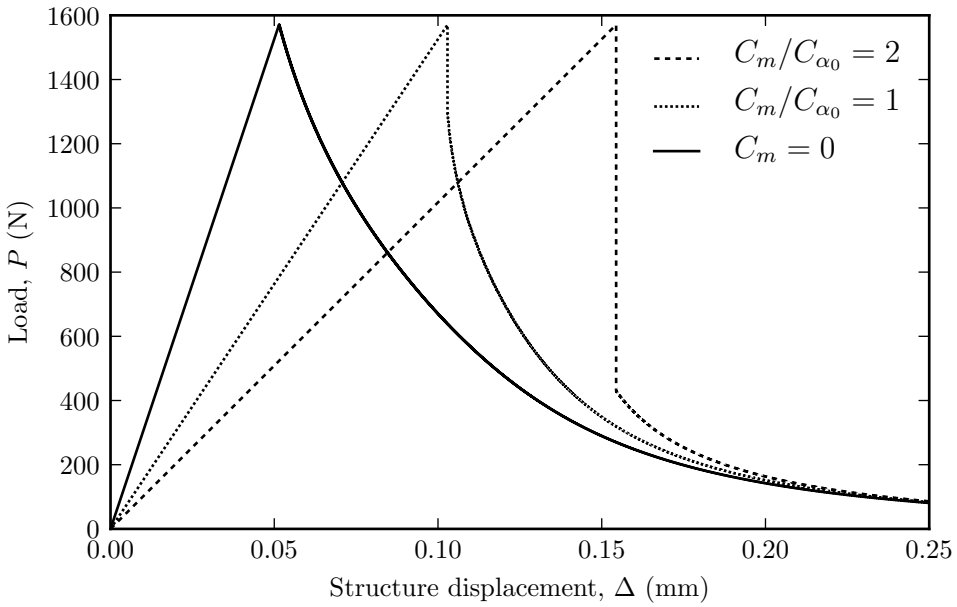

Figure 3.10: Load-Displacement for series structure model under displacement control with compact tension (C(T)) standard specimen geometry, for crack lengths $\alpha_0 = 0.2 \rightarrow 0.9$, with various spring to initial specimen compliance ratios (C_m/C_{α_0}).

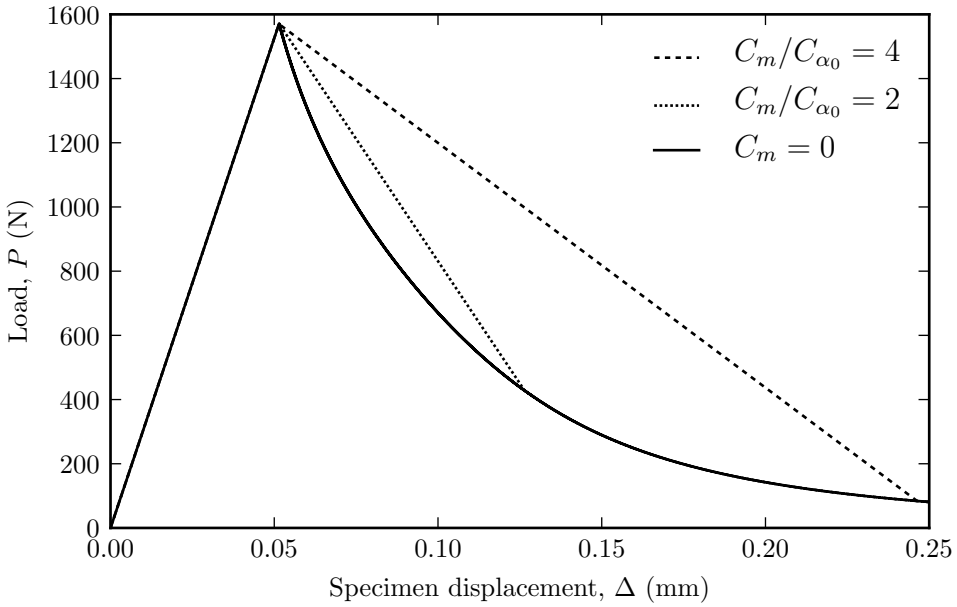

Figure 3.11: Load-Displacement model results under displacement control for series structure with compact tension (C(T)) standard specimen geometry, for crack lengths $\alpha_0 = 0.2 \rightarrow 0.9$, with various spring to initial specimen compliance ratios (C_m/C_{α_0}).

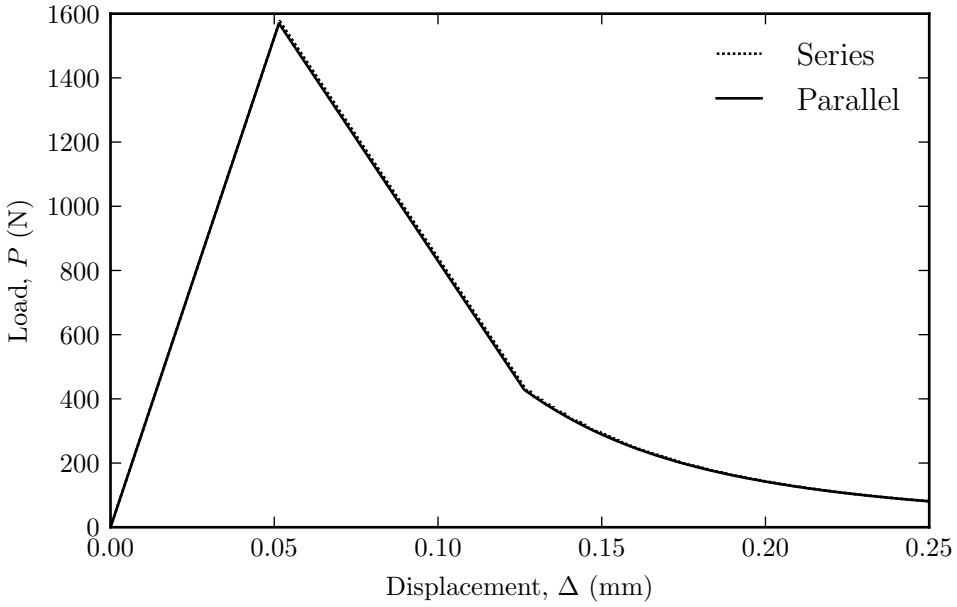

Figure 3.12: Load-Displacement model results with compact tension (C(T)) standard specimen geometry, for crack lengths $\alpha_0 = 0.2 \rightarrow 0.9$, with spring to initial specimen compliance ratio $C_m/C_{\alpha_0} = 2$. Direct comparison between series structure in displacement control and parallel structure in load control.

of the specimen is inherently stable across the range of possible initial crack lengths, this is not the case for most other specimen geometries.

Dimensionless equilibrium states can be used to examine the general behaviour of a specimen as can be seen in the equilibrium total energy in Figures 3.2, 3.3, with the dimensionless aspect underlining the limitation when examining size effects. Essentially, the availability of a greater total energy on the previous state, as always with respect to crack length, signifies an unstable transition. Additionally, the accumulation or non-expenditure of energy towards advancing the crack during the previous states, may alter the theoretical crack arrest point.

The introduction of a spring can assist to further examine the behaviour of specimen and structure in the presence of excess conditionally available energy. Choosing the C(T) specimen geometry is self-explanatory as it was shown to be the most stable in the total energy equilibrium. The model introduced highlights the differences with the equilibrium states as can be seen in any case of instability due to the follow-up energy of the spring, with specimen equilibrium states remaining the same as they are only a function of specimen

compliance ($z_{\mathrm{ll}}(\alpha)$) and stress intensity ($Y(\alpha)$). This snap-back behaviour of the structure in the equilibrium states is relevant when examining structures under conditions different than static loads, not the purpose of this work.

An emphasis must be given to the difference between structure and specimen when considering the displacement in the series model (displacement control). The structure always behaves as in displacement control, although more energy is accumulated, up to peak load, with increasing degree of spring to specimen compliance ratio. As initial fracture in the model occurs at peak load, based on $Y(\alpha)$, most of this excess energy is used to propagate the crack in an unstable manner. This draws attention to fracture resistance. A pre-peak fracture initiation or in the same manner a rising R-curve, truer to graphite's nature, would influence the threshold of instability and will be assessed in Chapter 5.

It was shown that, series and parallel spring structures behave in the same manner when in displacement and load control respectively (Figure 3.12). This informs part of the experimental program of the next chapter. Additionally, fulfilling another objective, the C(T) specimen was examined and was proposed as an ideal candidate for experimental parts in the following two chapters. The above was due to the inherent stability exhibited by that specimen and the ease of its use in a parallel configuration.

Chapter 4

Elastic follow-up effect

The aim of this chapter is to provide insight into the relevance of structure and associated degrees of elastic follow-up. Sets of experiments, with series and parallel (three bar) configuration, as seen in the previous chapter will be presented. By altering the base structure of the testing rig and subsequently its stiffness, the graphite specimens are loaded under various degrees of elastic follow-up and subsequently, crack stability may differ.

The effects of load multiaxiality, in stability and flexural strength come as a secondary aim of the chapter. The largest part of the experimental work will focus on biaxial and uniaxial tests, which based on the results seen in the bibliography remain quite uncertain. The applicability of Weibull and size effect will also be discussed and a distribution will be fitted to the flexural strengths derived from the uniaxial and biaxial experiments.

The above experimental results will be compared to the contradictory works done at the University of Manchester [104, 105], Birmingham [106] and Bristol [107]. Need for research on stress multiaxiality comes from the operational conditions of graphite bricks. Multiaxial states can be due to internal stresses from irradiation dimensional change or thermal strains with stress concentrators such as keyways further affecting their multiaxiality [108], as noted by Mostafavi *et al.* [105].

Additionally, a parallel configuration experiment will be presented, also with an associated degree of elastic follow-up. The behaviour of the specimens in the configuration will be accessed, in comparison to an independent one and corrections on the method will be discussed.

4.1 Biaxiality experiment, series

To evaluate the effect of load multiaxiality, 3 point beam bend and 5 point cruciform bend tests were used. Additionally, to alter the associated degree of elastic-follow up, the specimens were loaded against rigs of various materials and thus stiffness.

4.1.1 Background

Mostafavi *et al.* [104, 105] examined the effects of equibiaxial loading on the flexural strength, crack initiation and crack propagation in Gilsocarbon graphite. The specimens were uniaxially loaded in four-point bending and equibiaxially using a ring-on-ring test rig. The estimated flexural strength on the equibiaxial ring-on-ring was found to about 18 % lower than uniaxial flexural strength.

Novovic and Bowen [106] examined the biaxial strength of two types of nuclear graphites. Contrary to the results by Mostafavi *et al.*, the flexural strength, for Gilsocarbon, under the equibiaxial state (ring-on-ring) was found 6 to 16 % greater compared to the uniaxial four-point bend strength. Also mentioned in their study was the differences in strength exhibited with size, mainly in the additional uniaxial test dataset provided, with a reduction in strength with the cross-sectional increase.

Liu *et al.* [107] looked into the failure loads at three different biaxiality ratios by changing the roller configuration in the loading rig used between the extremes of 1 : 1 to the uniaxial 1 : 0, with the intermediate 6 : 7. Results by Liu *et al.* focused on load to failure and the acoustic events and showed an increase of about 30 % to the load required in the same specimen based on the configuration (5.4 kN for 1 : 1 and 4.2 kN for 1 : 0). The above, although not part of the original work could be calculated with the help of FE as a 20 % (25 MPa to about 30 MPa) increase in failure stress from equibiaxial to uniaxial for the same specimen geometry, in agreement with the results from Mostafavi *et al.*. Simple beams (Figure 4.1b) loaded in the same manner as the other specimen in the experimental work showed a strength of about 25 MPa (2.6 kN). During the experiment, acoustic emission events were recorded through four resonance transducers and confirmed the presence of microcracking well prior to final failure.

Based on the above, an experimental plan is proposed to evaluate graphite's

flexural strength. Also, based on the cracking prior to peak load or failure, use of different structures is suggested in assistance towards the study of elastic follow-up.

4.1.2 Design

Specimen

Figure 4.1 shows the design of the two graphite specimens, with Figure 4.1a being the biaxial and Figure 4.1b the uniaxial specimen.

The biaxial specimen is similar to the design used by Liu *et al.* [107], sharing a length of 150 mm symmetrical across its two centre axes with a 50 mm width for each arm, albeit with some refinements. The smaller radius (10 mm) on the corners of the cruciform in the original work may produce unwanted high stress concentrations. In Figure 4 of the original work by Liu *et al.*, the fracture paths of the Gilsocarbon specimen are shown with specifically Figure 4a and Figure 4b (1 : 0 ratio) showing a fracture path through the corners and not the centre of the cruciform specimen. In an FE analysis it can be shown that for the case of 10 mm radius and the properties seen in Table 3.2, the maximum principal stress at the corner is about 17 % higher than the centre. For a Poisson's ratio of 0.3, the stress between corner and centre is about the same. Thus to avoid concentration in the corners, a radius of 25 mm was chosen, which according to FE results in about 20 % greater stress in the centre.

The uniaxial specimen was designed in accordance to the cruciform, as to be able to use the same base structure and can be seen in Figure 4.1b. It spans 150 mm and is 50 mm in height with a thickness of 20 mm.

The specimens were made from Gilsocarbon graphite, the same type used by the background literature provided above. The graphite was extracted from a stock AGR reactor core block provided by EDF Energy. Extraction from the block as well as machining of the specimens was done by Erodex Ltd. A total of 12 uniaxial and 12 biaxial specimens were extracted, machined and tested.

By applying a displacement at the centre of each of the specimens (black dots in Figure 4.1) and validating with the use of FE, the location of maximum tensile stress is at the middle of bottom surface and the maximum compressive stress will be at the centre of the top surface. Although Gilsocarbon due to its microstructure and irregularities may fail far away from the point of maximum

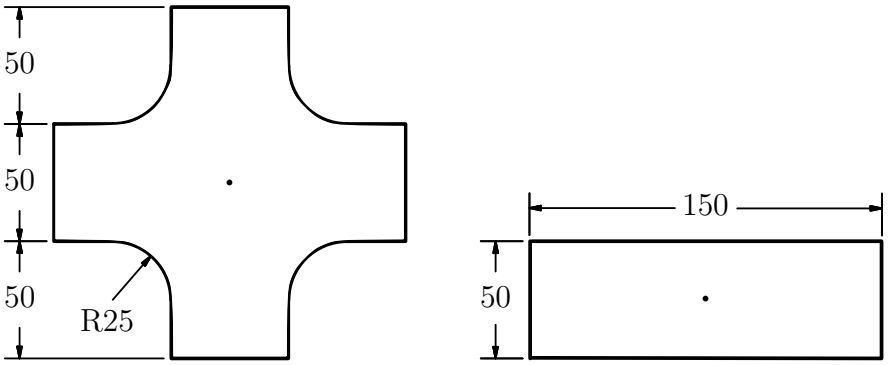

(a) Cruciform (b) Beam

Figure 4.1: Experimental specimens with dimensions. (a) Biaxial cruciform test specimen, (b) Uniaxial beam test specimen. All dimensions in mm, to scale. Thickness for both is 20 mm. Black dot represents the loading location.

stress, due to the concentration achieved with the radius of 25 mm, this is highly unlikely.

Base structure

The role of the base structure is to alter the levels of relative stiffness and thus the degree of elastic follow-up in testing. The loading of the graphite specimens on top of the base structure can be expressed as specimen and spring in series, shown in Figure 3.4a, with the structure being the equivalent spring.

Both the graphite specimen and the structure will be loaded against the cross head displacement of the machine as modelled earlier. Due to microcracking and other energy absorption mechanisms, it is expected for graphite to experiene a "graceful failure" as a quasi-brittle material. Theoretically, the structures will provide different amounts of follow-up energy while the specimen's compliance increases. This energy will affect, as earlier shown, the behaviour of the specimen.

The base structure is similar to the aluminium design used in the experiments by Liu and can be seen in Figure 4.2. Rollers of 10 mm are placed in the grooves shown in the drawing to get line contact on both specimens. There is a single roller configuration (1 : 1), for an equibiaxial testing of the cruciform specimens. For the uniaxial loading test, 2 of the rollers are simply used.

To achieve an appropriate range in stiffness, the base structures were made with 3 different materials: Steel, Aluminium and Poly(methyl methacrylate) (PMMA) giving a stiffness of $37 \times 10^3\,\mathrm{kN\,mm^{-1}}$, $12.5 \times 10^3\,\mathrm{kN\,mm^{-1}}$ and

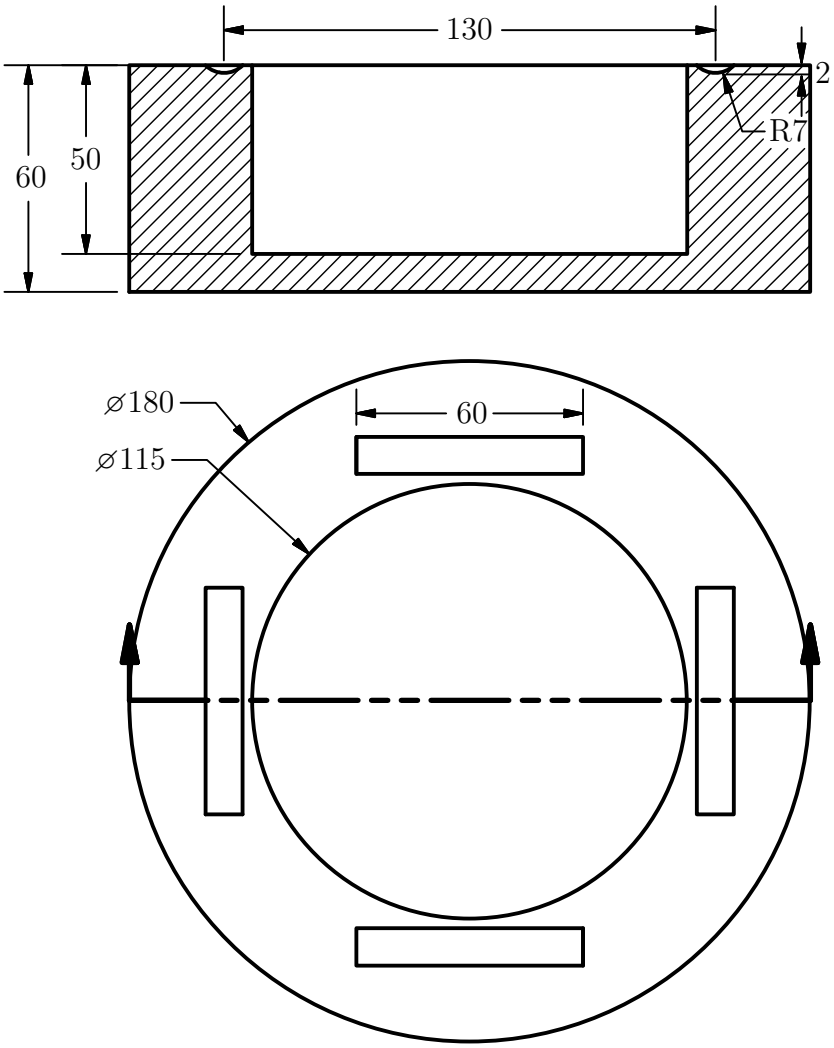

Figure 4.2: Base structure drawing with cross-section, detail on the 10 mm roller positions, radius 7 mm and depth 2 mm. All dimensions in mm, to scale.

$0.5 \times 10^3\,\mathrm{kN\,mm^{-1}}$ respectively, calculated in Autodesk Inventor. There were 4 uniaxial and 4 biaxial specimens that were loaded against each structure.

4.1.3 Setup and procedure

Strain gauges

Strain gauges were attached on the opposite side of the loading point to each of the graphite specimens (black dots in Figure 4.1). All purpose, Vishay C2A-06-250LW-350 uniaxial strain gauges were attached to the specimens using the recommended by Vishay M-Bond 200 fast curing adhesive. Based on the

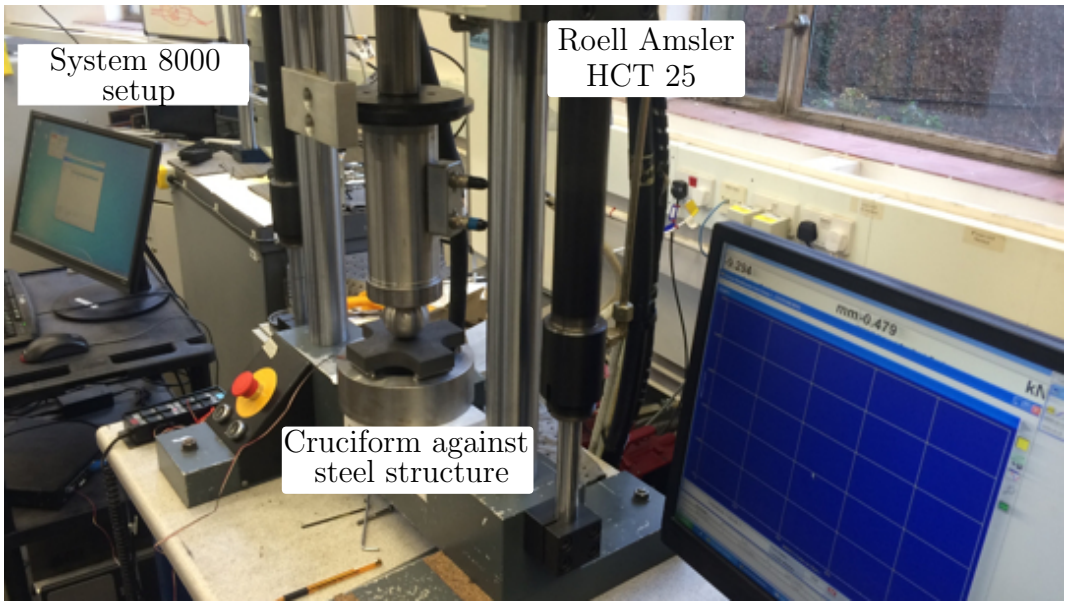

Figure 4.3: Overview of the experimental biaxial setup.

assumption that the two principal strains are equal for the equibiaxial test, a single uniaxial strain gauge per specimen was used.

Setup

A Roell Amsler (Zwick Roell) HCT 25 (25 kN) hydraulic testing system was used with an Instron 8800MJ testing controller, calibrated to standard [109] by Instron Laboratory. The maximum load of 25 kN was well beyond the expected failure load of about 7 kN for the biaxial specimens and 2.6 kN for the uniaxial load based on the work by Liu *et al.* [107]. The load was applied to the middle of the specimens using a machined steel ball with a diameter of 60 mm. A VPG System 8000 data acquisition system was used to record 4 variables. These included, time, uniaxial strain, load and displacement. Load and displacement values were passed to the System 8000 from the Roell Amsler and the Instron controller where they were also being recorded, acting as a safety measure for the case of a corrupt data file.

An overview of the biaxial setup can be seen in Figure 4.3

Procedure

There were 4 uniaxial and biaxial tests that were carried out on each of the 3 base structures at a rate of 0.04 mm min^{-1}. The data collected on the System

8000 and the Roell Amsler were exported into .CSV format files and then imported and analysed in Python [110].

4.2 Results and analysis

4.2.1 Uniaxial

Load-displacement

To observe if changing the base structure in the tests altered the elastic follow-up in the testing of the uniaxial specimens, the force displacement graphs for the uniaxial specimens for different base structures is shown below in Figure 4.4, 4.5, 4.6. Stiffness was calculated by linear regression over a part of the load-displacement line and plotted with a dashed line, with all the relevant values summarised in Table 4.1. For the steel structure (Figure 4.4) total stiffness of the system was of about 3.33 to 3.84 $\mathrm{kN\,mm^{-1}}$. For the aluminium structure (Figure 4.5) total stiffness for three of the tests was about 3.63 to 3.75 $\mathrm{kN\,mm^{-1}}$ and with one extreme of 4.31 $\mathrm{kN\,mm^{-1}}$. For the PMMA structure (Figure 4.6) total stiffness for three of the tests was of about 3.41 to 3.50 $\mathrm{kN\,mm^{-1}}$ with the exception of an outlier with 3.91 $\mathrm{kN\,mm^{-1}}$.

This outlier is to be taken from the dataset for the subsequent analysis as it was also shown to be slightly misaligned during the experiment (loading ball trace). The mean failure load was $2.446 \pm 0.098\,\mathrm{kN}$ with the average failure loads and standard deviations for the specimens loaded against the steel, aluminium and PMMA base structure were $2.501 \pm 0.119\,\mathrm{kN}$, $2.397 \pm 0.077\,\mathrm{kN}$ and $2.438 \pm 0.036\,\mathrm{kN}$ respectively.

The area under the curve or the accumulated energy was also calculated. The values presented in table 4.1 come from the area of the triangle formed by the dashed line (stiffness) up to the peak load. A comparison between the area calculated as the triangle and the area from the trace or the interpolation of the load-displacement up to the peak load showed very small discrepancies ($< 2\,\%$). The mean energy was 0.822 N m with a standard deviation of 0.07 N m. For the individual structures of steel, aluminium and PMMA it was $0.84 \pm 0.08\,\mathrm{N\,m}$, $0.76 \pm 0.02\,\mathrm{N\,m}$ and $0.88 \pm 0.04\,\mathrm{N\,m}$ respectively.

Table 4.1: Uniaxial test data

Material	Peak Load (kN)	Slope ($\mathrm{kN\,mm^{-1}}$)	Area under curve (N m)
Steel	2.536	3.67	0.888
	2.668	3.84	0.840
	2.338	3.61	0.717
	2.462	3.33	0.913
Aluminium	2.506	4.31	0.760
	2.288	3.63	0.727
	2.408	3.75	0.784
	2.387	3.71	0.778
PMMA	2.388	3.50	0.827
	2.474	3.43	0.904
	2.452	3.41	0.908

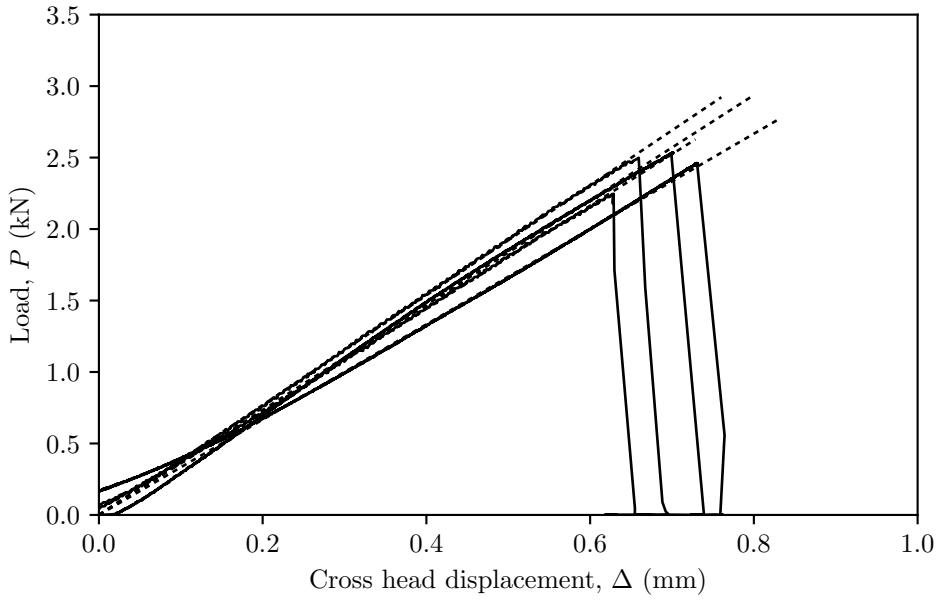

Figure 4.4: Load-Displacement graph for the uniaxial specimens, under displacement control, on the steel base structure.

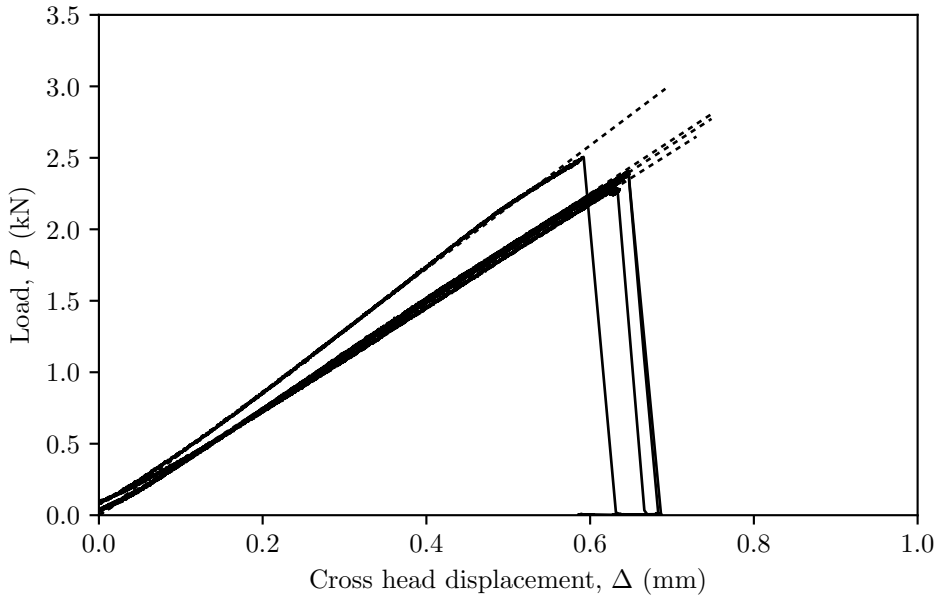

Figure 4.5: Load-Displacement graph for the uniaxial specimens, under displacement control, on the aluminium base structure.

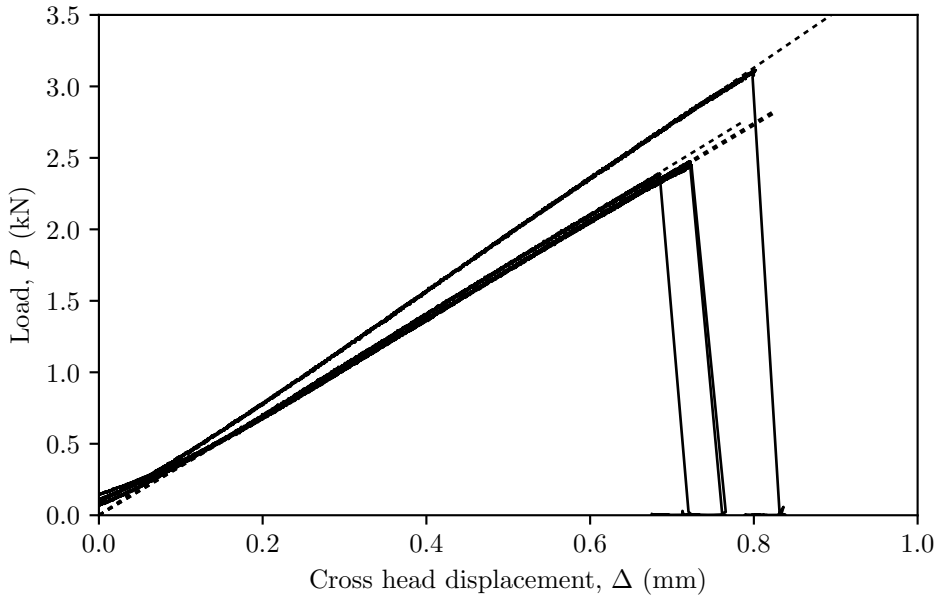

Figure 4.6: Load-Displacement graph for the uniaxial specimens, under displacement control, on the PMMA base structure.

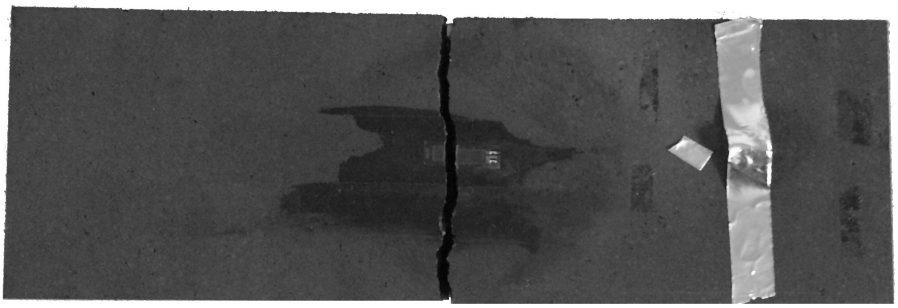

Figure 4.7: Fracture path exhibited in all uniaxial specimens.

Fracture paths

Figure 4.7 shows one of the uniaxial specimens post fracture. The fracture paths are at a 90°, vertical (50 mm) through the centre, for all of the specimens.

4.2.2 Biaxial

Load-displacement

Same as above, to observe the effect of changing the base structure the load-displacement graphs for the biaxial specimens are plotted separately, for the steel structure in Figure 4.8, for the aluminum one in Figure 4.9 and the PMMA one in Figure 4.10. Stiffness was calculated and plotted with a dashed line in the same manner as in the uniaxial tests. For the steel structure (Figure 4.8) total stiffness for three of the tests was of about 6.87 to 7.61 $\mathrm{kN\,mm^{-1}}$. For the aluminium structure (Figure 4.9) total stiffness for two of the tests was about 7.23 to 7.26 $\mathrm{kN\,mm^{-1}}$ and two outlier values of 8.19 $\mathrm{kN\,mm^{-1}}$ and 8.66 $\mathrm{kN\,mm^{-1}}$. For the PMMA structure (Figure 4.10) total stiffness for the tests was about 6.18 to 6.64 $\mathrm{kN\,mm^{-1}}$. The outlier values for the aluminium structure base are to be taken from the dataset for the subsequent analysis as they were also slightly misaligned during the experiment (loading ball trace).

The mean failure load was $5.298 \pm 0.266\,\mathrm{kN}$ with the average failure loads and standard deviations for the specimens loaded against the steel and PMMA base structure at $5.390 \pm 0.157\,\mathrm{kN}$ and $5.320 \pm 0.305\,\mathrm{kN}$ respectively.

The area under the curve or the accumulated energy was also calculated in the same manner as in the uniaxial and can be seen in table 4.2. The mean energy was $2.06 \pm 0.22\,\mathrm{N\,m}$ with steel and PMMA $2.02 \pm 0.14\,\mathrm{N\,m}$ and

Table 4.2: Biaxial test data

Material	Peak Load (kN)	Slope ($kN\,mm^{-1}$)	Area under curve (N m)
Steel	5.558	6.87	2.248
	5.268	7.24	1.938
	5.201	7.32	1.870
	5.535	7.61	2.025
Aluminium	4.851	7.26	1.644
	5.292	7.23	1.959
PMMA	5.035	6.32	2.022
	5.008	6.18	2.065
	5.711	6.64	2.339
	5.527	6.37	2.464

2.22 ± 0.18 N m respectively.

Fracture paths

The two types of fracture paths of the biaxial specimens are shown in Figure 4.11. Ten out of the twelve exhibited a typical path of fracture shown in Figure 4.11a, where there was a single path at 45° across the centre, extending to the proximity of the corners. The two specimens with the aluminium base that showed a post-peak response (Figure 4.9), followed a path seen in Figure 4.11b. A branching crack path at the centre, with each path extending towards the corner areas.

4.2.3 Finite element analysis

From the experiment, load, cross head displacement and maximum strain (based on location) through the strain gauge were obtained. However, the principal stresses are required to compare between uniaxial and biaxial as proposed by Sato [111] where, for near isotropic graphite (IG-11) under a multiaxial stress state the maximum principal stress can be invoked as the failure criterion. To obtain these stresses finite element models of both tests were created.

The aim of the model was to find a constant of proportionality between the applied load and the maximum principal stress on the opposite surface. The material was modelled with a constant Youngs modulus of 10 GPa and a Pois-

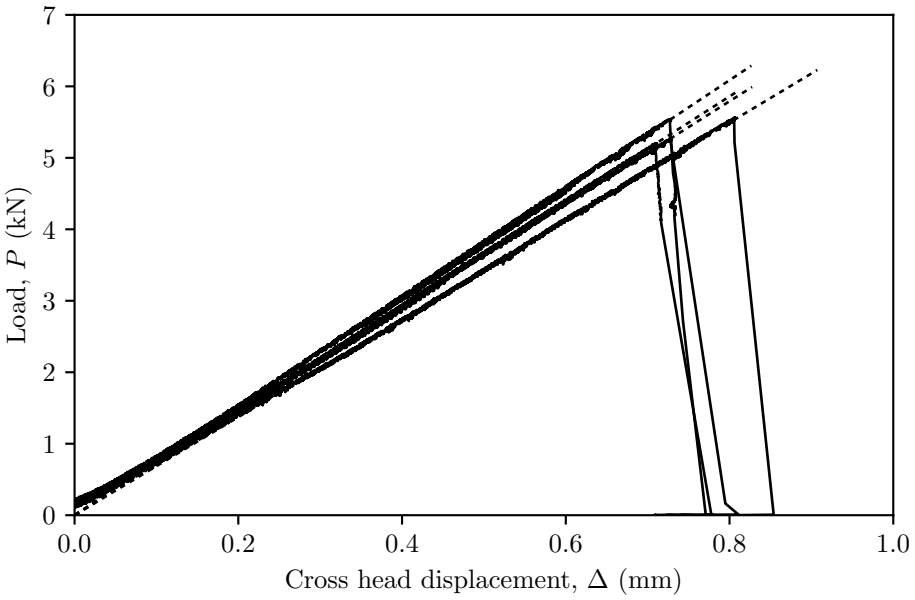

Figure 4.8: Load-Displacement graph for the biaxial specimens, under displacement control, on the steel base structure.

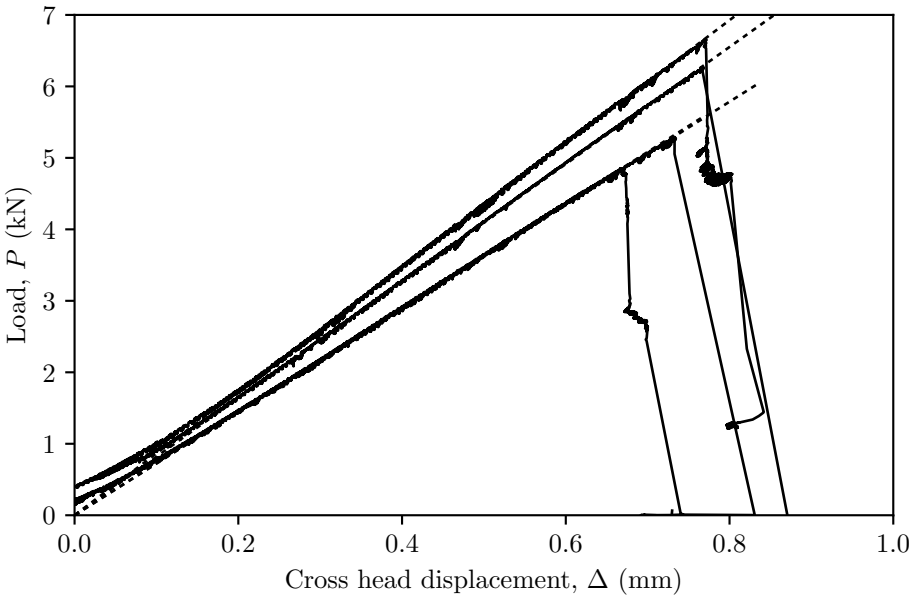

Figure 4.9: Load-Displacement graph for the biaxial specimens, under displacement control, on the aluminium base structure.

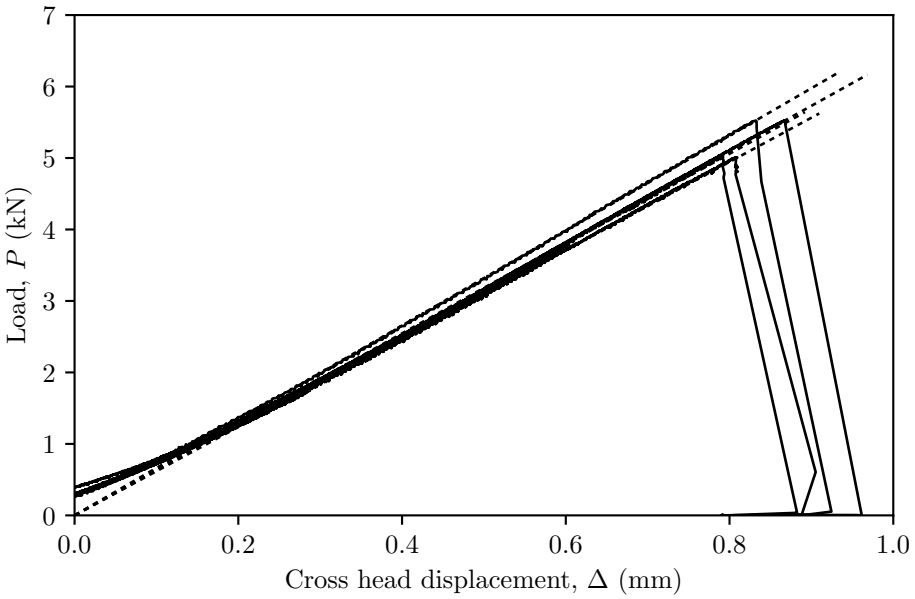

Figure 4.10: Load-Displacement graph for the biaxial specimens, under displacement control, on the PMMA base structure.

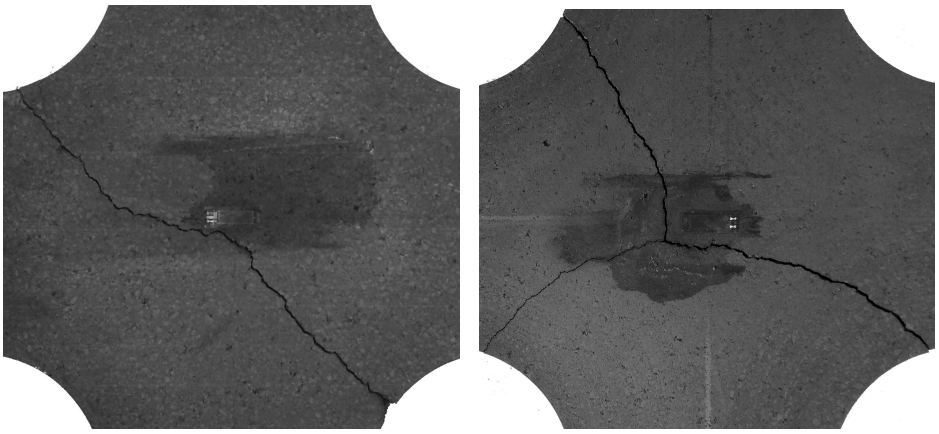

(a) Single path (b) Branched path

Figure 4.11: Fracture paths exhibited in the biaxial specimens. (a) Single path seen in 10 out of 12 experiments, (b) Branched path.

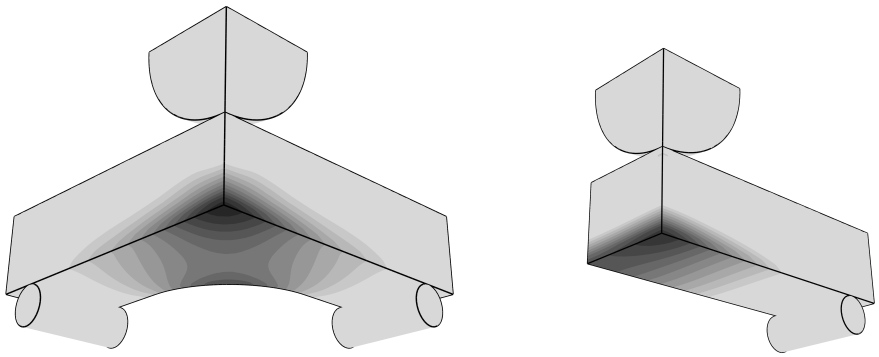

(a) Cruciform (b) Beam

Figure 4.12: Finite element simulation; quarter model contour plot of maximum principal stress for (a) Equibiaxial cruciform and (b) Uniaxial beam. A quarter of the roller supports and loading ball can be seen as well. Stress concentrated in the centre darker area.

son's ratio of 0.22 when the results from the experiment and bibliography [103] show a gradual softening in Gilsocarbon graphite. Although important for the validity of the specific values of load and strain the choice of Youngs modulus does not have a large effect on the constant ratio between reaction force and maximum stress. This can be validated by using different values of E and comparing the ratios. A difference of less than 0.1 % can be seen between a modulus of elasticity of 8 GPa and 10 GPa.

Assumptions & Variables

To create these finite element models and to extrapolate the values of stress corresponding to a load or displacement the following assumptions were made:

- The maximum stress in both the uniaxial and biaxial specimens for any given load was proportional to that load.
- The supports and loading apparatus (ball punch) were treated as rigid bodies and modelled with a modulus of elasticity of 200 GPa.
- All contacts, ball-specimen and specimen-rollers were frictionless.

Model

A quarter model was made in Abaqus CAE 6.12 using C3D8R linear brick elements with reduced integration. From the supporting structure only the

rollers, which were constrained from moving, were used as to simulate the line contact (interaction between surfaces). The rest of the structure was assumed to be rigid and was excluded from the analysis for simplification purposes.

To create a load between the quarter of ball and specimen, the ball was initially constrained in contact on top of the specimen at the ideal loading point and displaced in small increments until a final displacement of 0.8 mm. Reaction force, displacement, relevant stresses and strain were all recorded in intervals. The model was run with variable element sizes until the results converged to a certain level of accuracy (1 to 2 % difference in stress/reaction force) to achieve an acceptable result without the use of unnecessary computing time.

Validation

A comparison of the results produced by the finite element model and a known solution was needed to validate the model. Although, Hertz theory on contact mechanics is able to describe the stresses between sphere and surface [112], this is not needed as the maximum principal stress and failure location would be on middle of the opposite surface. The ratio of reaction force and principal strain was used to validate the model and compared with the experimental values of force and strain. The values of principal strain were taken from the location of the strain gauges attached to the specimen.

As shown in the bibliography [113], a clear softening response towards the peak load can be seen in graphite. Due to this response, the initial part of strain ($\approx$ 20 % of total strain) where strain rates were relatively constant, was used to compare between model and experiment. Also, the location of maximum strain and the concentration of measurements, where the gauges were attached could produce irregularities during higher loads (fracture zone). Figures 4.13 and 4.14 show the load-strain graphs for the uniaxial biaxial specimens up until 600 $\mu\epsilon$. In the uniaxial specimens (Figure 4.13) the average initial load-strain gradient was 1.00 ± 0.06 N/$\mu\epsilon$, the finite element model gave a gradient of 1.05 N/$\mu\epsilon$. In the biaxial specimens (Figure 4.14) the average initial gradient was found to be 2.34 ± 0.31 N/$\mu\epsilon$, in the range 0 to 600 $\mu\epsilon$, the finite element model gave a gradient of 2.8 N/$\mu\epsilon$. For the initial 200 $\mu\epsilon$ the gradient of the experimental data was 2.7 ± 0.6 N/$\mu\epsilon$ and in the range 200 to 600 $\mu\epsilon$, 2.2 ± 0.2 N/$\mu\epsilon$. In both the uniaxial and biaxial specimens the gradient

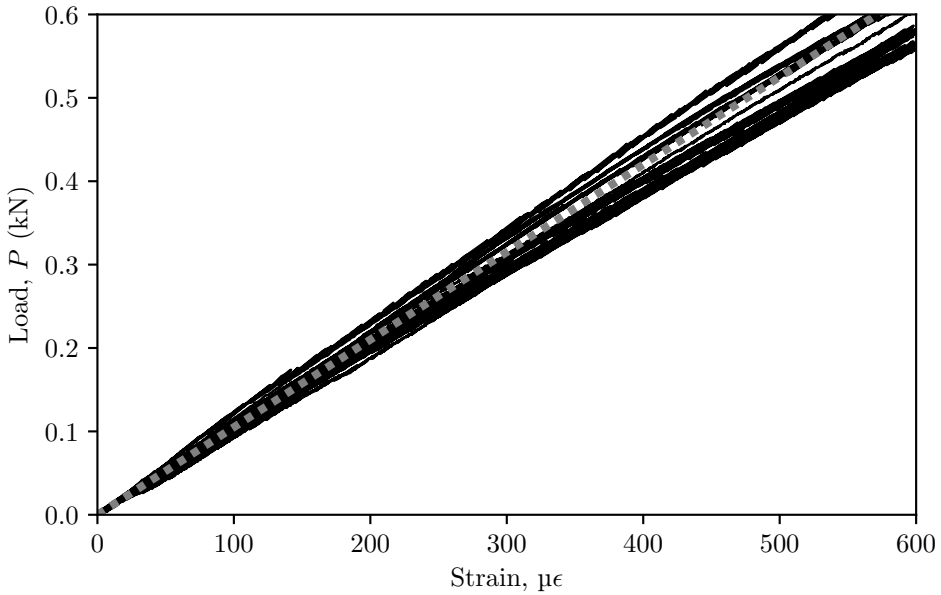

Figure 4.13: Load-Strain (longitudinal surface strain) graph for the uniaxial specimens, on all base structures with the grey dashed line being the finite element model's prediction.

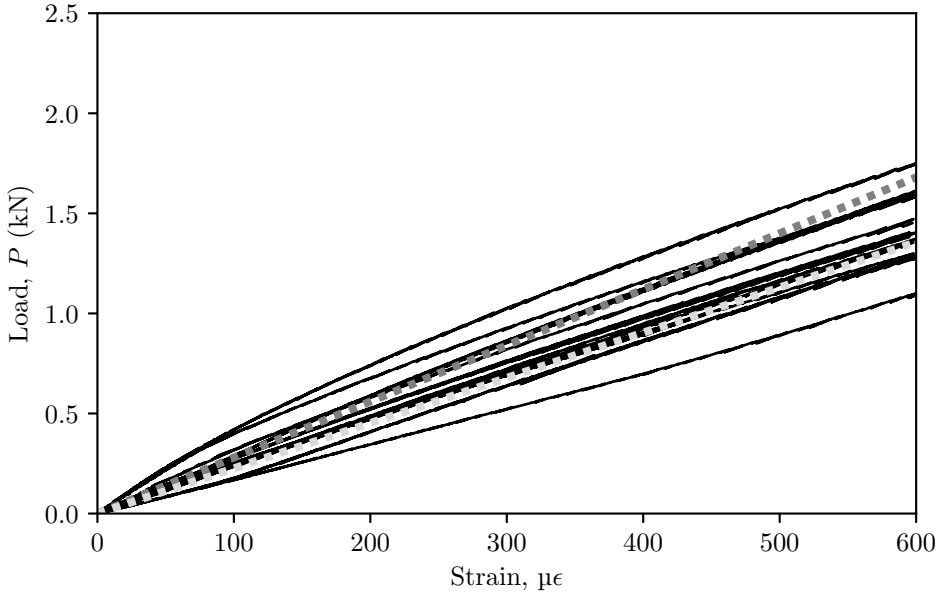

Figure 4.14: Load-Strain (longitudinal surface strain) graph for the biaxial specimens, on all base structures with the grey dashed line being the finite element model's prediction. Brighter grey denotes model with a lowered Young's modulus of 8 GPa.

of the load-strain graph from the finite element model lied within 1 standard deviation from the average of the initial gradients of the experimental results, therefore the model can be assumed to be valid.

A study on the effect of both the Young's modulus and Poisson's ratio was also done by altering the values within a logical limit. Although, for the biaxial specimen, the ratio of reaction force to strain showed a linear decrease with the decrease of Young's modulus ($\approx 20\,\%$ for $E = 8\,\mathrm{GPa}$), the ratio of maximum principal stress to reaction force remained the same. This is shown with a brighter dashed grey line in graph 4.14.

4.2.4 Flexural strength

The constants of proportionality between force and applied load can be used to get the flexural strengths from maximum principal stress in the uniaxial and biaxial specimens based on their peak load from Tables 4.1 and 4.2 respectively. Based on the finite element model for the uniaxial case the ratio was found to be $9.3\,\mathrm{MPa\,kN^{-1}}$ and for the biaxial case $4.35\,\mathrm{MPa\,kN^{-1}}$. The specimens were sorted in both the equibiaxial and uniaxial data sets based on their strength. Probability of failure for each (i), P_f, was calculated by:

$$P_f = \frac{i - 0.5}{N} \tag{4.1}$$

with N being the total number of specimens in each data set. A two-parameter Weibull distribution (m,σ_w) was fitted to the data of flexural strength with SciPy in Python (scipy.stats.weibull_min) [114] and also plotted [115] using the equation below:

$$P_f = 1 - \exp\left(-\frac{\sigma_b}{\sigma_w}\right)^m \tag{4.2}$$

The specific distribution was chosen to enable direct comparison with the data from Mostafavi *et al.* [105] and due to its general versatility (two-parameters). The Weibull distributions for the flexural strength in the uniaxial and biaxial specimens are shown in Figure 4.15. It was found that under uniaxial load $\sigma_w = 23.20\,\mathrm{MPa}$ and $m = 23.29$ where under equibiaxial load $\sigma_w = 23.64\,\mathrm{MPa}$ and $m = 22.86$.

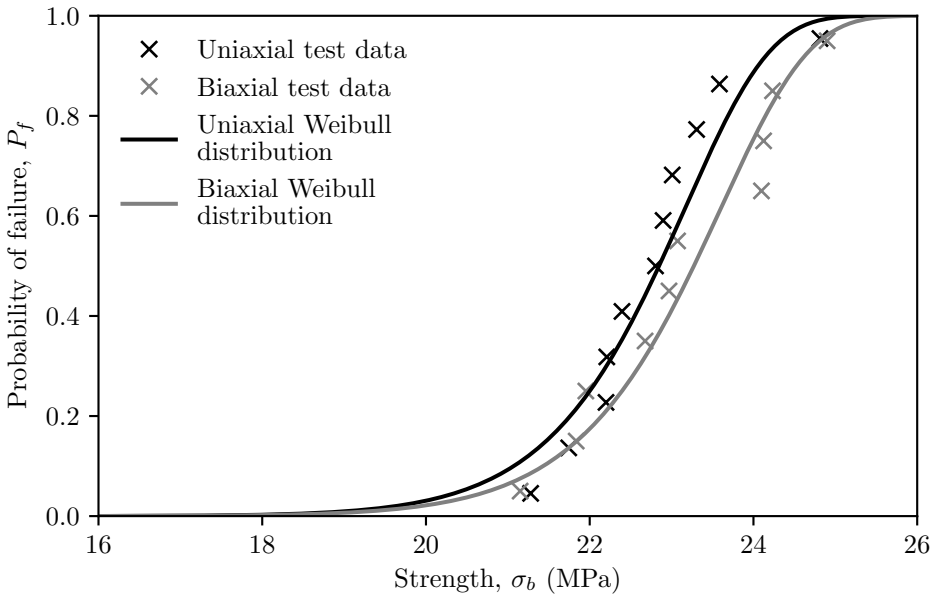

Figure 4.15: Two parameter cumulative Weibull distribution of the flexural uniaxial and biaxial strength. Under uniaxial load: $\sigma_w = 23.20\,\text{MPa}$, $m = 23.29$; equibiaxial load: $\sigma_w = 23.64\,\text{MPa}$, $m = 22.86$

4.2.5 Elastic modulus

Figures 4.16 and 4.17 show the elastic modulus with respect to strain on the specimen, for uniaxial and biaxial respectively, as recorded by the strain gauges. A rolling linear regression function (least squares regression) was written to calculate the elastic modulus. This rolling function has a specific window size and starts from the first point of the strain/load data set. The load is multiplied by the ratios found above ($9.3\,\text{MPa}\,\text{kN}^{-1}$ for uniaxial and $4.35\,\text{MPa}\,\text{kN}^{-1}$ for biaxial). The slope of the stress strain would approximate the elastic modulus for the size of the window. There is a discrepancy between elastic modulus and strain as the strain used to plot the graph is the first value of strain in the rolling window rather than a median or an expected value from the regression. Also, the linear regression is calculated with an intercept despite the elastic relationship between stress and strain.

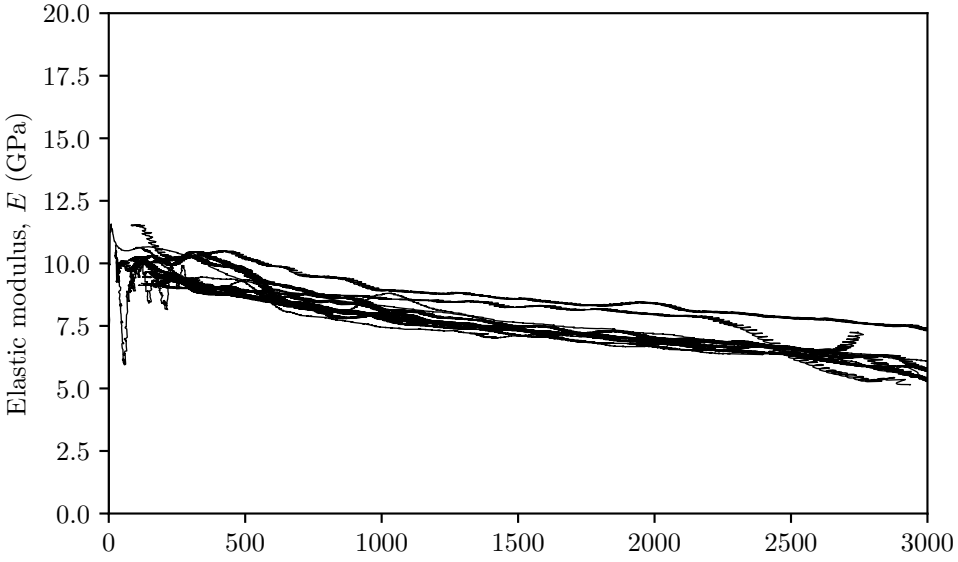

Figure 4.16: Elastic modulus-Strain graph for all uniaxial specimens.

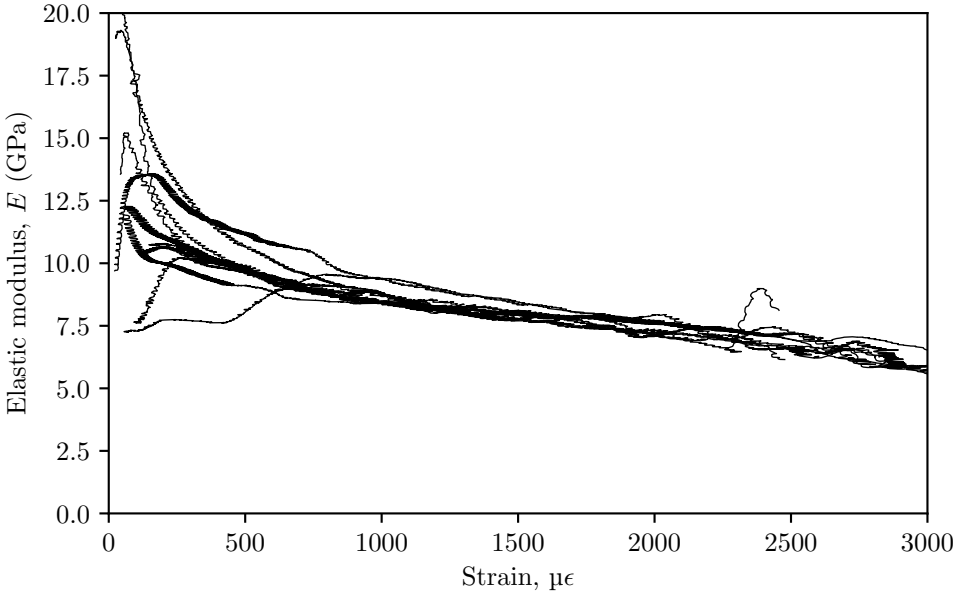

Figure 4.17: Elastic modulus-Strain graph for all biaxial specimens.

4.3 Three bar experiment, parallel

Another set of experiments on the follow-up of elastic energy will be presented in this section. The parallel model, or three bar structure, will be used, as can be seen in Figure 3.4b. The aim of this preliminary experiment was to map a method to evaluate the threshold of stability in Gilsocarbon graphite either by changing specimen compliance (initial α) or by changing the material of the outer bars of the parallel system. These tests are presented to underline the difficulties and the necessary steps needed for future work on the matter, as well as an argument on the choice of the experimental work presented on the next chapter.

4.3.1 Design

To evaluate stability conditions and fracture properties, fracture tests on specimens were performed with the addition of outer bars. This addition, as explained in Chapter 3 will alter the additional energy provided by the system, based on their relative stiffness to the specimen.

Specimen

A standard compact tension specimen was chosen, as inherently being the most stable, shown in the total energy equilibrium of Chapter 3. The specimens were made from Gilsocarbon graphite, the same type used by the background literature provided above. The graphite was extracted from a stock block provided by EDF Energy. Extraction from the block as well as machining of the specimens was done by Erodex Ltd with dimensions specified from ASTM-399 [94] and an $\alpha_0 = 0.5$. Width of the specimen was 50 mm and breadth was 25 mm.

Three bar rig

Two bases (Figure 4.18) were used to hold the two outer bars and the specimen together. The bases were made out of mild steel with two slots measuring a radius of 10.5 mm for the insertion of the outer bars. Two bars ($n_{\text{out}} = 2$) were chosen for symmetry as well as the ability to go into lower ratios of stiffness ($n_{\text{out}}k_{\text{out}}/k_{\text{spec}}$). The bars are to be secured into the holes with nuts and washers

on the top and bottom side. One of the two holes has been extended to the edge for ease of instalment of the bars while the specimen was in place. The general purpose of the base rig is for outer bars to be swapped in order to achieve different compliance ratios.

Outer bars

Firstly, an estimate on the desired range of stiffness ratio had to be chosen. The upper limit would not pose a problem as the graphite specimen is of lower Young's modulus to most metals and thus could easily reach high ratios of stiffness. The lower limit of ratios could pose a problem without sacrificing more initial crack length on the specimen. Knowing the elastic C(T) specimen solutions by Towers [116] also found in [28,31,61], with the dimensions mentioned above ($E \approx 10\,\mathrm{GPa}$, $W = 50\,\mathrm{mm}$, $B = 25\,\mathrm{mm}$ and $\alpha_0 = 0.5$) the specimen's initial stiffness is about $6.5\,\mathrm{kN\,mm^{-1}}$, based on the load line displacement.

Poly(methyl methacrylate) (PMMA) was chosen as an ideal material for the outer bars having a Young's modulus of about 2.8 to 3.75 GPa and a minimum stress where crazing starts to appear of about 30 to 40 MPa [117,118]. Based on the above properties, each bar, diameter of 10 mm and length of 100 mm, would have a theoretical stiffness value of 2.2 to $2.9\,\mathrm{kN\,mm^{-1}}$ and able to withstand a load of at least 2.4 kN.

With the above range of outer bar stiffness and the specimen being known, the ratio of compliance ($n_{\mathrm{out}}C_{\mathrm{out}}/C_{\mathrm{spec}}$) is about 1.1 to 1.5 .

4.3.2 Setup and procedure

Setup

A Shimadzu AGS-X 10 kN dual column electromechanical machine was used for this experiment. The machine was calibrated to standard [109] by Instron Laboratory. Test control and data acquisition (time, load and cross head displacement) was done through Trapezium X software.

Specific intricacies presented themselves during the setup of the three bar with the outer bars. The specimen had to be secured in position with loading pins before installing and tightening the nuts on the bars. Tightening the nuts proved to be a difficult task due to the coarse pitch of the M10 thread and even a quarter turn would displace the specimen by about 0.4 mm. Due to the

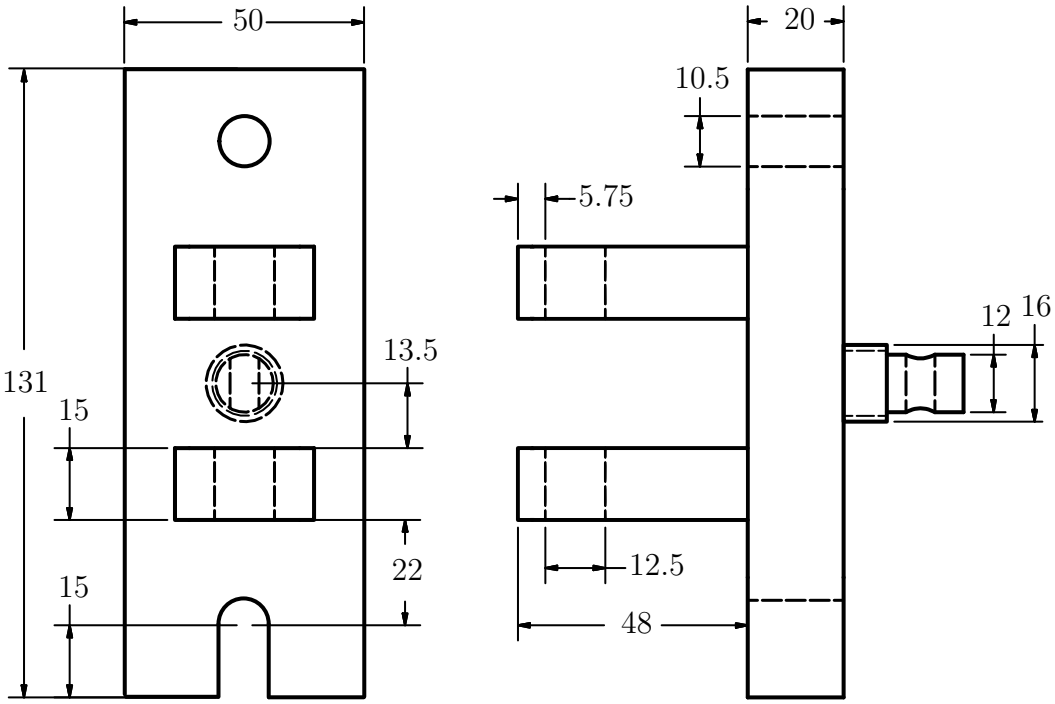

Figure 4.18: Design of base structure housing bars and specimen made from mild steel. All dimensions in mm, to scale.

above it was decided not to overly secure the nuts. Washers were also placed between nuts and base, specifically important for the slotted side. An overview of the three bar setup can be seen in Figure 4.19.

Procedure

Two compact C(T) specimen were tested. The first was a single C(T) without the use of outer bars in the structure. It was loaded in displacement control at a rate of $0.1\,\mathrm{mm\,min^{-1}}$. For the second C(T), PMMA outer bars were used as explained above. The structure was loaded in load control at a rate of $10\,\mathrm{N\,min^{-1}}$. Both specimens were loaded to failure.

4.3.3 Results

Load-displacement

The load-displacement graphs for both cases (single C(T) specimen and specimen with outer bars) are shown in Figure 4.20. As can be seen from the figure, the C(T) specimen in the three bar takes most of the load up to about 300 N.

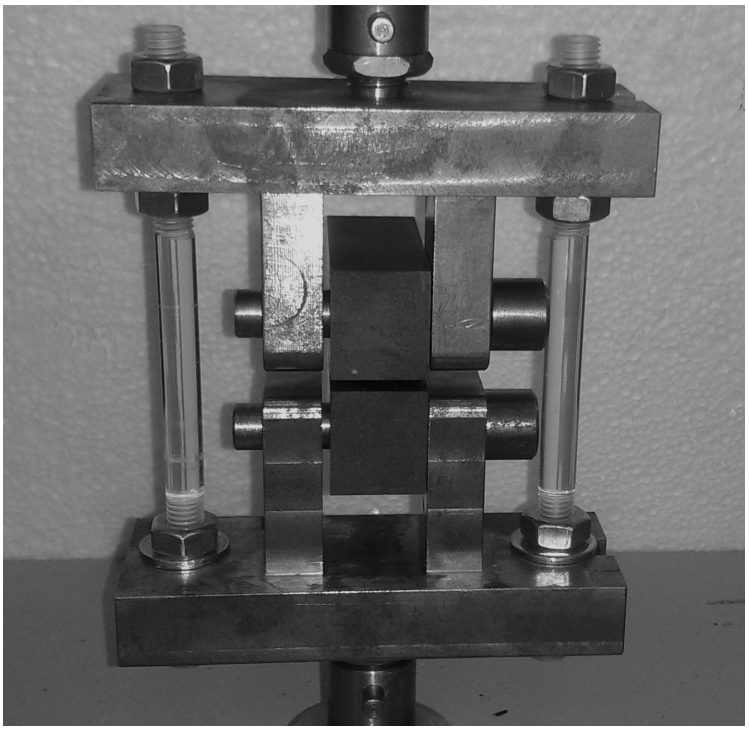

Figure 4.19: Three bar structure configuration close up with PMMA outer bars and a Gilsocarbon graphite compact C(T) specimen.

This initial slope, based on load and cross head displacement, of the three bar C(T) coincides with the single specimen at about $3.15\,\mathrm{kN\,mm^{-1}}$ with less than 0.5 % difference. With the slack of the outer bars taken out, the structure, now with a slope of about $4.3\,\mathrm{kN\,mm^{-1}}$ is loaded up until specimen fracture.

After most of the fracture process, the outer bars take most of the load, as can be seen in Figure 4.20, about 0.5 mm of cross head displacement onwards. Then, the slope of the outer bars is about $1.7\,\mathrm{kN\,mm^{-1}}$.

Comparison

To directly compare specimen behaviour, results from Figure 4.20 need to be calibrated for the initial loading of the specimen in the case of outer bars. By definition, in a the parallel structure displacement is shared between bars and specimen. Thus, theoretically, the specimens in both cases should reach their peak load at about the same displacement. By substituting the difference of cross head displacement at peak load for the two cases from the structure with the outer bars, both cases share the same displacement albeit with an additional load for the case of the outer bars. Detail of the comparison of the

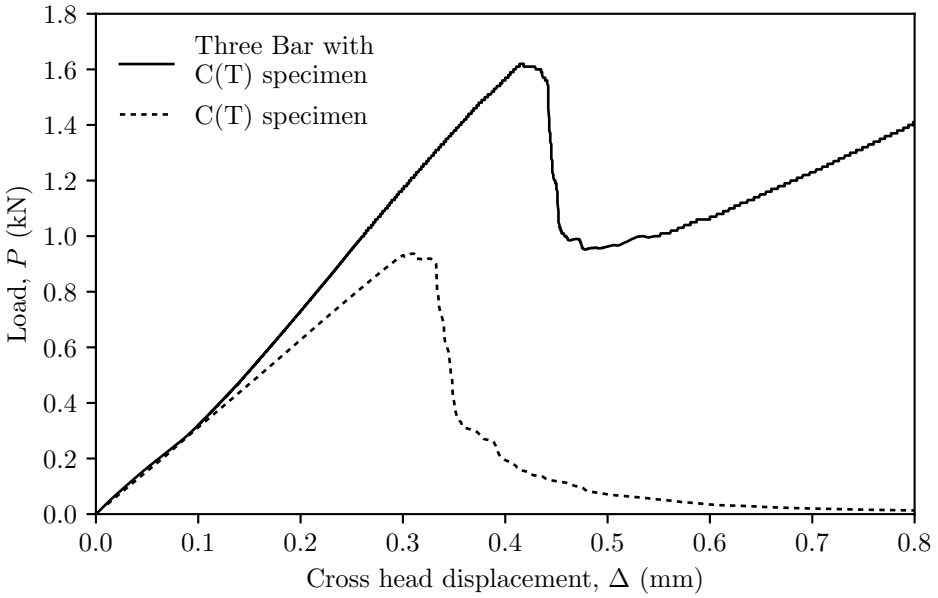

Figure 4.20: Load-Displacement graph comparison between the three bar structure with a compact tension C(T) specimen and a single compact tension C(T) specimen.

fracture process between the calibrated three bar and the single specimen can be found in Figure 4.21.

In the same figure, the difference in peak loads between three bar and single specimen is substituted from the three bar and plotted separately. Although the proportionality of the shared load on the specimen will change throughout the loading, before the apparent fracture and after the specimen "preload" this can be considered negligible. Essentially, by assuming the specimens will behave in the same manner pre apparent fracture, we are able to overlay and compare their fracture behaviour.

4.4 Discussion

4.4.1 Series experiment, uniaxial, biaxial

Stability and base structure

As can be seen from Figure 4.4 to 4.10 as well as Tables 4.1 and 4.2 the stiffness of the base structure had no real effect on the post-peak response of the uniaxial and biaxial specimens. Most of the specimens failed at peak load with no signs

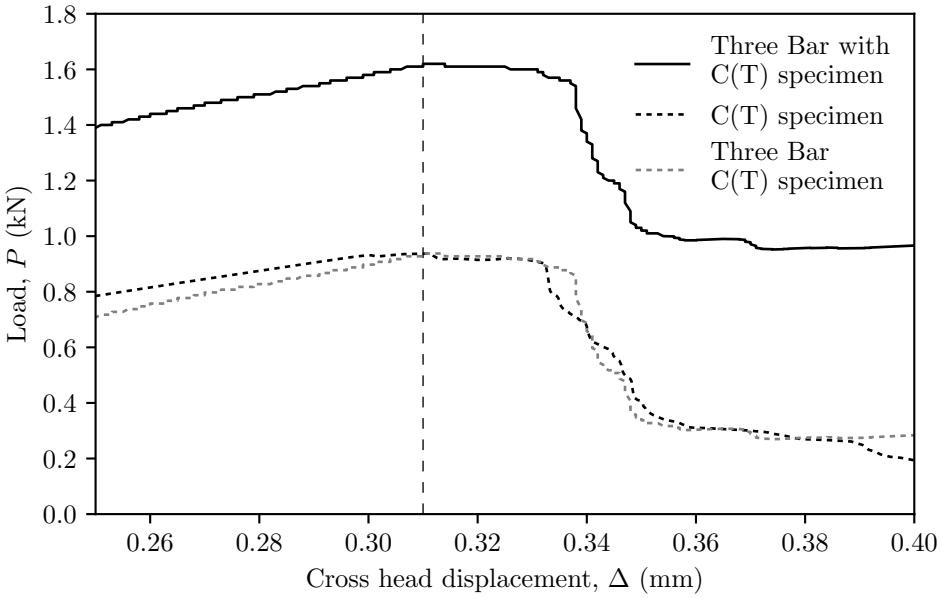

Figure 4.21: Load-Displacement graph comparison between the three bar structure with a C(T) specimen and a single C(T) specimen. Displacement for the three bar structure calibrated on the total displacement at maximum load for the single C(T) specimen. Load for the three bar C(T) specimen calibrated on the maximum load of the single specimen.

of post-peak softening. The only post-peak responses, even minimal, can be seen in the aluminium fixture for the biaxial specimens in Figure 4.9, with one of the two cases being discarded due to misalignment issues. The only effect of the base structure, inconclusive at best, is the area under the graph or the energy accumulated by specimen and base. As expected, for the case of a series structure, the additional energy absorbed by the more compliant spring/base comes from supplementary displacement. Displacement for a given fracture load on the specimen is expected to increase with the increase in spring/base compliance as, when in series, the compliance of the system is the sum of spring and specimen compliance.

Micro-events pre-peak load in the biaxial and uniaxial specimens have been documented through acoustic emission by Liu *et al.* [107]. The lack of a stable post-peak response could be due to the formation of a shallow or not concentrated fracture process zone, not capable of dissipating the accumulated elastic strain energy in a stable manner. As the specimens were plain without notches or pre-cracks, a deep fracture process zone might be difficult to form, always dependent on the geometry of the specimen.

Sub-critical growth of cracks, typical to the stress concentrating defects of the microstructure, was observed by digital image correlation in studies by Mostafavi *et al.* [105, 119] as well as Li *et al.* [120]. The depths of these cracks were calculated, based on their crack mouth opening compliance, to be of about 0.5 to 0.7 mm. The dissipation mechanisms available, essentially microcracking as there was no apparent crack depth to be bridged, could not overcome the elastic strain release rate and produce a more stable fracture, even for the steel base, underlining the initial defect size as an important stability parameter to be considered.

In their report Novovic and Bowen [106] expand on their attempts to arrest crack growth. While at a rate of $0.5\,\mathrm{mm\,min^{-1}}$, the tests were interrupted after the maximum load plateau. Although the authors do not offer more details on the arrest of crack growth or their definition of the plateau, they report success in their method for some of the specimens.

The areas under the curve, calculated in Tables 4.1 and 4.2 show an inconclusive trend. Theoretically, higher energy on the structure is provided for more compliant bases. This is shown as the PMMA structure accumulates the most energy in uniaxial and biaxial. Surprisingly, the energy on the steel structure was greater than that of aluminium in the uniaxial experiment.

As the specimens failed in an unstable manner, comparison of the total energy values would not provide insight into the work to fracture. For the load displacement to provide meaningful results, external work needs to supplement the stored elastic energy, which cannot be assumed in this case. Based on the above, the objective of quantifying stability in a series structure cannot be concluded.

Flexural strength

Contrary to the previous study by Mostafavi *et al.* [105], the results as seen in Figure 4.15 show no clear difference in the flexural strengths between the uniaxial and biaxial specimens. The results, addressing a secondary experimental objective, show a mean stress of $22.7 \pm 0.9\,\mathrm{MPa}$ for the uniaxial and $23.0 \pm 1.1\,\mathrm{MPa}$ ($1.1\,\mathrm{MPa}$) for the biaxial. The Weibull stress was found for uniaxial $\sigma_w = 23.2\,\mathrm{MPa}$ with a modulus of $m = 23.29$ and for equibiaxial $\sigma_w = 23.6\,\mathrm{MPa}$ with a modulus of $m = 22.86$ compared to moduli of 25.27 and 25.36 found by Mostafavi. Results also differ compared to Novovic and

Bowen [106] where equibiaxial strength was calculated to be greater by 16 % compared to uniaxial (28.59 MPa to 24.75 MPa). Interestingly in Novovic and Bowen's study, equibiaxial strength showed no sensitivity to specimen thickness for smaller diameter specimens (120 mm), although, on the contrary, 5 mm thick biaxial specimens ($D = 350$ mm) showed 40 % increase in strength compared to ones of 10 mm, presumably as explained by the authors due to large deflections not accounted for by plate theory.

Li *et al.* [120] in another biaxial ring-on-ring experiment, concluded on an dependence of strength to crack depth and by extension initial defect size. Even though, according to Li, deeper pre-existing flaws tend to produce greater subcritical crack growth, the opposite is true when considering strength. This critical defect dependence in a fully formed zone of microcracking introduces a geometry factor. This puts the specimens in an intermediate state concerning the applicability of Bažant's law as seen in the literature review, where notches or preexisting macroscopic cracks are required, and Weibull's distribution applicability, when compared with different sizes.

Bažant in his later work proposed a categorisation of size effects, naming the above case as Type 1 [121], where material inhomogeneity, expressed as randomness, can influence the mean size effect significantly. It was also found that the flexural strength is inversely proportional to the specimen depth and proportional to the thickness of the boundary layer, validated through Monte Carlo simulations [122]. The equivalent to Figure 2.10 asymptote was determined. For structures much larger than the boundary layer the probabilistic model must reduce to a Weibull distribution [123], whereas for smaller structure sizes it approaches a Gaussian distribution [121].

Fracture paths

The fracture paths are shown in Figure 4.7 and 4.11. All of the uniaxial specimens showed a 90° fracture path passing through the centre of the specimen, as can be seen from the opposite side of the load bearing ball punch. The biaxial specimens could be compared to the paths in the biaxial specimens shown the study by Liu *et al.* [107], where similarities come from the 1 : 1 condition. Ten out of the twelve specimens followed the 1 : 1 condition crack path, documented also by Liu *et al.* [107] in her work. Although even in the 1 : 0 a crack were expected to initiate in the central area, Liu's study shows

otherwise. For this condition (uniaxial), Liu's cruciform showed fracture across the width of one the arms, basically initiating from the corner of the cruciform and following a 90° path towards the other corner, rather than initiating at the centre, which according to Sato *et al.* [111] would point to the area of maximum principal stress. This was the basis behind the change of the corner radius from 10 mm to 25 mm, based on FE calculations, as explained in specimen design. Specimens with variable corner radius, coupled with a method to validate crack initiation locations along with the study of crack paths could provide a method to determine Poisson's ratio.

Two of the biaxial tests, the only ones that showed a post-peak response, had a crack path that branched in the central area, seen in Figure 4.11b. Branching is a minor energy dissipator compared to other mechanisms over shorter branching paths [47]. This branching may be the cause of the response after failure, although it cannot be considered as typical quasi-brittle behaviour, as it is exhibited well below peak load, an equivalent to two consecutive unstable fractures, one after the other, rather than a state of quasi-stability. This response signifies the additional deflection upon the specimen with the growth of another crack branch as the main path grows. The additional energy provided during this post-peak response was used to load both cracks in over 30 sec of displacement at the rate of $0.04\,\mathrm{mm\,min^{-1}}$. In preliminary tests (1 : 1 and 6 : 7) by the author done besides Liu's work, the same branching fracture path was exhibited for the same post-peak response.

Elastic modulus

Although concentrated to the area of maximum principal strain, the strain gauges could offer insight into the softening (non-linear Load-Displacement due to microcracking and FPZ formation) of graphite under uniaxial and biaxial loads. As can be seen in Figure 4.16 and 4.17 the elastic modulus shows a decrease with increase in strain, as measured by the strain gauges (9.5 to 6.5 GPa). Also, these figures show that the taken value of 10 GPa for the FE model was relatively accurate. The above is unrelated to the FE assumptions as it was shown that the stress to load ratio used in the calculation was non-sensitive to the value of the modulus.

Ideally, to fully examine the softening response of this grade of graphite, cyclic loading, with increasing loads (tension or compression) and measuring of

the unloading cycles is suggested, as seen in [103]. The incrementally increasing cyclic loads offer a better understanding on damage accumulation with clear thresholds of softening and the formation of the FPZ. Marrow *et al.* [103] in contrast to the tensile experiments in their study, found the elastic modulus in typical four-point bending (tensile surface) not to be affected by loading (less than 10 % softening). On the contrary, Mostafavi *et al.* [113] in similar configuration used in this study, showed a decrease of measured modulus from 9.7 to 7.8 GPa with measurable inelastic strain present. This validates the presence of an intercept in the rolling linear regression performed.

4.4.2 Three bar experiment, parallel

Behaviour

As can be seen from Figure 4.21, both specimens perform in a similar manner, not concluding the objective of quantifying stability in the three bar parallel structure. It was expected for the specimen in the three bar structure to fail in a more unstable manner as can be seen in Chapter 3, as the ratio of outer structure to specimen compliance was calculated theoretically to about 1.5.

Slopes and stiffness

The Towers solution [116] (seen also in ASTM-1820 [61]) for the specimen stiffness was used and found to be about 6.5 $\mathrm{kN\,mm^{-1}}$. This solution provides the load line compliance based on specimen geometry, crack to width ratio (α) and elastic modulus. The specimen type used (ASTM-399 [94] C(T)) cannot support a clip gauge on the load line, thus making the use of one at the crack mouth a necessity when evaluating compliance and by extension crack length.

As these preliminary tests were mostly focused on fracture behaviour and thus post-peak load, for ease of use on the testing machine without a data logger, no clip gauges were used. Based on the slopes of Figure 4.20, the specimen itself for both cases, has a slope of about 3.15 $\mathrm{kN\,mm^{-1}}$. After the fracture of the specimen most of the load is on the outer bars which together show a slope of 1.70 $\mathrm{kN\,mm^{-1}}$. The vast difference between theoretical load line specimen compliance and slope in the load-displacement graph (cross head displacement) may be due to elastic contributions in series to the specimen and outer bars (loading pins, machine, etc.). The machine (Shimadzu AGS-X) has

a frame rigidity of $42\,\mathrm{kN\,mm^{-1}}$, as stated by the manufacturer, which would lower the specimen's slope response to about $5.7\,\mathrm{kN\,mm^{-1}}$.

Calculating the slope of a load-displacement graph, even with the most accurate data can be quite sensitive based on the algorithm used. Several methods can be used to describe what can be considered the best fit of a line. One of the most common, also used in this work, is the least squares method. The above is basically described as minimising the sum of the vertical distances from the data point to the fitted line if x is chosen as our independent variable. If y is chosen as the independent variable, the horizontal distances are minimised. This can have an effect in the stiffness values given from our linear fit and thus the independent variable should be chosen as the one driven by the testing machine.

Load, displacement control

Electromechanical machines, as the one used in this experiment are driven by a stepping motor, which can control the angular position of the rotor directly, without a closed feedback loop. Through a ball screw the controlled rotation of the motor is translated to linear motion acting on the specimen. Thus, the machine naturally operates in pure displacement control. Operating in pure load control can pose a challenge as the machine uses a closed feedback loop between load cell and step motor. This might have been the limiting factor to the three bar structure load control test.

The above challenge can be seen in Figure 4.20 where the three bar structure is under load control of $10\,\mathrm{N\,min^{-1}}$. Before the peak load, when reviewed in the raw data with time, a perfect rate was kept. After the peak load and as the specimen is fracturing (increasing compliance), the motor is simply delivering displacement (slowly) rather than keeping a dead load, an intermediate state rather than the pure load control required. This may be attributed to the limitations of the stepper motor, a safety function prohibiting fast cross head movement, or the sampling in the closed feedback loop.

Corrections on method

Based on the above problems some future recommendations can be added, even though the three bar initial tests were not promising in altering the fracture behaviour of the C(T) specimen. A machine capable of pure load control with

increasing load would be ideal. Otherwise, the same test can be run in series with a normal testing machine in displacement control with the spring in series as can be seen from the uniaxial and biaxial experiments. The bar or spring supporting the specimen has to be equal or of lower stiffness for any change to appear, especially for the case of inherently stable C(T) specimen as can be seen in the analysis of Chapter 3. Moreover, a clip gauge (load line or crack mouth) needs to be added to measure the elastic strain energy of the specimen. More of the experimental preparations needed for a conventional fracture test on a C(T) specimen will be presented in the next chapter.

Chapter 5

Fracture size effect

Although energy release rate or crack driving force G and the elastic energy follow-up that might come from the rest of the structure or a different specimen might lead to instabilities, the most important factor would be fracture resistance R. As can be seen in the literature review of Chapter 2, a significant amount of work has been done in developing methods examining and understanding the intricacies behind fracture resistance of graphite.

The work though is mostly focused on specific sized specimens without any consideration on the matters of size; focus more prevalent in concrete by the works of Bažant. Concrete as well as graphite are considered to be in a similar category of materials, exhibiting post failure gradual softening, which can be described as a "graceful failure" [103]. Due to the non-scalability of the mechanisms contributing to this behaviour, concrete and graphite experience a size effect, a mismatch in scaling between these mechanisms and the size of the specimen or structure. Even though concrete size effect might be more prevalent due to much larger structures, there has been interest in quantifying the effect in graphite. As seen in the review of the bibliography, fine grain isotropic graphite was found to exhibit a distinct size effect even in the range of standard laboratory specimens [75, 85].

The aim of this chapter is to examine the effects of size in all matters of fracture properties and specifically resistance. The discrepancies between apparent fracture toughness K_{Q}, with ties to the rising behaviour of the K_{R} and R-curves, under the prism of size will be examined. Also, the calculation of the resistance curves will provide important insight into the general fracture behaviour of graphite irrespective of size. Moreover, uncertainties introduced

in previous tests, as seen in Chapter 2, will be addressed.

Firstly, the experimental details will be discussed. These include the chosen specimen and sizes, the fixtures, the experimental preparations and procedure. Following, the experimental data will be presented, everything needed for the subsequent analysis. Before the discussion, analysis of the experimental data will provide the needed information for the conclusions to be drawn.

5.1 Experimental Details

The aim of this experiment is to evaluate the fracture resistance of graphite, on varying crack lengths and further expand the understanding of the mechanisms responsible for graphite's fracture behaviour. The above needs to be done in different sized, ideally similar geometry specimens, to examine whether a size effect is present over the size scale, as well as quantify it.

For the fracture resistance, a valid method of calculating the elastic strain energy on the specimen needs to be understood. The varying crack lengths needed, require, as accurate as can be, methods of measuring directly or calculating the crack lengths, without adding many complexities. Controlling fracture as well as quantification of size effects, require an inherently stable specimen able to form and propagate a large crack in a quasi-stable manner.

The experimental details presented below aim to address these considerations.

5.1.1 Design

Specimens

Compact tension (C(T)) specimens were used in this test programme. The specimen allows for a crack to grow in a stable manner and to greater lengths compared to other standard geometries [61, 94]. Although these standards apply to metallic materials, the geometric functions are generally applicable. The design of the specimens followed the simpler E399 which calls for knife edges on the crack mouth rather than the load line seen in the C(T) specimen of E1820, and can be seen in Figure 5.1. This is due to the limiting factor of size and clip gauge length, as will be explained below.

Three specimen sizes were chosen. The traditional 1T-C(T) (25 mm thick)

Table 5.1: C(T) specimen dimensions.

Specimen Size	1/2T	1T	2T
Thickness, B (mm)	12.5	25	50
Width, W (mm)	25	50	100
Crack Length, a (mm)	8.75	17.5	35
a/W, α	0.35	0.35	0.35

was selected as a base, with one perfectly scaled in half (1/2T) and one double in size (2T), with the specific dimensions seen in Table 5.1. The initial crack length for all sizes was chosen to be 35 % of the width ($a/W = \alpha = 0.35$), which would provide enough uncracked ligament for resistance measurements without compromising stability and the validity of the compliance and stress intensity geometric functions. Although the standard applies to metallic materials, size requirement is defined as $W - a \geq 2.5\,(K_{\mathrm{Ic}}/\sigma_{YS})^2$. The smaller chosen size is valid for IM1-24 graphite, if as σ_{YS} its tensile strength is used.

The specimens were made from Gilsocarbon graphite (IM1-24) extracted from a stock block provided by EDF Energy. Extraction from the block as well as machining of the specimens was done by Erodex Ltd with dimensions specified from ASTM-E399 [94]. The straight through notch tip radius produced by Erodex for all sizes was approximately 0.05 mm as measured by the Axio Imager 2 Research Microscope (Zeiss). The notch type was chosen to avoid the problems on the chevron notches when monitoring and measuring the crack ligament area, as experienced by Sakai [42] and Hodkins [5].

Burchell, as part of his PhD thesis [33] studied the notch sensitivity on sleeve graphite and found a difference of less than 3 % in the stress intensity factor between notches with radius of 0.005 mm and 0.05 mm. Brocklehurst [40], for IM1-24, studying the stress concentration, found differences of about 7 % between notches of 0.02 mm and 0.12 mm. Brocklehurst also argued that on very small radii, the notch tip gets blunter as damage accumulates, well before the peak load. Both of their studies were done on single edge notched beams, in 3-point bending. Based on the above, the notch radius was deemed satisfactory.

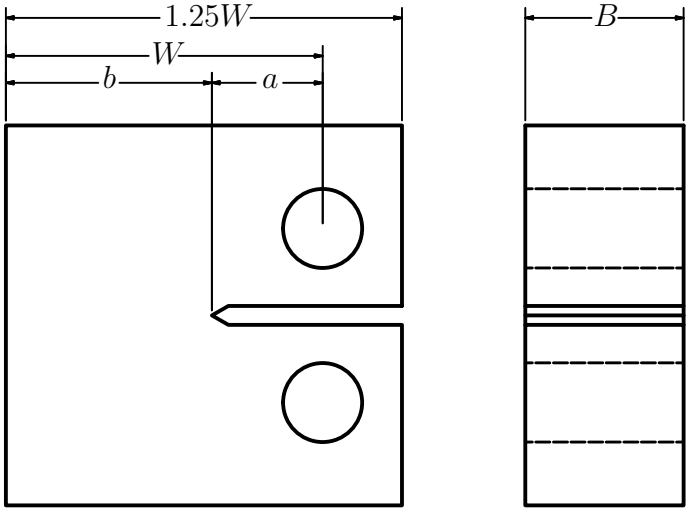

Figure 5.1: ASTM Standard E399 compact tension specimen geometry, to scale, showing important geometrical dimensions: crack length, a; width, W; uncracked ligament length, $b = W - a$; and thickness B. Specific dimensions presented in Table 5.1.

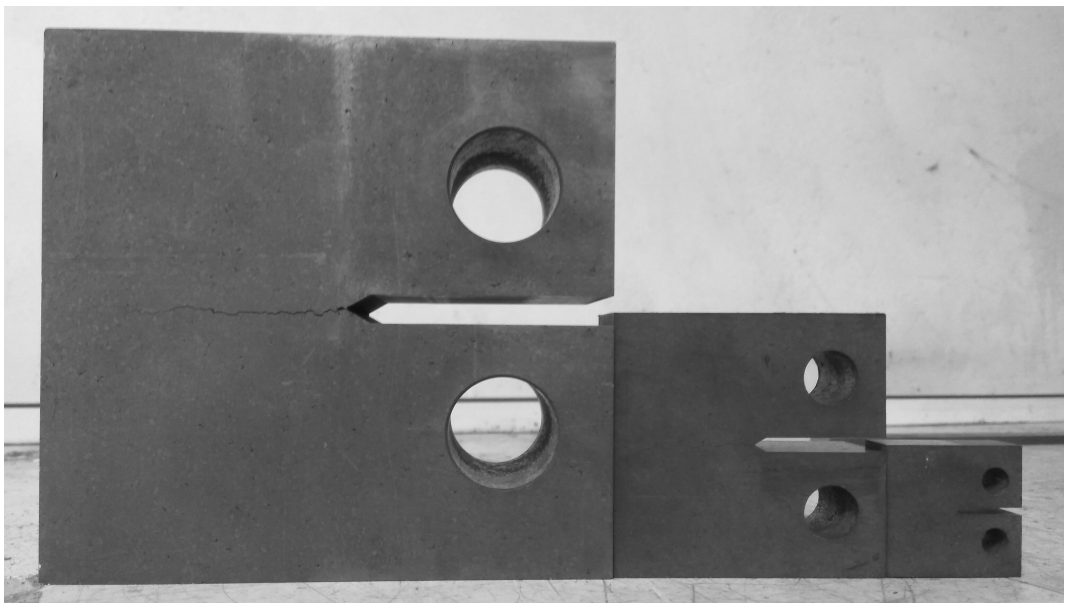

Figure 5.2: Different sized Gilsocarbon graphite compact C(T) specimens. Largest specimen 125 mm in total width.

Clevises

The clevises designed for the experiment followed the general guidelines of ASTM-E399 [94]. A single loading rod between specimens sizes was used, thus the diameter on the bottom of the clevises was the same, with a loading rod thread of M36. Rods and clevises were made from EN24T steel.

The corners on the clevises for the smaller specimens ($B = 12.5\,\text{mm}$) were removed, per suggestion of the E399 standard, to easily accommodate the clip gauge and improve visibility of the specimen side for the optical measurements.

5.1.2 Setup and procedure

Crack mouth opening displacement

The measurement of either the load line or crack mouth opening displacement is essential for the measurements of stiffness. Cross head displacement was proved to be inaccurate in the previous chapter, even for much stiffer loading structures compared to the specimen. Two standards for compact tension specimens (E399, E1820) and their solutions were examined.

An Instron 10/4 clip gauge was used, with gauge length of 10 mm and travel of 4 mm. The clip gauge beams have a width of 10 mm, small enough to be inserted between the clevises of the smaller specimens ($B = 12.5\,\text{mm}$). The smaller specimens could not accommodate a clip gauge at the load line as the edge of the holes for the loading pins are closer than the gauge length of the clip gauge that was available. Thus, based on E399, knife edges on the front face of the specimens were used, with extra caution to centre the gauge to avoid issues caused by eccentricity.

Steel knife edges were manufactured, again according to the standard. These knife edges were mounted on M2.5 threaded holes that were tapped across the width of the specimens face on the exact location to ensure the gauge length of 10 mm. For the 1/2T specimen, threads could not be added due to geometry and material limitations. The knife edges for the smaller specimens were glued to the pretreated area with a slow set glue. The area was thoroughly dusted and rubbed with an alcohol solution. Initial tests on the glue bond were performed and readings on the clip gauge were recorded for 3 hour period. These tests showed no deviation (less than 0.5 %), considering the background noise, and the gluing and knife edges were deemed acceptable.

The clip gauge was calibrated based on the method seen in the PhD thesis of Van Gelderen [124], although only for room temperature (20 °C). Linearity of the clip gauge was tested over its 4 mm travel using a tabletop barrel micrometer. The linear profile was deemed satisfactory.

Camera

Due to the uncertainty on the optimal crack measuring method, as seen by the plethora of techniques used in section 2.3, the additional use of an optical method seemed crucial. A Pixelink PL-B778G camera was used, mounted on a tripod, with a macro lens, ideal for high quality pictures in close proximity to the specimen (3000 x 1776 pixels). The lens was specifically chosen to be able to focus on the whole side face of the largest specimens, in order to capture the full length of the crack. An extra light source with a diffuser was used to increase the clarity of the obtained images and thus the contrast between face and crack.

Even with the above setup, cracks were difficult to spot on the first specimen. To increase contrast, the uncracked ligament area of the specimens was sprayed with a coat of white paint. A light coat was used as for the paint to not excessively permeate through the outer pores of the specimens.

The camera was connected from its GigE interface through a Gigabit ethernet cable to a network card in a mobile tabletop workstation. The workstation was running a LabVIEW code though which the camera was operated, providing real time crack monitoring through the screen.

Setup

An Instron MJ6272 (25 kN) hydraulic testing system was used with an Instron 8800MJ testing controller calibrated to standard [109] by Instron Laboratory. The maximum load of 25 kN was well beyond the expected peak load of the 2T specimens of about 4 kN. The clip gauge was connected to the Instron 8800MJ and its values were passed to the Trapezium recording software. Time, load and cross head displacement values where also passed and recorded.

Time and load values were also passed to the LabVIEW camera program setup. The camera was connected to a different computer setup and the voltage values passed (time, load) had to be calibrated through both. This enabled

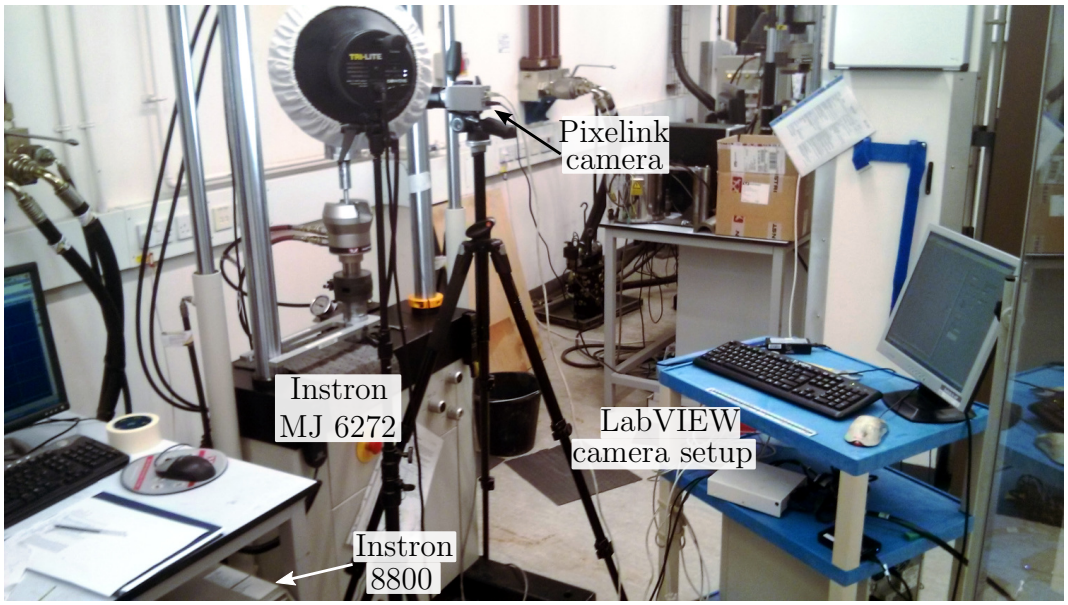

Figure 5.3: Overview of the experimental setup.

the images to be taken with the corresponding load and time in the file name for ease of use in the analysis.

An overview of the setup can be seen in Figure 5.3 with a close up on the loaded specimen in Figure 5.4.

Procedure

The procedure that had to be followed for the determination of the R-curve should be close to the one followed by Sakai *et al.* [42]. A cyclic load is to be used with an unload-reload procedure repeated after an incremental crack extension Δa. This load-unload procedure is to be repeated until the specimen fails, with usually 8 to 15 repetitions completed with each specimen. Based on the above, each graphite specimen would provide many data points, as a function of crack length, for the fracture parameters.

A loading pattern was programmed in Trapezium, the software used to control the machine. This software allows for several loading blocks as well as looping between them. Thus, loops for load, hold and unload were written, to be repeated indefinitely with the user able to exit the loop at any point, namely the final failure of the specimen. The iteration of the loops was also controlled by the author/user as in preliminary tests the software triggering events (load drop etc.) seemed unsatisfactory and crude. As the load after

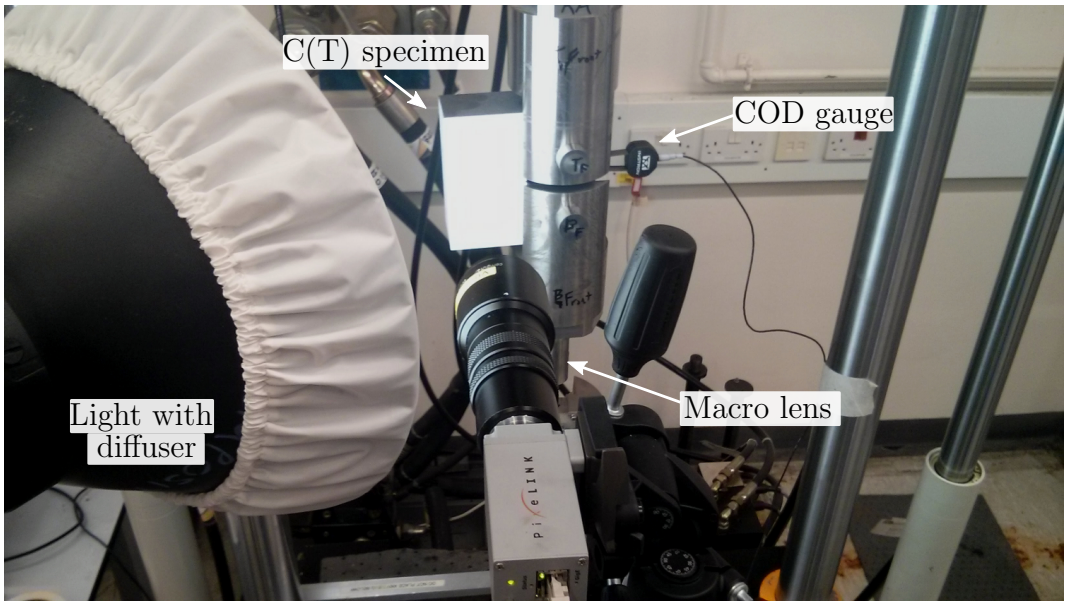

Figure 5.4: Close up of the experimental setup.

the crack extension stabilised, the hold was triggered and then the unload to about 5 % of the overall peak load. The partial unloading, as explained in subsection 2.3.6 was done to avoid crushing the bridging particles more than necessary.

The hold was put in place to ensure an image was taken at the moment where the crack measurement was the most important. Although images were taken throughout the procedure, the LabVIEW code enabled on the fly changes in the capturing frequency, up to the capabilities of the camera and lens. The above meant that as each peak load was approaching the user could change the frequency to capture more photos of the loading and stable fracture. Due to buffer as well as size limitations, fast capture (1 image per second) was only enabled very close to the cycle peak loads based on the previous cycle.

Displacement rate was set differently for each specimen size, based on Li's study [65], although the cross head displacement instead of the CMOD was chosen. The cross head displacement meant that there is no variability in the strain rate based on the displacements of the gauge, resulting in strange loops when the closed feedback loop of machine and CMOD has to be recalibrated. As the machine is hydraulically operated, stable displacement can be achieved. Displacements were set at $0.01\,\mathrm{mm\,min^{-1}}$, $0.02\,\mathrm{mm\,min^{-1}}$ and $0.04\,\mathrm{mm\,min^{-1}}$ for 1/2T, 1T and 2T respectively. A faster loading and unloading cycle was put

in place in order to minimise the time in the linear cyclic areas. These loading rates were twice the normal loading rates, low enough for the strain rates not to affect the behaviour of the specimen, as seen in Burchell's work [33] where he showed negligible differences between rates of $0.5\,\mathrm{mm\,min^{-1}}$, $1\,\mathrm{mm\,min^{-1}}$. The faster loading blocks were only in the linear areas of the loading and unloading blocks and far from peak or lower limit loads.

Camera rate was manually set from 0.05 to 1 Hz based on proximity to peak load or change from unload to load, producing 600 to 1100 photographs per tested specimen.

In total, 10 specimens from each size were tested, 2 of each size on a single load to failure with the same rate as the rest in the cyclic loading explained above. Specimens are named with the size first followed by the specimen number, example 1/2T5 being specimen number 5 from the 1/2T size. The first two specimens from all sizes are the ones tested in a single load to failure (1/2T1, 1/2T2, 1T1, 1T2, 2T1, 2T2).

5.2 Results

As stated in the procedure, 10 specimen of each size were tested. The initial two for each size were single loads to failure in order to have a general overview of the cracking process. Photographs were taken throughout the loading and cracking.

5.2.1 Load CMOD

The load unload process can be seen in the load-crack mouth opening displacement Figures 5.5, 5.6, 5.7. One of the two single load loadings is plotted against a cyclically loaded specimen for each size.

The unload threshold was about 20 N for the 1/2T, 50 N for the 1T and 200 N for the 2T. However, as this was manually controlled, there were discrepancies in the unload threshold between specimens and cycles, which will be addressed later in the analysis. As can be seen from Figure 5.5 14 cycles were performed for specimen 1/2T4, 13 for specimen 1T4 (Figure 5.6) and 17 for specimen 2T6 (Figure 5.7).

Lastly, Figures 5.8, 5.9, 5.10 show the response of all specimens of each size accordingly. The cycles have been taken out as these figures serve illustration

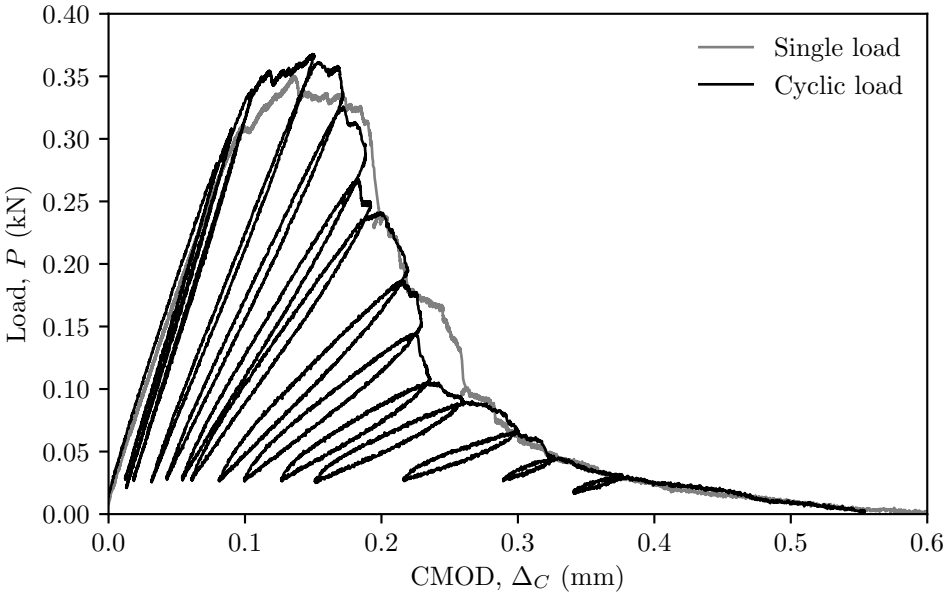

Figure 5.5: Load-crack mouth opening displacement, under displacement control, 1/2T size. Specimen 1/2T1 (single load) and specimen 1/2T4 (cyclic load), 14 cycles.

purposes.

5.2.2 Discrepancies

Specimen 1/2T2, the smallest of the three sizes, loaded to a single load to failure exhibited a curious case as can be seen in Figure 5.11. Cracking did not initiate from the notch tip or even the notched surface. It did initiate however from pores in a close proximity to the notch and thus the higher stressed area. As can be seen in the figure, with the addition of photographs taken at specific times, the cracks initiated through the pores at around 250 N, sensitive to the frequency of the camera and loading rate. In the initial photograph taken, the crack has not extended to the notch or the notched side, however at the peak load of 344 N or shortly prior, the crack has been extended backwards and forwards, though not through the notch tip, by less than 0.5 mm. Due to the above, 1/2T2 will be excluded from the subsequent analysis (K_{Q}, γ_{wof} calculations).

Specimen 1/2T8, also exhibited an abnormal crack initiation location as can be seen in Figure 5.12. A very thin crack was present below the area of the notch tip. This crack opened by even the slightest load (30 N), as can be seen

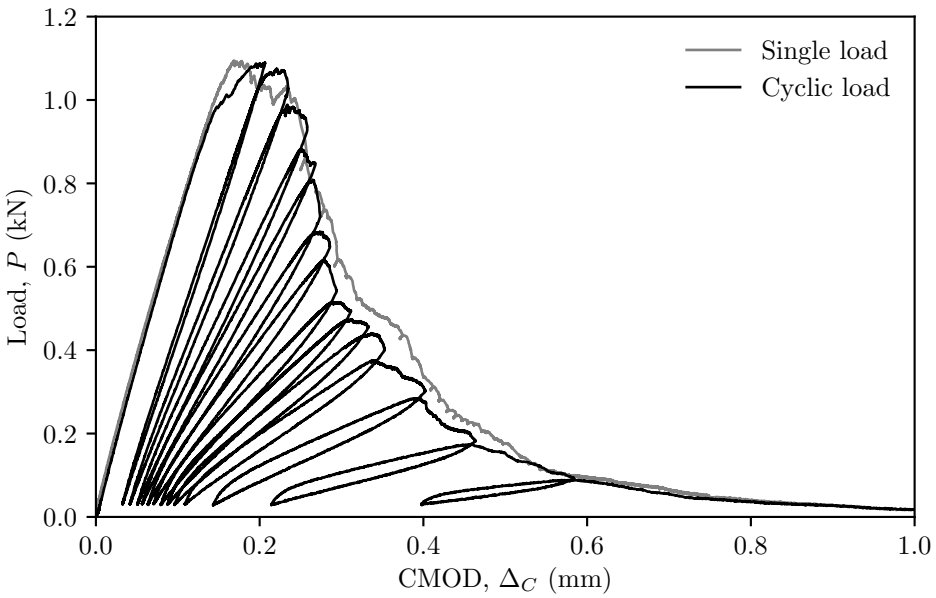

Figure 5.6: Load-crack mouth opening displacement, under displacement control, 1T size. Specimen 1T2 (single load) and specimen 1T4 (cyclic load), 13 cycles.

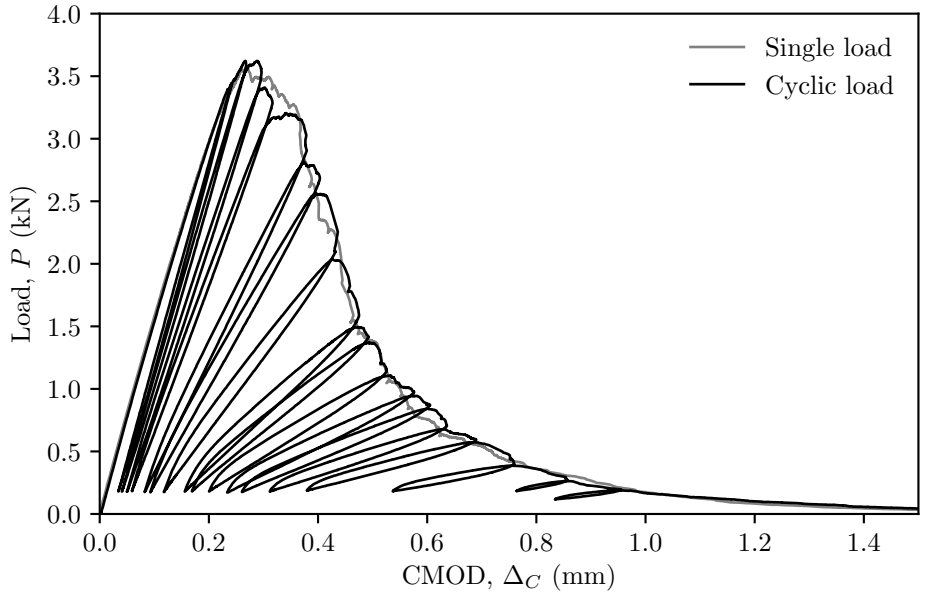

Figure 5.7: Load-crack mouth opening displacement, under displacement control, 2T size. Specimen 2T2 (single load) and specimen 2T6 (cyclic load), 17 cycles.

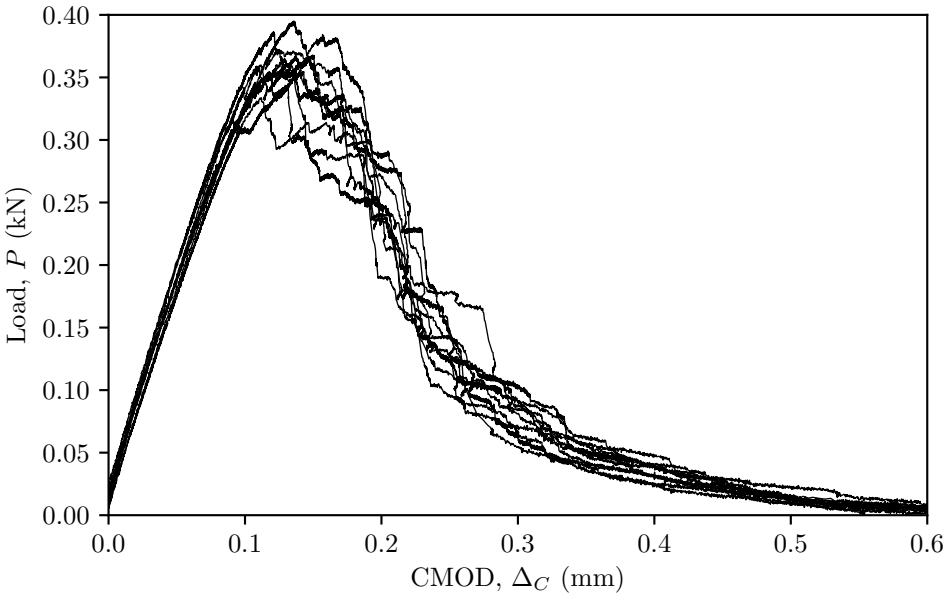

Figure 5.8: Load-crack mouth opening displacement, 1/2T size, all specimens. Cycles on the 8 specimens were removed for illustration purposes.

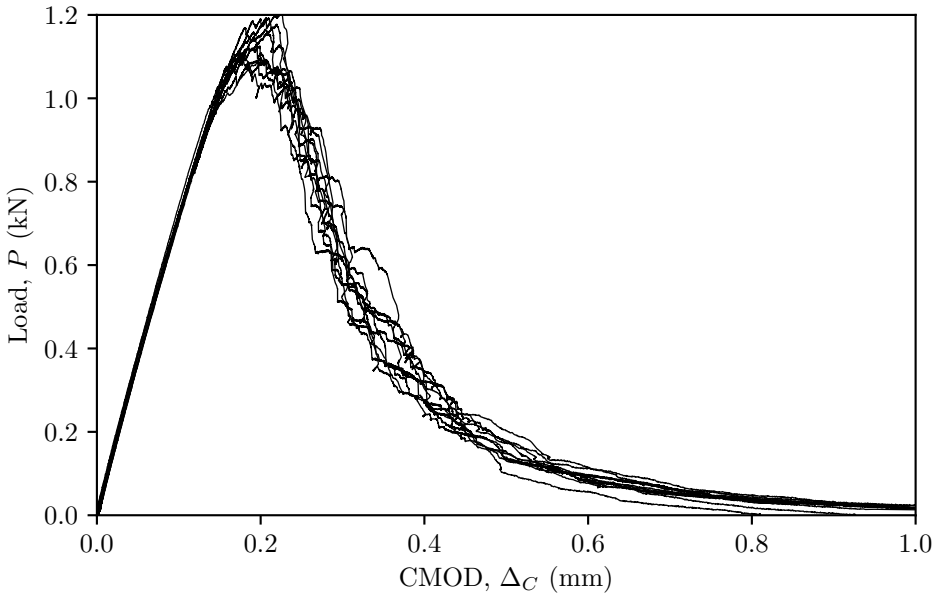

Figure 5.9: Load-crack mouth opening displacement, 1T size, all specimens. Cycles on the 8 specimens were removed for illustration purposes.

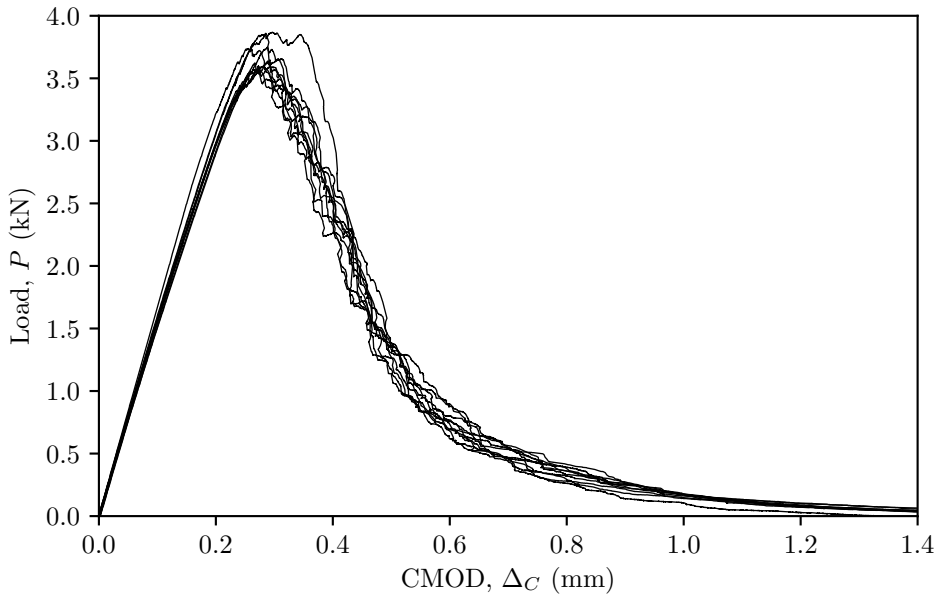

Figure 5.10: Load-crack mouth opening displacement, 2T size, all specimens. Cycles on the 8 specimens were removed for illustration purposes.

in the first photograph of Figure 5.12. The pre-crack exhibited might be due to manufacturing or mishandling during experimental preparation or loading (loading pins etc.). Cracking, after about the initial 2 mm bowed upwards towards the centreline. Due to the above, no measurements corresponding to this specimen will be analysed. Image measuring of crack lengths will be discussed in the following section.

5.3 Analysis

The analysis of the experimental data will be presented below. All of the analysis was done in Python [110] and the functions used will be referenced. Initially the method for the linear regression performed on all cycles will be presented.

5.3.1 Cycle linear regression

As can be seen in Figures 5.13 and 5.14, two types of linear regressions were performed. The first one is on the unloading lines (Figure 5.13) and the other on the reloading (Figure 5.14). The intricacies of the procedure as well as the

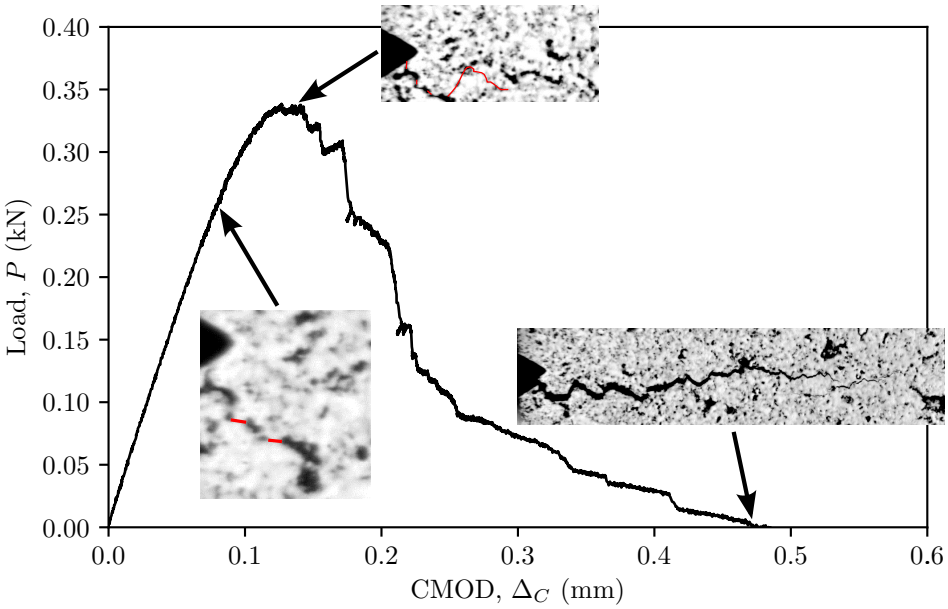

Figure 5.11: Discrepancy of specimen 1/2T2, single load to fracture. Crack initiation through a pore at about 70 % of peak load. Images of crack at various loads, 70 % of peak load, peak load, load at failure. Hair thin cracks displayed with red lines.

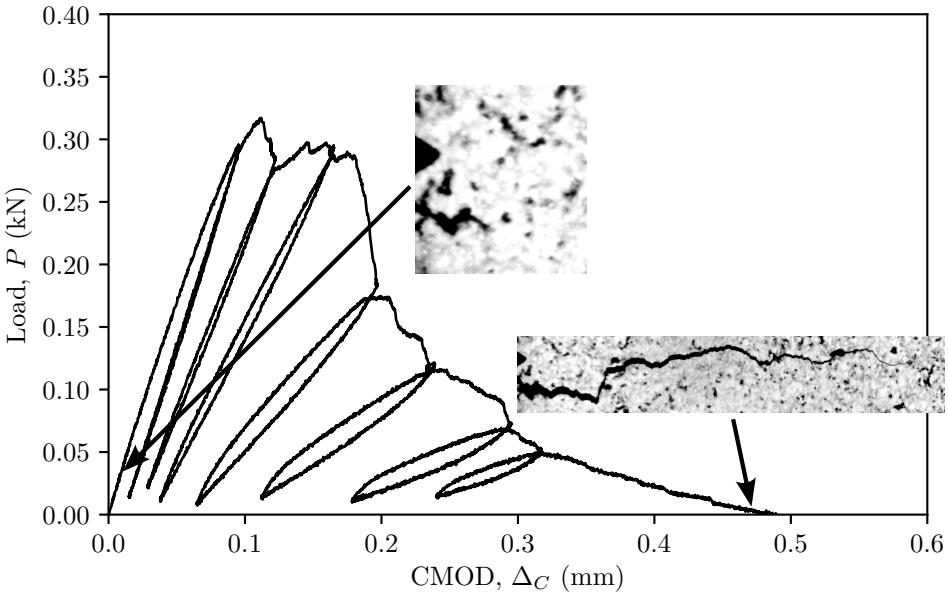

Figure 5.12: Discrepancy of specimen 1/2T8, cyclic loading to fracture. Pre-existing crack, due to manufacturing or mishandling of delicate specimen. Images of crack at various loadings, 10 % of peak load, load at failure.

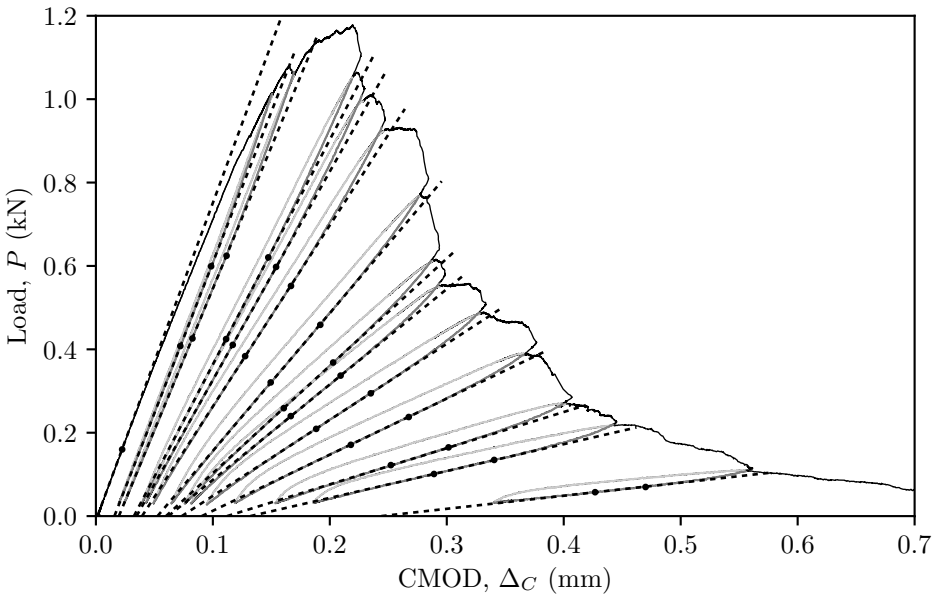

Figure 5.13: Load-crack mouth opening displacement, 1T size. Specimen 1T7, graphical representation of the linear regression performed on the unloading part of the 13 cycles. Black dots represent the chosen windows.

acquired values are presented below, with the interpolation and regression of the cycles presented in Appendix B.

Unload or reload

Figures 5.15 show the cycle slope values and the intercept on the independent variable (CMOD), based on the above method, for each of the specimen sizes. The CMOD intercept was calculated as $-\beta_0/\beta_1$ with β_0 being the intercept and β_1 the slope, both from the linear regression function. From top to bottom the three specimen sizes are presented, 1/2T, 1T, 2T, respectively. Both the reload and unload values from the regressions are presented to aid in the selection of the most appropriate in determining the value of stiffness in the cycle.

During the analysis an additional check for errors in the script was introduced. Based on the assumption that the values of intercept, individually between load and unload, had to be increasing, albeit slowly for the subsequent cycles, a function was introduced. This function, although never triggered, would print the cycle and specimen number for ease of identification.

For consistency in the following analysis, a method between the two had to picked. Although the values on the 1/2T specimens are quite scattered,

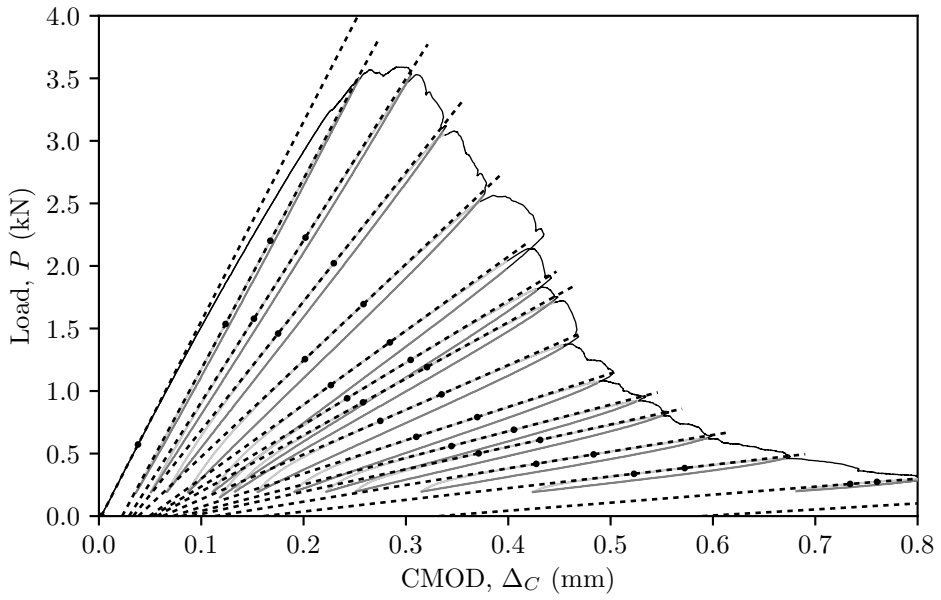

Figure 5.14: Load-crack mouth opening displacement, 2T size. Specimen 2T8, graphical representation of the linear regression performed on the reloading part of the 15 cycles. Black dots represent the chosen windows.

the unloading slopes for the 1T and 2T specimens show less scatter than the reload slopes. Moreover, there is a general consensus that seems to support the use of the unloading line although no reason is provided against the use of the alternatives (reload or combination) [31,79,125]. Due to the above, for the subsequent analysis, the unloading slope will be used, unless directly stated.

5.3.2 Crack length measurements

The methods used throughout the work to determine the crack lengths will be examined below. These methods come either directly from the camera measurements as taken from the pixel counting in the images, the standards' functions used to describe the C(T) specimen or the simpler linear interpolation seen in (2.17) in subsection 2.3.3. Apart from the camera images, the methods presented below require the values of stiffness/compliance as calculated above, albeit with some additional calibrations.

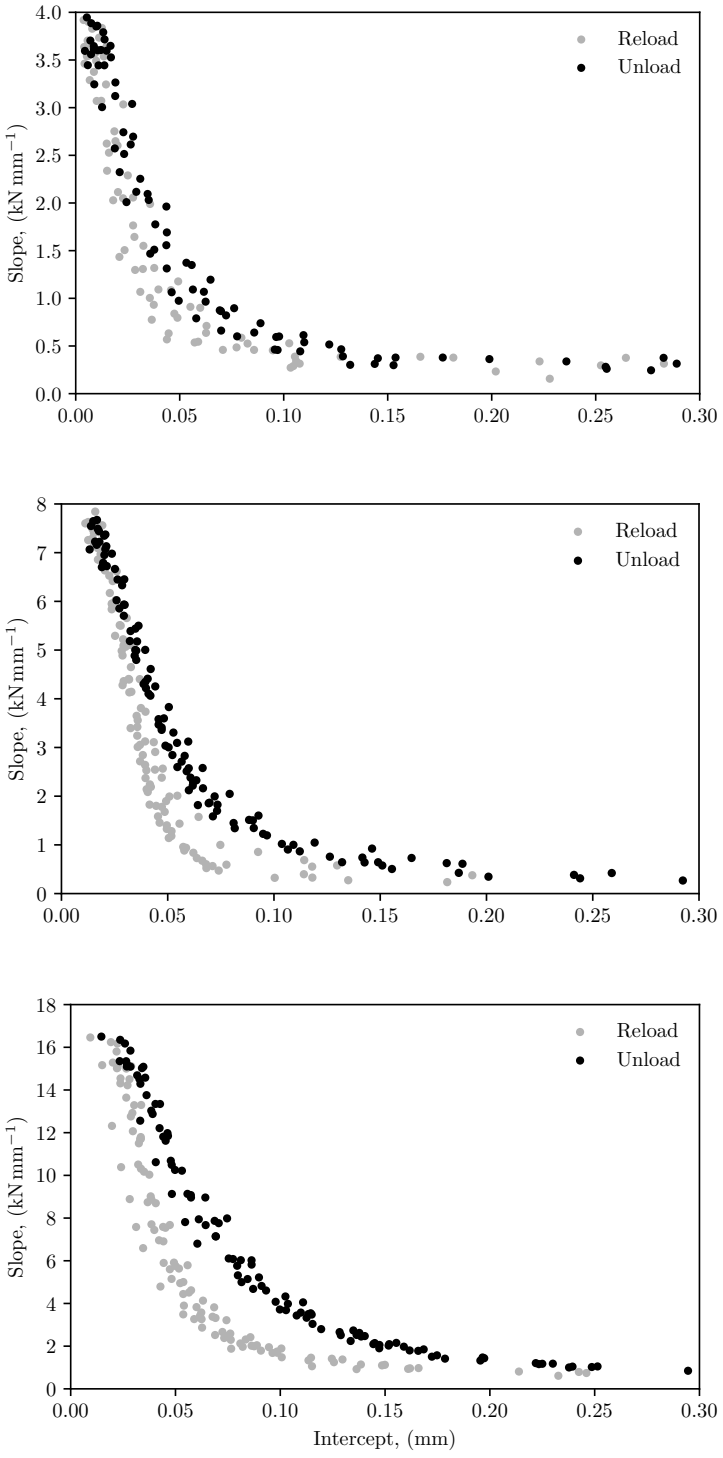

Figure 5.15: Intercepts and slopes as calculated from the regression function, for the three specimen sizes. From top to bottom, 1/2T, 1T, 2T respectively. Reload cycles in grey and unload cycles in black.

E399

The standard's crack mouth opening compliance function using crack length to width ratio a/W is given for the C(T):

$$\frac{V_m}{P} = \frac{1}{E'B} q\left(\frac{a}{W}\right) \tag{5.1}$$

where:

$$q\left(\frac{a}{W}\right) = \frac{19.75\left[0.5 + 1.92\frac{a}{W} + 1.385\left(\frac{a}{W}\right)^2 - 2.919\left(\frac{a}{W}\right)^3 + 1.842\left(\frac{a}{W}\right)^4\right]}{\left(1 - \frac{a}{W}\right)^2} \tag{5.2}$$

The reverse function from E399, using with the measurements of compliance, provides the crack length to width ratio as:

$$\frac{a}{W} = 1 - 4.500U + 13.157U^2 - 172.551U^3 + 879.944U^4 - 1514.671U^5 \tag{5.3}$$

with U being:

$$U = \frac{1}{1 + \sqrt{\frac{E'BV_m}{P}}} \tag{5.4}$$

where E the Young's modulus, $E' = E/(1-\nu^2)$, B the specimen thickness and V_m/P the crack mouth opening compliance with V_m the crack mouth opening displacement and P the applied load.

The above function, as described by the standard, requires measurements of displacement at the location of integral knife edges and is valid within 0.1 % over a crack to width ratio of $0.2 \leq a/W \leq 0.8$. As previously stated, due to specimen size and clip gauge availability, integral knife edges could not have been used and were substituted with attachable knife edges to the faces of the specimens. The values for the displacement and thus the compliance had to be calibrated.

For the calibration, a finite element method was used. Although the problem is geometrical, the several limitations to the movement of the specimen and the problem of the increasing crack length proved complicated for simple trigonometry. The analysis over several crack lengths (0.35 to 0.95) for the different sizes of specimens gave a relationship that could be linearly approximated with the relation $\Delta_c = k\Delta_{\text{int}}$ with $k = -0.0304\alpha + 1.0306$ with Δ_c the experimental crack mouth opening displacement, Δ_{int} the displacement mea-

sure at the integral knife edge locations as described by the standard. This function of crack length would give a difference in displacement of about 0.6 to 2 % over the standard's validity. Alternatively, the E561 standard [126] could be used for this calibration, especially in $0.35 \leq a/W \leq 0.6$ range, with an accuracy of $\pm 0.04\%$.

The compliance correction for a fixed crack length over the specimen rotation, as can be seen in E1820, was negligible for the experimental cyclic ranges of CMOD and will be further touched upon in subsection 5.3.5. Moreover, the differences between specimen sizes were minimal, 0.2 to 0.5 % for 1/2T and 2T and thus a single equation was chosen.

Based on the above functions, with the compliance calibrations, a/W values were calculated for each cycle and specimen size. The initial loading mean $\bar{a_0}/W$ and standard deviations for the different sized specimens were as follows: 1/2T specimen 0.353 ± 0.009, 1T 0.353 ± 0.008 and 2T specimen 0.355 ± 0.006. These values were calculated based on the specimen geometries and material property values of $E = 10\,\text{GPa}$ and $\nu = 0.2$.

The above can be seen in Figure 5.16, where the values from the compliance to crack length function are plotted against those of the inverse function (5.1). As expected, the values are on the dashed line and as can be seen from the figure, the crack lengths at the last cycles, which were very close to full failure ($\alpha > 0.9$), seem underestimated.

Interpolation

Several alternatives of interpolation can be used but all of them are based on the function below:

$$a_n = a_{n-1} + \frac{W - a_{n-1}}{2} \frac{C_n - C_{n-1}}{C_n} \tag{5.5}$$

with $n-1$ being the previous cycle, n being the current one, a the crack length, W the specimen width and C the compliance, either measured at the load line or crack mouth.

As can be seen from the function, it requires an initial crack length in order to interpolate over. One can either use the initial a_0/W as manufactured and measured, which is the same for the optical measurements, or the values given by the E399 function above.

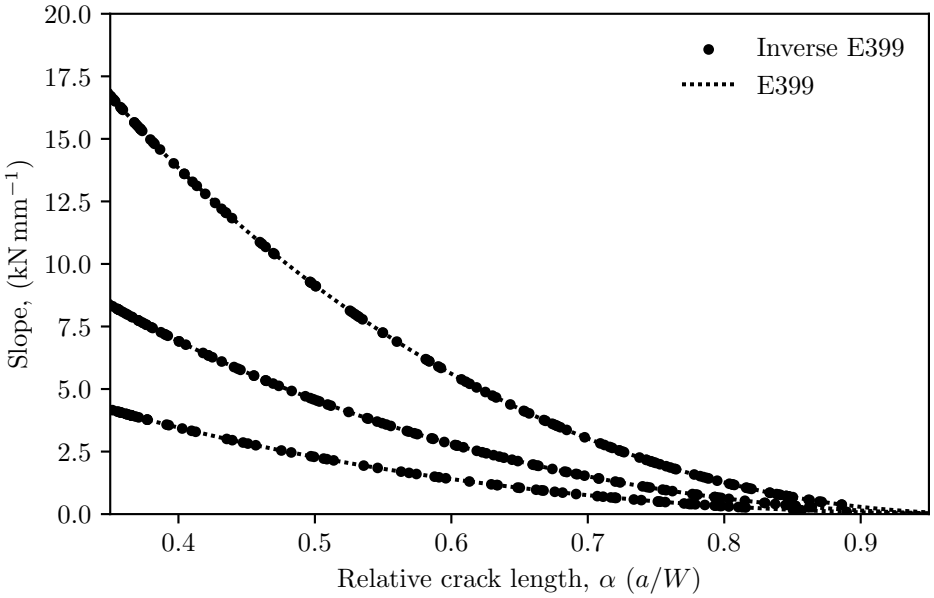

Figure 5.16: Relative crack lengths-calibrated slopes for 2T, 1T and 1/2T sizes, top to bottom. Graphical representation in dashed line of E399 (5.1) and the inverse (5.3) from the experimental data.

Moreover, based on the selection of data, one can interpolate over each specimen individually or the sorted, by stiffness/compliance, data for all specimen and cycles (by size). The latter option provides more uniformly spaced crack lengths, although overestimating over the initial cycles for some specimens. As the relative standard deviation between in the initial stiffness values of the specimens is about 3 % (2.5 % for 2T and 3.2 % for 1/2T and 1T), by picking the stiffest of the specimen and setting it to either the initial $a_0 = 0.35$ or the value given from the E399 function, one might end up with initial a_0/W, for the most compliant specimens, well over 0.38 which is far from the case. Either using the calibrated displacement at the integral knife edges or the experimental, measured at the points of the attachable knife edges, would produce very similar results based on the nature of the interpolation. Based on the above, the interpolation is calculated for each specimen individually and with an initial $a_0/W = 0.35$ matching the manufacturer's and camera's values.

Optical measurements

As described in 5.1.2 up to 1100 images were taken per specimen. These images were named chronologically with the load in the file name which eased

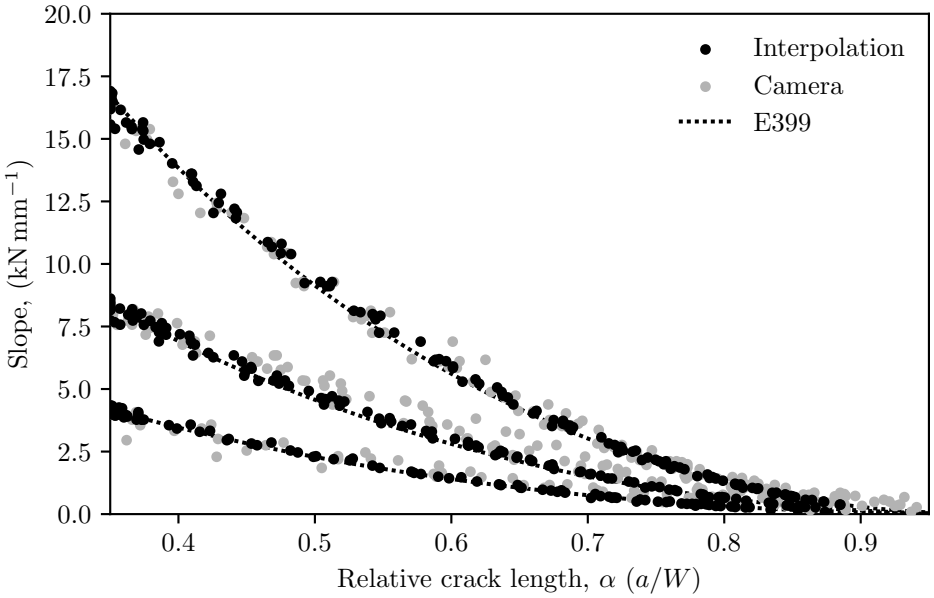

Figure 5.17: Relative crack lengths-calibrated slopes for 2T, 1T and 1/2T sizes, top to bottom. Graphical representation in dashed line of E399 (5.1), the crack lengths from the interpolated calculated compliance and from the optical measurements.

the analysis.

The images per each specimen where imported to ImageJ (v.1.47), an open-source image processing program [127]. As the images where named chronologically, they were imported as an image sequence. As each image was about 5 MB, each sequence would require reasonable amounts of RAM up to 5.5 GB. With enough amount of RAM the user could scroll with ease over the images and cyclic loadings as well as batch edit the image sequence. Each sequence was contrast enhanced by 2 % and normalised. The above made the determination of the crack tip in each loading and by extension the crack length measurements, after a scale was determined (specimen width) much easier.

The results of the optical crack length measurements as well as the compliance interpolation method against the E399 function (5.1) can be seen in Figure 5.17. As not every cycle produced a visible crack increase by the optical measurements, the later cycles with the same crack length were omitted when plotted.

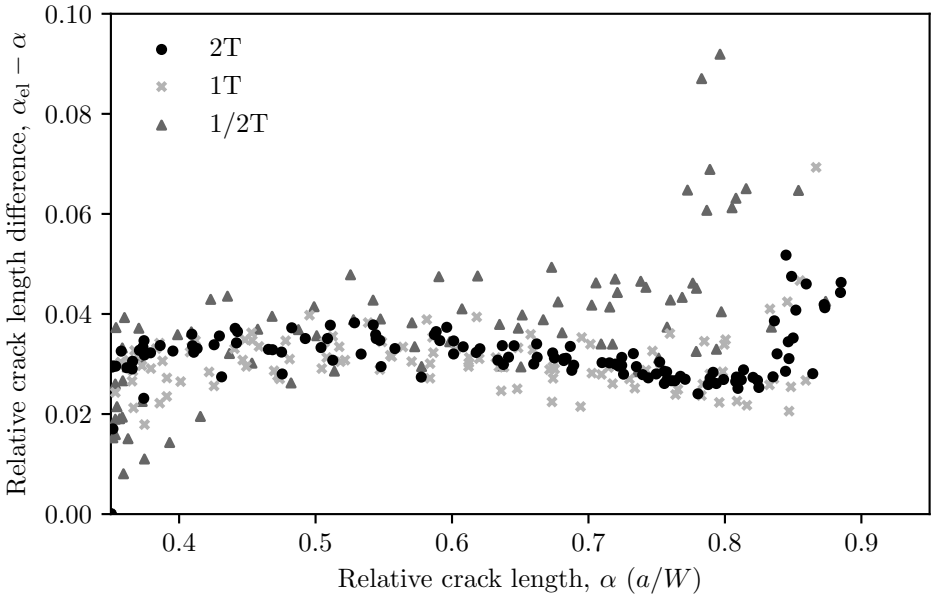

Figure 5.18: Relative crack lengths from the interpolation of the unloading line compliance-difference between the elastic compliance crack length and the one used in the X axis, for all specimen sizes.

Elastic compliance

Anderson [31], based on ASTM-E561, suggests the use of elastic compliance, described as effective compliance. The elastic compliance is the calculated compliance (unloading line) minus the intercept (plastic deformation, residual strain etc.), basically rotated from the point on the load line to the origin. The compliance for each subsequent cycle, based on the increasing residual strain, will get an extra elements in increasing and be higher than the ones calculated by the linear regression functions on the unloading line. Figure 5.18 highlights the difference between the two for the interpolated crack length based on the linear regression compliance. Although the crack lengths in the final cycles ($\alpha > 0.8$) may be better estimated with the use of this method, compared to the underestimation seen in the other methods, the overestimation in the rest of the crack length range deems it unacceptable. A discussion will be had on the underestimation of the effective crack length in the discussion section.

5.3.3 K_{R} calculations

Figures 5.19, 5.20 and 5.21 show the K_{R} with the increasing normalised crack lengths for the three different specimen sizes. The above figures were plotted with the K values estimated following the functions as given by the E399 standard with K_{Q} replaced by K_{R}:

$$K_R = \frac{P}{B\sqrt{W}} f\left(\frac{a}{W}\right) \tag{5.6}$$

with:

$$f\left(\frac{a}{W}\right) = \frac{\left(2+\frac{a}{W}\right)\left[0.886 + 4.64\frac{a}{W} - 13.32\left(\frac{a}{W}\right)^2 + 14.72\left(\frac{a}{W}\right)^3 - 5.6\left(\frac{a}{W}\right)^4\right]}{\left(1-\frac{a}{W}\right)^{3/2}} \tag{5.7}$$

where P the load, B the specimen thickness and W the specimen width.

The load used for each cycle is the maximum load for each cycle, apart from the initial loading which is excluded from these calculations and will be examined in the subsection below. For the crack length estimates, the interpolation method on the linear regression of the unloading compliance was used.

The apparent underestimation of the effective crack lengths in the later stages ($\alpha \geq 0.8$), as seen in Figure 5.17 might provide conservative results over this stage. Compared to the alternative of optical measurements, the method used produces much less scatter, as expected, over the length of the ligament with the average K_{R} much lower than the one found from the overestimated optical crack measurements. The same applies to the overestimated crack lengths obtained using the linear compliance interpolation, albeit with less scatter compared to the optical. The E399 function provides same results with the interpolation method used.

There are some differences between the specimen sizes, especially over the early stages, where all the crack estimation methods are in agreement. An overview of the 7.5 mm to crack extension ($a - a_0$) can be seen in Figure 5.22. There is an initial rise in the K_{R} values, which differ initially for each specimen size. For the 1/2T, these initial values ($\alpha < 0.37$) show a mean of $1.05\,\mathrm{MPa\,m^{1/2}}$, for the 1T $1.20\,\mathrm{MPa\,m^{1/2}}$ and for the 2T $1.44\,\mathrm{MPa\,m^{1/2}}$.

A plateau region region is reached, more apparent in the two largest sizes

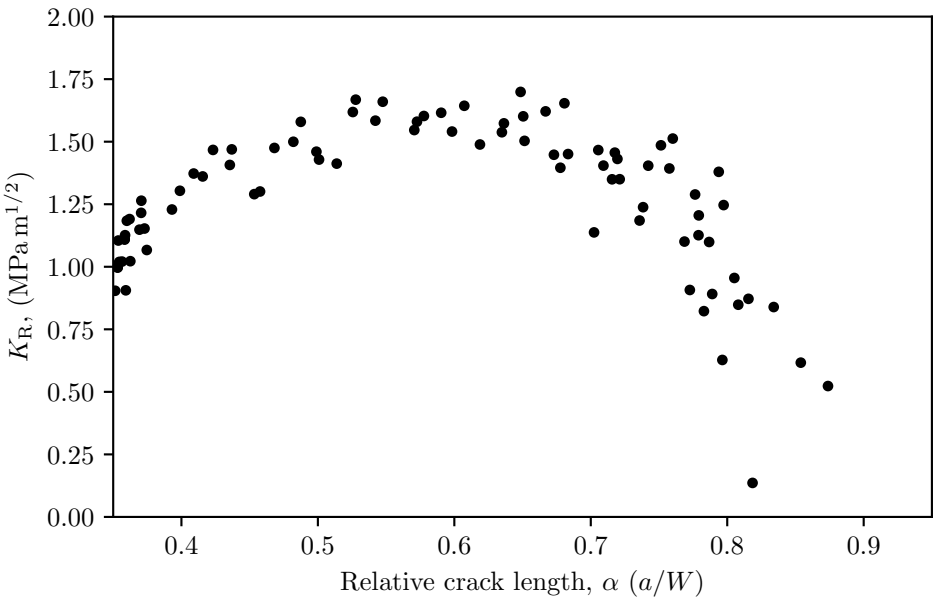

Figure 5.19: Relative crack lengths-K_R, 1/2T size. Graphical representation of K_R based on E399 K function. Peak cycle loads loads are used with respect to crack lengths from interpolation on the inelastic unloading compliance.

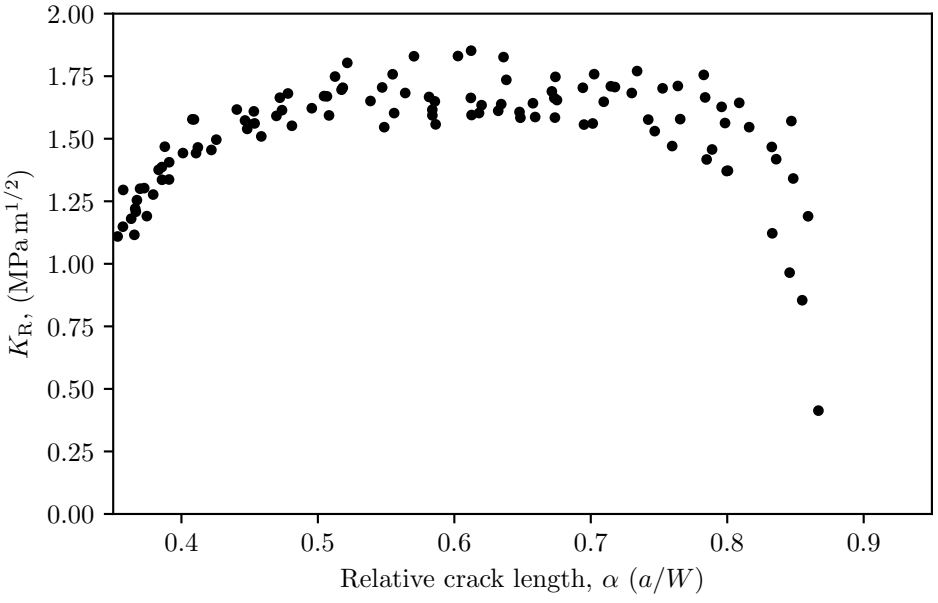

Figure 5.20: Relative crack lengths-K_R, 1T size. Graphical representation of K_R based on E399 K function. Peak cycle loads loads are used with respect to crack lengths from interpolation on the inelastic unloading compliance.

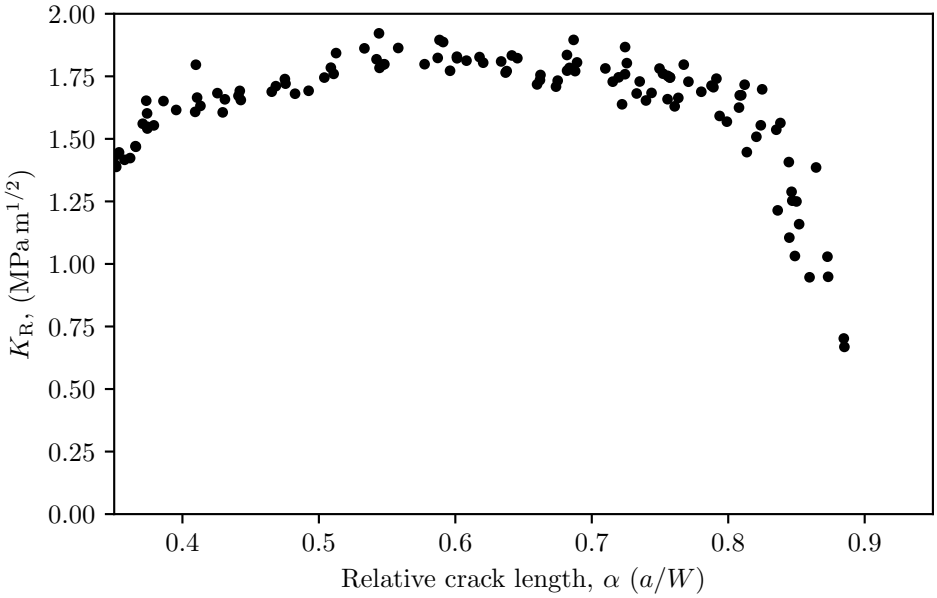

Figure 5.21: Relative crack lengths-K_R, 2T size. Graphical representation of K_R based on E399 K function. Peak cycle loads loads are used with respect to crack lengths from interpolation on the inelastic unloading compliance.

1T and 2T. The plateau values are arguably reached for the 1T specimens at lengths of about $\alpha = 0.5$ (Figure 5.20), equivalent to about 7.5 mm of crack extension, where for the 2T specimens the plateau is reached at lengths closer to $\alpha = 0.42$ (Figure 5.20) with about the same crack extension. A distinct plateau region for the smallest 1/2T specimens is not reached, with the decline of the K_R values starting at about $\alpha = 0.65$ (Figure 5.19) or about 7.5 mm of crack extension in the 16.25 mm initially uncracked ligament. Mean values for the plateau regions of 1/2T are 1.60 MPa m$^{1/2}$, for the 1T 1.66 ± 0.08 MPa m$^{1/2}$ and for the 2T 1.74 ± 0.05 MPa m$^{1/2}$. The fall in K_R for the 1T appears to start at about $\alpha = 0.75$ and for the 2T closer to $\alpha = 0.8$.

5.3.4 Size effect

For the calculation of K_{If} based on the methods of Bažant, the determination of initial load to produce a visible stable crack is needed. Accuracy on the load measurements is essential as the same percentage increase in load produces the equivalent increase in apparent fracture toughness K_Q for the same initial conditions (α_0 and B). Two methods were used to determine the initiation load; the optical, based on the load in each image name, and a CMOD (or

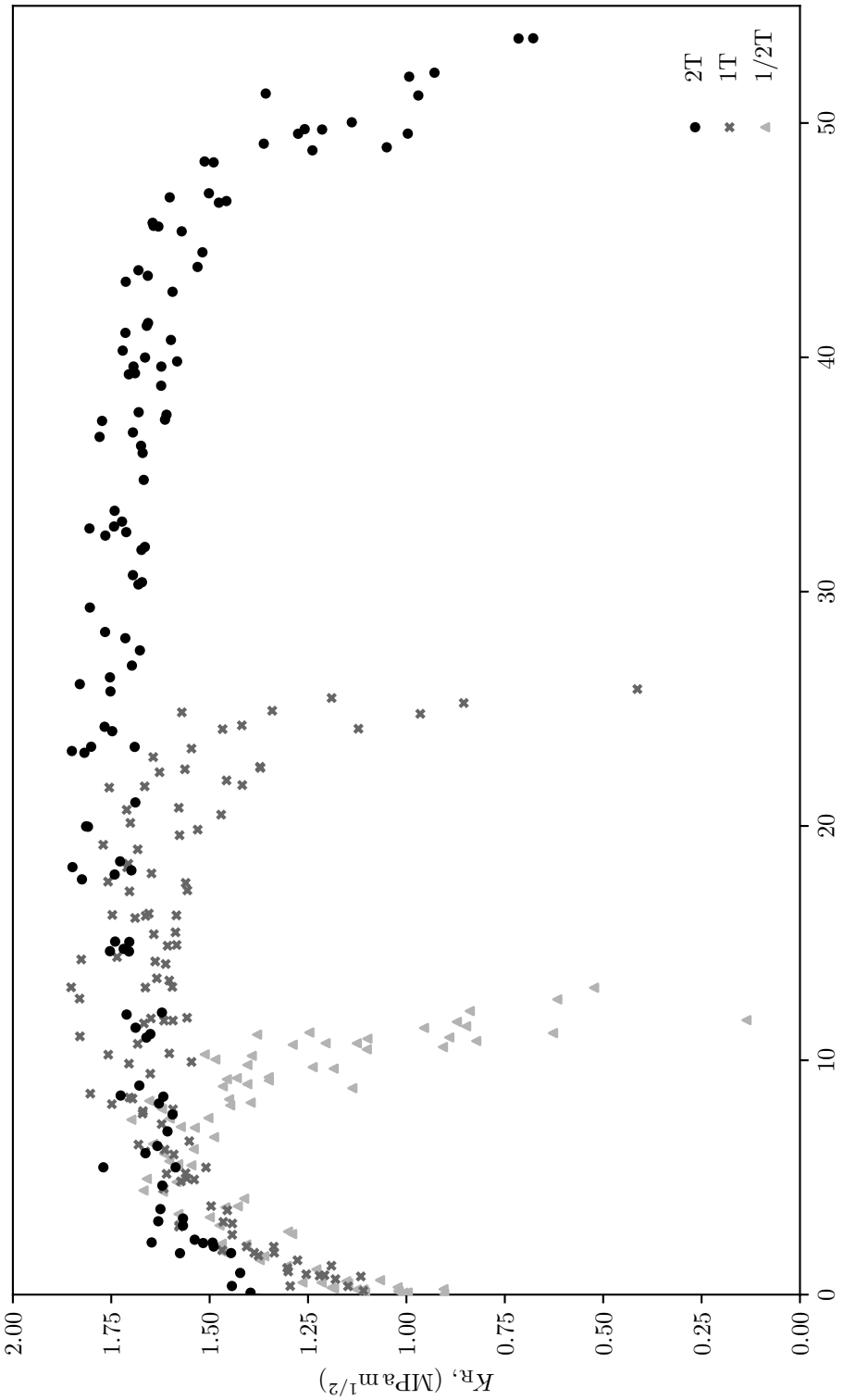

Figure 5.22: Crack length extensions $\alpha - \alpha_0$-K_{R}, all sizes.

displacement) correlation to load.

During the experiment, as the load was approaching the peak values, the image capturing frequency was manually changed to 1 Hz, which meant, based on the loading rates and initial stiffness, that each image would be about 1 N, 2 N and 5 N apart, for each specimen size during stable loading. Subsequently, with the assumption that each visible crack initiation occurred at the image attributed by the author, peak loads and K_{Q} values would produce errors of less than 1 %.

Moreover, as an extra safety measure for the load approximation, a rolling Pearson correlation function from Python was used (pandas.rolling.corr) [128]. Pearson correlation r is calculated for a sample (the rolling window) as:

$$r = \frac{\sum_{i=1}^{n}(x_i - \bar{x})(y_i - \bar{y})}{\sqrt{\sum_{i=1}^{n}(x_i - \bar{x})^2}\sqrt{\sum_{i=1}^{n}(y_i - \bar{y})^2}} \tag{5.8}$$

The values of the coefficient vary from 1 to -1 for fully positive and fully negative correlation, with 0 the value for no correlation at all. Figure 5.23 shows the increasing load plotted against the sample correlation coefficient for specimen 1/2T1. The drop in the coefficient signifies a non-linearity between the sample (load, CMOD). The first image in which a crack was spotted for the specific specimen was at 299 N, very close to the value from the drop in the correlation at about 301 N. The above correlation is very sensitive to window size and number of data points and proved to be quite difficult to incorporate as a general solution to the analysis scripts.

Size independent values

Based on the loads determined by the optical measurements and validated by the correlation method, the apparent toughness values K_{Q} were found, $1.00 \pm 0.03\,\mathrm{MPa\,m^{1/2}}$, $1.13 \pm 0.06\,\mathrm{MPa\,m^{1/2}}$ and $1.36 \pm 0.03\,\mathrm{MPa\,m^{1/2}}$ for the 1/2T, 1T and 2T specimen sizes respectively. To determine the size independent values for c_f, the equivalent fracture process zone and K_{If}, the fracture toughness, both at an infinite specimen size, the following steps were required.

Firstly, the shape independent sizes of the specimen, $\bar{d}$ (or sometimes seen as D) need to be evaluated. To calculate $\bar{d}$ the equation below was used:

$$\bar{d} = \frac{g\left(\alpha_0\right)}{g'\left(\alpha_0\right)} d \tag{5.9}$$

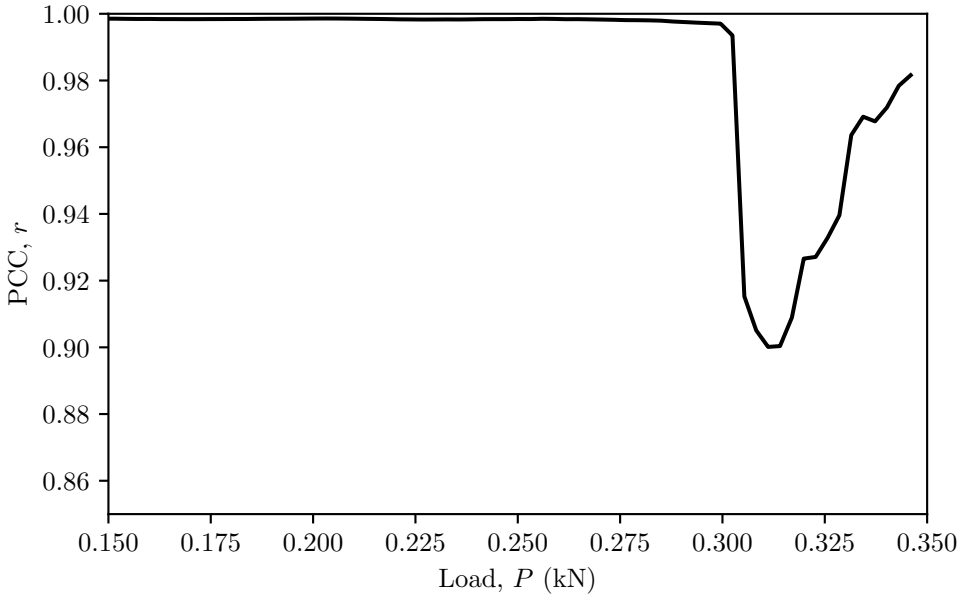

Figure 5.23: Load-rolling Pearson correlation coefficient, for specimen 1/2T1.

with $g(\alpha) = f(\alpha)^2$ with $f(\alpha)$ from the C(T) E399 function seen in 5.7, d the specimen width and $\alpha_0 = 0.35$. The $g(\alpha)$ and $g'(\alpha_0)$ functions were determined by a symbolic solver (sumpy.solvers) from the SumPy library in Python. After initial hand calculation testing, $f(\alpha)$ was fed to the solver and $g(\alpha)$ and its prime were calculated.

From the calculation of $\bar{d}$, a linear interpolation of $x = 1/\bar{d}$ and $y = 1/K_{\mathrm{Q}}^2$ using the scipy.stats.linregress was performed [114]. Following Bažant's law, as can be seen in the literature review in section 2.4, the intercept would be equal to $1/K_{If}^2$ and the slope equal to c_f/K_{If}^2. Following the interpolation the $c_f = 6.29\,\mathrm{mm}$ and $K_{If} = 1.50\,\mathrm{MPa\,m^{1/2}}$.

Figure 5.24 shows the brittleness number against the apparent fracture toughness for the three specimen sizes. Also the asymptote to K_{If} is plotted based on (2.33). To determine the brittleness number the shape independent size factor $\bar{d}$ for each specimen was divided by the equivalent process zone c_f. The above gave brittleness numbers of 0.77, 1.55 and 3.10 for the 1/2T, 1T and 2T specimen sizes respectively. The asymptote at the above brittleness numbers gave K_{Q} values of $0.99\,\mathrm{MPa\,m^{1/2}}$, $1.17\,\mathrm{MPa\,m^{1/2}}$ and $1.31\,\mathrm{MPa\,m^{1/2}}$. Based on the size effect law, the brittleness numbers are well within the law limits of non-linear fracture mechanics of $0.1 < \beta < 10$. A fully linear elastic (LEFM) IM1-24 C(T) specimen ($\alpha_0 = 0.35$), according to the law ($\beta \geq 10$),

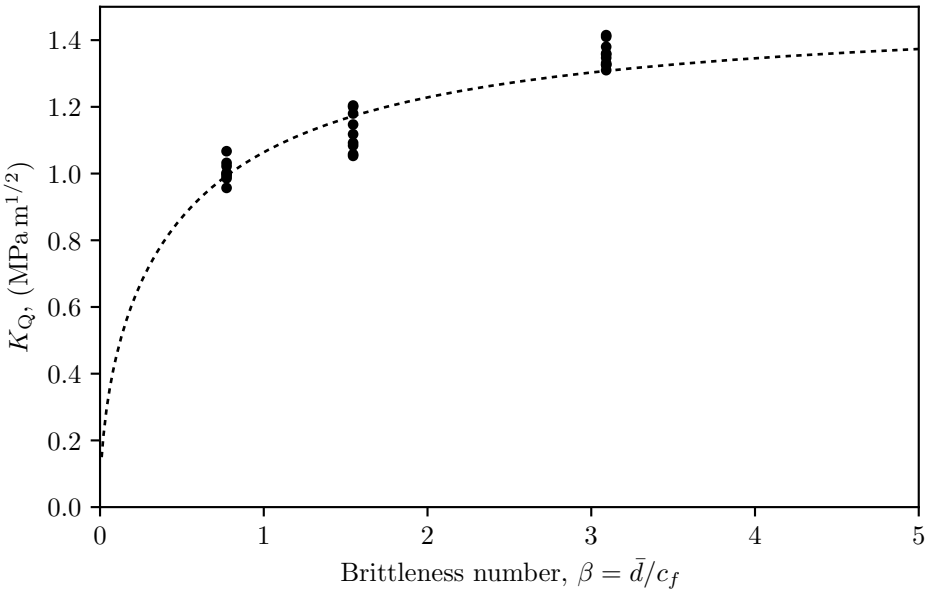

Figure 5.24: Brittleness number-apparent fracture toughness for the different specimen sizes, left to right, 1/2T, 1T, 2T. Equivalent frontal zone length $c_f = 6.29\,\text{mm}$ and $K_{If} = 1.50\,\text{MPa}\,\text{m}^{1/2}$.

would need to be more than 325 mm in width.

5.3.5 R curves

For the energetic calculations to produce comparable results, the experimental crack mouth opening displacement had to be calibrated to the load line. Subsequently, the energetic calculations would be corresponding to the load line. Similarly to the E399 calibration, a function of crack length was used from a performed FE analysis, fitted by Python's numpy.polyfit. $\Delta_c = k\Delta_{ll}$ with $k = -0.5403\alpha^3 + 1.8168\alpha^2 - 2.4732\alpha + 2.3583$ with Δ_c the experimental crack mouth opening displacement, Δ_{ll} the displacement measured at the load line. The analysis showed negligible differences for the different specimen sizes and thus the equation for the 1T specimen was used. Moreover, the correction on compliance for specimen rotation, according to the functions of the E1820 standard, produced, for the ranges of CMOD and specimen sizes, corrections of less than 1 % and was considered insignificant.

The crack lengths, were re-evaluated and plotted against the E1820 compliance function [61], using the same method as above, with the addition of the camera lengths, presented in Figure 5.25. As can be seen, the calibration leads

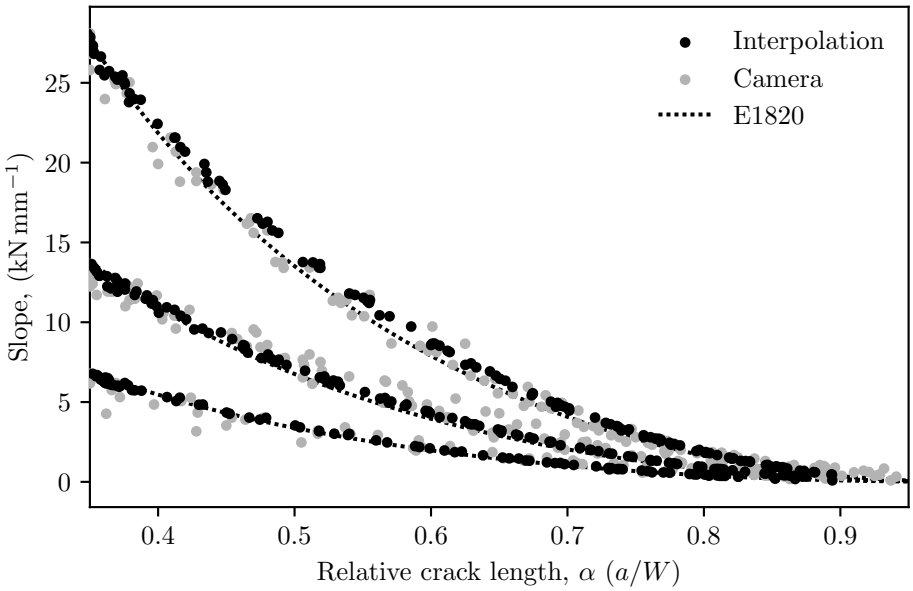

Figure 5.25: Relative crack lengths-calibrated slopes for 2T, 1T and 1/2T sizes, top to bottom. Graphical representation in dashed line of E1820 equation, the crack lengths from the interpolated calculated compliance and from the optical measurements.

to minimal overestimation over the crack lengths of $0.45 < \alpha < 0.7$. Based on the above, the calibration deemed acceptable.

Calculation of R

Figures 5.26, 5.27, 5.28, show the produced R-curves for the three specimen sizes following the graphical method presented in 2.3.1. According to the method, R is produced as the graphical area between two subsequent loadings divided by the cracked ligament area.

In order to get the area between cycles, the Python function numpy.trapz was used, independently for each loading. This function integrates over a given axis using the composite trapezoidal rule. In order to minimise the error based on the irregularities of the load and displacement with the trapezoidal rule, both were interpolated with the method seen in 5.3.1. With the interpolation, many perfectly spaced points leading to a minimum dx were provided.

For the first cycle, the interpolation and calculation of area was done to the point where the unloading would start for the subsequent cycle. Additionally, for the following cycle, the area calculated was up to the point where the

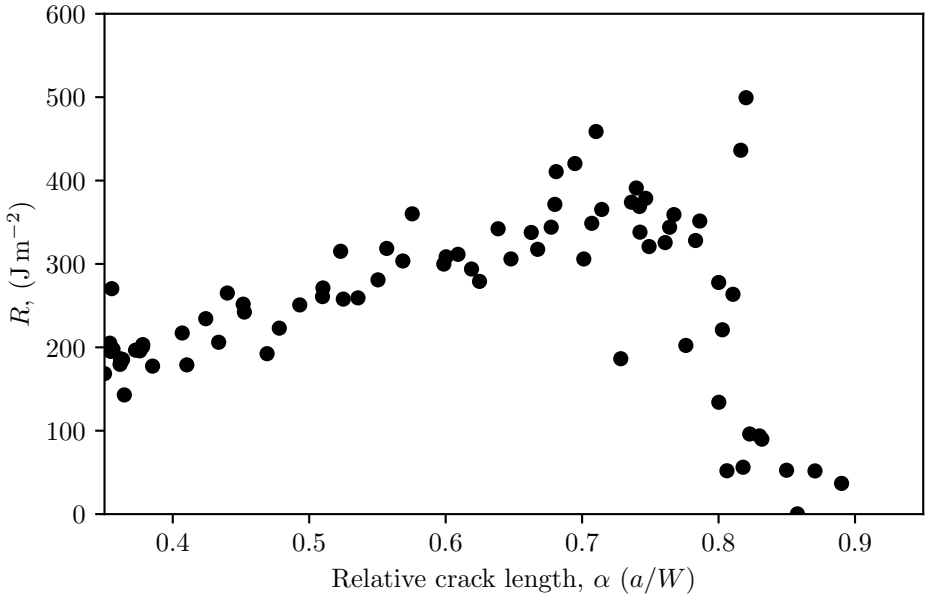

Figure 5.26: Produced R-Curve for the 1/2T size specimens. Crack length estimates based on compliance interpolation.

previous cycle stopped. This ensured the subtraction of these areas would produce realistic results. The cases where the unloading was triggered during an unstable fracture and thus leading to errors from the method above were minimal and corrected manually, without a general solution. Moreover, the areas below the minimum loads were calculated by the triangle from the intercept on the displacement axis and the reloading slope of each cycle. These areas were subtracted and added to the calculated area from above. The equivalent crack lengths estimated from the interpolation of the unloading compliance were used and by subtracting their lengths and multiplying by the specimen thickness the cracked area was calculated.

Results show a general increase in R with crack length. For the smallest 1/2T specimen, although the results were scattered due to the nature of graphite, R rose from an initial point of about $180\,\mathrm{J\,m^{-2}}$ to values about $350\,\mathrm{J\,m^{-2}}$ with its values declining from approximately $\alpha = 0.75$. For the 1T specimen, R rose from an initial point of about $220\,\mathrm{J\,m^{-2}}$ to values about to $370\,\mathrm{J\,m^{-2}}$ with a decline from $\alpha = 0.85$ onwards. The largest 2T specimen initially exhibits R of $250\,\mathrm{J\,m^{-2}}$ to values about $380\,\mathrm{J\,m^{-2}}$ with a decline as well, from $\alpha = 0.85$ onwards.

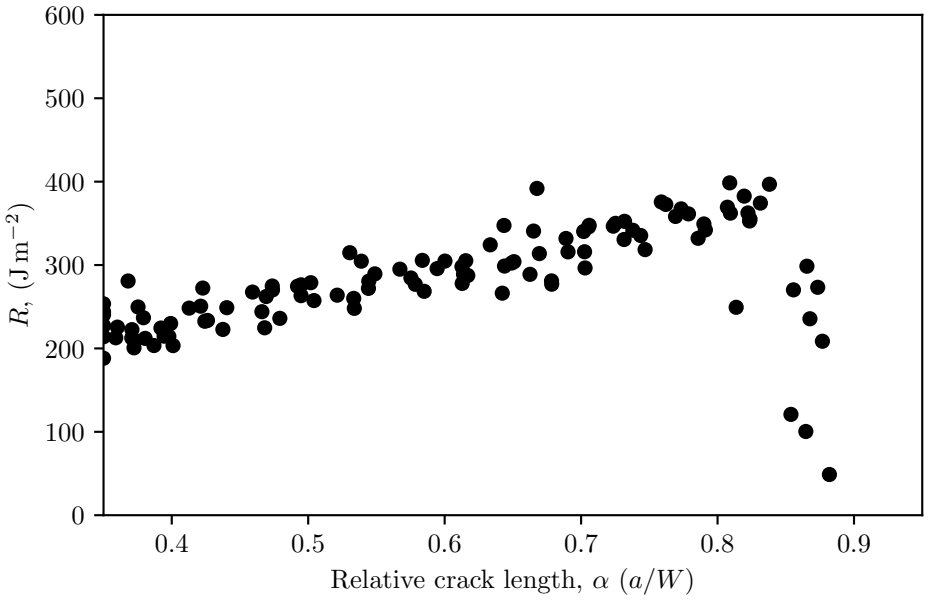

Figure 5.27: Produced R-Curve for the 1T size specimens. Crack length estimates based on compliance interpolation.

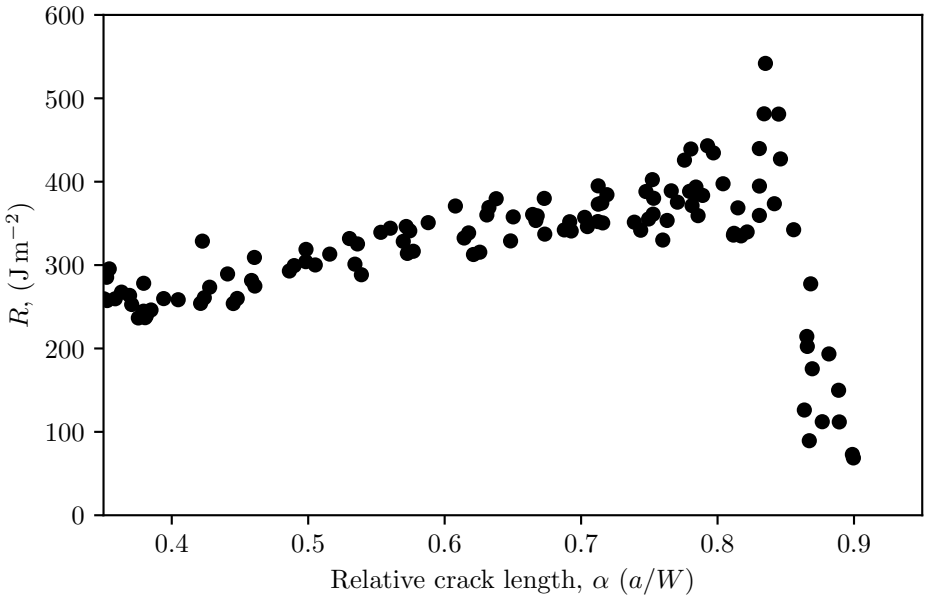

Figure 5.28: Produced R-Curve for the 2T size specimens. Crack length estimates based on compliance interpolation.

Table 5.2: Comparison of LEFM and R_{ini} contributions to γ_{wof}.

Size	$2\gamma_{wof}(K_{\text{ini}})$, ($\text{J m}^{-2}$)	R_{ini}, (J m^{-2})	LEFM %
1/2T	100	180	55 %
1T	127	210	60 %
2T	184	250	74 %

Table 5.3: Comparison of LEFM and R_{pla} contributions to γ_{wof}.

Size	$2\gamma_{wof}(K_{\text{pla}})$, ($\text{J m}^{-2}$)	R_{pla}, (J m^{-2})	LEFM %
1/2T	256	350	73 %
1T	275	370	74 %
2T	306	380	80 %

Work of fracture

Work of fracture is the mean energy expenditure per unit area to propagate a crack over the whole specimen. The direct comparison between the total work and the work needed at the plateau region for each size can be performed by the use of the R-curve. The R-curve enables us to calculate the work of fracture from:

$$2\,\gamma_{wof} = \frac{\int_0^S R\,(A)\,dA}{S} \tag{5.10}$$

The mean work was found $121 \pm 10\,\text{J m}^{-2}$ (1/2T), $139 \pm 7\,\text{J m}^{-2}$ (1T) and $157 \pm 6\,\text{J m}^{-2}$ (2T). With $\gamma_{wof} \approx R/2$, the values for the greater regions of R for each specimen can be approximated at $175\,\text{J m}^{-2}$, $185\,\text{J m}^{-2}$ and $190\,\text{J m}^{-2}$.

Based on Sakai's suggestion [47], the hypothetical $\gamma_{wof}(K_{\text{Q}}) = K_{\text{Q}}^2/E$ can be introduced to describe the work of fracture to extend the crack and form the process zone without the contribution of other irreversible processes. Also, in the same manner as above, $2\gamma_{wof}(K_{\text{R}}) = K_{\text{R}}^2/E$ can be used to describe the work attributed to the bridging particles at the plateau values, in addition to $\gamma_{wof}(K_{\text{Q}})$. The above are compared in tables 5.2 and 5.3, with $K_{\text{Q}} = K_{\text{ini}}$ and $K_{\text{R}} = K_{\text{pla}}$, based on the assumption that the Young's modulus remains constant.

5.4 Discussion

5.4.1 Unloading compliance

The curved paths according to Sakai are due to "energy dissipated by plastic deformation during the artificial loading-unloading" with the loading path being above the unloading. Based on Jenkins [45], during this hysteresis, the graphite remains elastic as subsequent cycles between the same stress limits produce identical loops. The curvature of these paths is a characteristic of graphite behaviour and no further explanations can be found in the bibliography.

Apart from Shah [129], where the use of the whole hysteresis loop is recommended, the discussions on methodology regarding the compliance measurements seem to have settled. The use of the unloading compliance is suggested by many, though not offering specific explanations, for the determination of the effective crack length. Karihaloo [79], suggests the use of unloading compliance and for example Hodgkins [5] used it throughout his work.

Figure 5.15 showed the less scatter produced by the unloading compliance compared to the reloading and was preferred to the whole loop based on its wide use. The above was based on the assumption that equivalent slopes would have similar intercepts (offsets).

Moreover, the additional suggestion by Anderson [31] for use of the elastic compliance was deemed unnecessary, especially on experimental data with cyclic loading where the unloading compliance could be easily estimated. As the elastic compliance would introduce overestimations over the apparent one, it would have the same effect on crack length [18], as can be seen in Figure 5.18, based on all of the examined non-optical crack length estimation methods.

These large hysteresis loops are associated with quasi-brittle materials as also seen in subsection 2.3.1. No further explanation can be found in the bibliography.

5.4.2 Crack length estimations

The crack estimations presented in this work can be divided into two categories, compliance based and optical. With the presence of cyclic loadings and accurate displacement measurements, compliance methods seem to fare better

for the calculations of equivalent crack lengths, although not irrespective of method.

Liu *et al.* [70] demonstrated that for concrete, the crack front is not straight. Through the thickness of the specimen, the side faces showed greater crack lengths compared to the middle, prevalent at increased crack lengths compared to lengths close to α_0 where the effect is minimal. Hodgkins [5], showed the same effect with several X-ray microtomography scans over repetitive loadings on C(T) specimens irrespective of specimen thickness or presence of side grooves.

The interpolation provided similar results compared to the property dependant standard functions, seen in Figure 5.17. The results seem clustered, especially compared to the interpolation of the whole data set for each specimen size. Provided there are adequate cyclic loadings and thus compliance measurements the linear interpolation of each specimen separately is preferred. Due to the inhomogeneous nature of IM1-24, relatively scattered values of initial compliance (C_{α_0}), especially with decrease in specimen size were found. This would lead to overestimations of crack lengths when the lowest compliance specimen, likely an outlier, would be assigned as α_0.

Based on the above methods, and for the case of graphite, it can be concluded, fulfilling an experimental objective, that accurate crack measurements, especially at greater crack extensions, can be produced mostly through cyclic loadings and compliance measurements. The optical measurements, although measuring actual and not effective crack lengths, proved to be inconsistent.

5.4.3 Fracture toughness $K_{\mathbf{R}}$

Figure 5.22 shows a clear initial rise in the first 7 to 9 mm of crack extension for all specimen sizes. The smallest 1/2T specimens (Figure 5.19) do not exhibit a steady plateau state, compared to the other two. The plateaus reached by the two bigger specimens are at $1.66\,\mathrm{MPa\,m^{1/2}}$ and for the 2T $1.74\,\mathrm{MPa\,m^{1/2}}$ with values more scattered for the smaller of the two, similar to the $1.65\,\mathrm{MPa\,m^{1/2}}$ value reported in Ouagne's work [6, 57].

The initial rise is mainly attributed, throughout the bibliography, to the bridging particles at the wake of the crack based on the works of Sakai *et al.* [47, 130]. Based on the above and the agreement in crack length measurements at lengths relatively close to α_0, it can be concluded, with a relative

certainty, that the formation of the bridging zone takes place over these initial 7 to 9 mm and can describe its length based on the steady states. Although bridging particles have been spotted well behind the wake and the length of the estimated bridging zone length [5], these are rare and their effect on K_{R} minimal. The estimated bridging zone length is well within the reported values of about 7 mm [18, 57].

Although there is some consistency in the initial rising part of the K_{R} curves, the falling behaviour, apart from the 1/2T specimen, might as well be described as a function of α rather than crack extension. The falling behaviour of the K_{R} was shown to be at 8 mm, 10 mm and 20 mm before the back face of the specimens for increasing specimen sizes.

Sakai *et al.* [47] argue the falling behaviour might be due to the interaction of the fracture process zone with the back face of the specimen. That may well be the case, although a systemic underestimation of effective crack size, or increased irregularities on the crack tip, both at the later stages, alongside the K function might a produce falling behaviour where there is none. On the contrary, using methods which systematically overestimate crack sizes (optical), might lead to a rising, on the later stages, K_{R} behaviour [6, 18, 57]. Based on the above, the methodology to estimate the fracture process zone size by the falling K_{R} behaviour threshold may lead to errors.

5.4.4 Apparent toughness and size effect

Though the optical measurements were inadequate to estimate the crack lengths during the later stages of loading, they proved very useful in determining crack initiation. Through the initiation loads as seen from the optical image file names, with the added correlation check, the apparent fracture toughness for each of the specimens was calculated. The very slow loading rates and the higher image capturing frequency in addition to the correlation check guaranteed a value for the apparent toughness K_{Q}, as shown earlier, with errors of less than 1 %. An increase in apparent toughness with specimen size was shown, at means of 1.00, 1.13 and 1.36 $\mathrm{MPa\,m^{1/2}}$ for the three specimen sizes.

This effect is well-documented in quasi-brittle materials, from mortar [131], cement [132, 133] as well as other graphite grades [85]. Although this might be counter intuitive based on a weakest link assumption, it verifies the existence of a size effect. The deviation from LEFM and the material property K_{Ic},

seen in these tests, can be explained by the formation of a process zone with adequate size to influence the behaviour of the specimen. As the process zone is defined by the properties of the material's microstructure, its scalability to the geometry size is mismatched. The rise in K_{Q} can be explained by the decreasing softening behaviour contribution of the process zone, with increase in specimen size.

Figure 5.24 shows the size effect between the specimen sizes, with the dashed line being the predicted values on differently sized specimens. These predictions can be made after the calculation of the size of the process zone in an infinitely sized specimen $c_f = 6.29\,\mathrm{mm}$ and the critical stress intensity factor $K_{\mathrm{I}f} = 1.50\,\mathrm{MPa\,m^{1/2}}$. Moreover, the brittleness number β, the dimensionless measure of proximity to either yield criterion or LEFM could be calculated for any specimen type of IM1-24. The minimum size required for a C(T) (E399) specimen to produce LEFM results ($\beta \geq 10$) is, based on the law, 325 mm in width.

5.4.5 R curves and work of fracture

The R values for the three specimens were calculated, seen in Figures 5.26, 5.27 and 5.28. The initial values of $180\,\mathrm{J\,m^{-2}}$, $210\,\mathrm{J\,m^{-2}}$ and $250\,\mathrm{J\,m^{-2}}$ show a size effect, with the higher values differing less between the sizes at about $350\,\mathrm{J\,m^{-2}}$, $370\,\mathrm{J\,m^{-2}}$ and $380\,\mathrm{J\,m^{-2}}$. This is somewhat consistent with the exhibited K_{R} curves although the rise happens in a more gradual manner. A very small plateau is reached, especially compared to K_{R}.

These results (1T specimen) show similarities with the values produced by the Type A (short) specimen employed by Hodgkins [5] with initial values of $230\,\mathrm{J\,m^{-2}}$ to plateau values of $370\,\mathrm{J\,m^{-2}}$, as can be seen in Figure 2.8. There was no sharp increase as seen in Ouagne's work [57], where a plateau value is reached in the same manner as K_{R}, in about 7 mm of crack extension. Due to the sensitivity of the measurements to specimen geometry, direct comparison between the values of this work and the bibliography cannot be facilitated as most specimens previously used did not rigorously follow the standards.

Fall in values is exhibited at, 6.5 mm, 8 mm and 15 mm before the back face of each specimen size from smallest to largest. Although for the smallest two of the specimens, this can be attributed to the interaction of the process zone and the back face, this is not the case for the largest one. Although

slight under or overestimation of crack lengths might not pose a problem as the calculation of R is based on subsequent crack length differences, the last cyclic load might lead to misinterpretations.

Cyclic loadings were performed in a similar manner between sizes, with crack lengths at the final cycles of about $\alpha = 0.85$ and stiffness at about 4 % the initial. As the specimens were loaded to failure, for the last cycle, the cracked ligament was estimated as the total remaining at the start of the loading. The above led to lowered R values due to processes in the specimen during the last cycle, not necessarily at the initial crack length which especially in the case of 2T might lead to wrong conclusions. Based on the above, although the results were more scattered, the 1/2T specimen might paint a clearer picture, with the approximate process zone length of 6.5 mm, value close to the infinite zone estimated from the size effect law.

The work of fracture from the R curves was found to be 121 ± 10, 139 ± 7 and $157 \pm 6\,\mathrm{J\,m^{-2}}$ for the three specimens (1/2T, 1T, 2T), more scattered, as expected due to size, for the smallest specimen. The above discrepancies may be explained from the contributions of the R curve itself and from the differences due to the size effect.

Firstly, more of the fracture process of the larger specimens is spent in the higher region of R, with larger contribution of energy compared to the initial and falling regions. Additionally, the LEFM contributions, especially for the initial cycles (table 5.2), are increasing with size as well. These contributions will provide more resistance to fracture and thus more work will be needed, especially compared to the softening behaviour attributed to the formation rather than propagation of the process zone and bridging particles seen in table 5.3.

Chapter 6

Conclusions

Manufactured graphite can be used in the core of a nuclear reactor to moderate fast neutrons emitted after fission of the fuel. The graphite blocks act as a moderator but also as a structural component, providing a channel for the coolant as well as the control and fuel rods. Due to the severe operational environment, macrocracks form in the graphite bricks. This is a common occurrence for all the AGRs operating in the UK, limiting the life extensions afforded them.

The project's aim was to develop a greater understanding of the initiation and mostly of the thresholds of unstable fracture of nuclear graphite and more specifically virgin IM1-24. A first objective was to employ a method of estimating the stability of various specimens, configurations and loading conditions. Moreover, to settle on the experimental procedures in order to further determine the fracture resistance and other fracture parameters for different sized specimens and to compare the findings and derive size independent material fracture properties.

6.1 Overall conclusions

An equilibrium dimensionless method and a simple series fracture model were utilised and expanded upon to estimate stability of various specimens, configurations and loading conditions. Despite problems drawing exact parallels between fracture in industrial environments and theoretical predictions, it was shown that the dimensionless method can offer insights on the thresholds of stability in various specimens.

Differences between the dimensionless equilibrium and a simple series fracture model with variable spring compliance were also examined. The dimensionless equilibrium is valuable to determine the simple case of specimen stability based on its dimensionless energy. For the case of instability, especially with compliant structures in addition to the specimen, the dimensionless load and displacement can provide insight into non-static loads and snap-back behaviour. The model's behaviour compared to the equilibrium states, strictly operates, dependent on the ratio of compliances, between the limits of load and displacement control.

The model and equilibrium method underlined the theoretical influence of relative stiffness in specimen stability. In order to quantify this and further investigate, two experimental setups were envisioned. The first involved uniaxial and biaxial tests, in series, loaded against similar rigs from various materials and thus stiffness. The second setup involved a parallel three bar structure with a C(T) specimen acting as the middle bar. It was shown that the used range of stiffness and thus associated elastic follow-up did not produce a change in the fracturing behaviour of the specimens. This is true for both experimental setups, series (uniaxial, biaxial) and parallel (C(T) in three bar).

A secondary point of interest emerged as a result of the uniaxial and biaxial series test. Despite the influence of load multiaxiality on fracture stress of graphite seen in previous works [105–107], there was little effect in post-peak fracture behaviour indicating a lack of influence on fracture stability. Additionally, the flexural strength of IM1-24 was calculated at $22.7 \pm 0.9\,\mathrm{MPa}$ for uniaxial and $23.0 \pm 1.1\,\mathrm{MPa}$ for biaxial specimens and loading. The differences seen, compared to the inconclusive results from previous studies, can be attributed to geometry factors introducing a Type 1 size effect.

To further examine the influence of size on fracture, an additional suite of experiments was proposed. Three different sized C(T) specimens were cyclically loaded to failure following the available practices and standards in the bibliography. An important outcome is a preference towards compliance crack length measurements, compared to optical which tend to diverge in later stages of fracture, leading to errors.

Based on compliance crack measurements conducted to determine K_R and R graphs, as by the research objectives, some salient features of the K_R graphs

can be underlined. A distinct initial rising part in K_{R} was seen in all C(T) specimen sizes. This can be attributed to the formation of a bridging zone with its length estimated at about $c_{\mathrm{b}} = 7\,\mathrm{mm}$. The rising part was followed by a plateau and a falling region, especially for the two largest specimens. The smallest one, with an initial uncracked ligament of $b_0 = 16.25\,\mathrm{mm}$ did not exhibit a distinct plateau, an indication of interaction with the back face of the specimen.

In pursuit of the research objectives which sought to settle on experimental procedures, comparisons were made concerning crack length measurements. Optical measurements of crack length led to overestimations, especially in the later stages of fracture. This can be the cause of rising K_{R} behaviour, in the last stage, seen in earlier studies using solely optical measurements [6, 18, 57].

Contrary to crack length measurements in the later parts, optical measurements proved instrumental in determining the load to initiate fracture. The determination of the initiation load allowed the calculation of the size effect parameters, meeting the required research objectives. Based on the size effect law, the calculation of the equivalent fracture process zone in an infinitely sized IM1-24 specimen was calculated at $c_f = 6.29\,\mathrm{mm}$. The above material property can be freely used in evaluating fracture in graphite components, including virgin graphite bricks.

A size effect can also be seen in the work of fracture, where the linear elastic contributions to work are higher with increasing specimen size, leading to an increase in total work. This is more due to the formation rather than propagation of a process zone. The above can be attributed to the size mismatch between the scaling of the zone and specimen, while considering the softening nature of the zone.

Although the research objectives have been met, full understanding of fracture in a block already in service still remains elusive. The limited readily available irradiated graphite makes testing the aged material very difficult and thus research is focused on computational and physical models. Based on the above, further experimental work should focus on general fracture principles of the interconnected bricks and the validation or better approximation of the fracture properties underlined in this work, providing the background to the computational work.

6.2 Recommendations for further work

As noted above, the range of relative stiffness used in this work, did not produce significant differences in the graphite's fracture behaviour. Further work could estimate an elastic follow-up factor due to the contributions of the uncracked area in a nuclear brick as well as the whole interconnected core, actually quantifying the effect in engineering components while making the distinction between two parts of elastic follow-up or the internal and external relative stiffness. By estimating the stiffness of cracked area, brick and core, a study can show how a growing crack in a brick can affect the behaviour of the core, especially in non-static loads.

Although this work was limited to static loading, the snap-back behaviour seen by the dimensionless equilibrium load-displacement poses the question. How would a graphite specimen behave in a non-static loading? Further work can be undertaken to examine graphite's energy absorption and stability under other loads evaluating the superposition method proposed by Bažant [37]. Results might prove useful in understanding seismic loads and their contribution to fracture.

The same experimental programme followed in this work can be applied to other specimen types of different sizes to evaluate the approach to fully linear elastic fracture mechanics. Ideally, the results will further validate and approximate the fracture material properties found in this work.

References

[1] E. Carpenter and D. Norfolk, "Lattice of power: graphite core life," *Nuclear Energy*, vol. 23, no. 2, pp. 83–96, 1984.

[2] J. Vidal and I. Sample, "Documents reveal hidden fears over Britain's nuclear plants." The Guardian, archived at: https://goo.gl/kS92FQ, July 2006.

[3] Health and Safety Executive, "Assessment of implications of full length axial crack in a graphite moderator brick." Health and Safety Executive, obtained from: https://goo.gl/eqsqd7, May 2006.

[4] D. Miller, "Cracks found at reactor at Hunterston B nuclear power station." BBC News, archived at: https://goo.gl/XAc4Xe, Oct. 2014.

[5] A. Hodgkins, *Crack propagation in nuclear graphite*. PhD thesis, University of Manchester, 2006.

[6] P. Ouagne, *Fracture property changes with oxidation and irradiation in nuclear graphites*. PhD thesis, University of Bath, 2001.

[7] J. D. Bernal, "The structure of graphite," *Proceedings of the Royal Society of London A: Mathematical, Physical and Engineering Sciences*, vol. 106, no. 740, pp. 749–773, 1924.

[8] A. W. Hull, "A new method of X-Ray crystal analysis," *Physical Review*, vol. 10, pp. 661–696, Dec. 1917.

[9] L. Girifalco and R. Lad, "Energy of cohesion, compressibility, and the potential energy functions of the graphite system," *The Journal of Chemical Physics*, vol. 25, no. 4, pp. 693–697, 1956.

[10] R. Nightingale, *Graphite in Nuclear Industry*. New York and London Academic Press, 1962.

[11] H. Lipson and A. R. Stokes, "The structure of graphite," *Proceedings of the Royal Society of London A: Mathematical, Physical and Engineering Sciences*, vol. 181, no. 984, pp. 101–105, 1942.

[12] H. Boehm and R. Coughlin, "Enthalpy difference of hexagonal and rhombohedral graphite," *Carbon*, vol. 2, no. 1, pp. 1 – 6, 1964.

[13] E. Acheson, "Manufacture of graphite," September 1896. US Patent 568,323.

[14] R. Moskovic, P. E. J. Flewitt, E. Schlangen, G. Smith, A. G. Crocker, A. Hodgkins, P. Heard, and M. R. Wootton, "Understanding fracture behaviour of PGA reactor core graphite: perspective," *Materials Science and Technology*, vol. 30, no. 2, pp. 129–145, 2014.

[15] M. Mostafavi, M. Schmidt, B. Marsden, and T. Marrow, "Fracture behaviour of an anisotropic polygranular graphite (PGA)," *Materials Science and Engineering*, vol. 558, pp. 265 – 277, 2012.

[16] S. Mrozowski, "Mechanical strength, thermal expansion and structure of cokes and carbons," in *Proceedings of the First and Second Conferences on Carbon: Held at the University of Buffalo, Buffalo, New York*, pp. 31–45, 1956.

[17] M. Joyce, T. Marrow, P. Mummery, and B. Marsden, "Observation of microstructure deformation and damage in nuclear graphite," *Engineering Fracture Mechanics*, vol. 75, no. 12, pp. 3633 – 3645, 2008.

[18] S. Fazluddin, *Crack growth resistance in nuclear graphite*. PhD thesis, University of Leeds, 2002.

[19] K. Wen, T. Marrow, and B. Marsden, "The microstructure of nuclear graphite binders," *Carbon*, vol. 46, no. 1, pp. 62 – 71, 2008.

[20] G. M. Laudone, C. M. Gribble, and G. P. Matthews, "Characterisation of the porous structure of Gilsocarbon graphite using pycnometry, cyclic porosimetry and void-network modeling," *Carbon*, vol. 73, pp. 61 – 70, 2014.

[21] A. A. Griffith, "The phenomena of rupture and flow in solids," *Philosophical Transactions of the Royal Society of London A: Mathematical, Physical and Engineering Sciences*, vol. 221, no. 582-593, pp. 163–198, 1921.

[22] C. E. Inglis, "Stresses in a plate due to the presence of cracks and sharp corners," *Transactions of the Institute of Naval Architects*, vol. 55, pp. 219–242, 1913.

[23] G. R. Irwin and J. A. Kies, "Critical energy rate analysis of fracture strength," *Welding Journal Research Supplement*, vol. 33, no. 4, pp. 193–198, 1954.

[24] G. R. Irwin, "Analysis of stresses and strains near the end of a crack traversing a plate," *Journal of Applied Mechanics*, vol. E24, pp. 351–369, 1957.

[25] A. Demaid, *Fail-safe*. Open University. Course T207, Fracture Training Associates, 2004.

[26] H. P. Rossmanith, *Fracture research in retrospect: an anniversary volume in honour of G.R. Irwin's 90th birthday*. CRC Press, 1997.

[27] H. Westergaard, "Bearing pressures and cracks," *Journal of Applied Mechanics*, vol. 60, pp. A49–A53, 1939.

[28] H. Tada, P. Paris, and G. Irwin, *The Stress Analysis of Cracks Handbook*. American Society of Mechanical Engineers, 2000.

[29] Y. W. Mai and B. R. Lawn, "Crack stability and toughness characteristics in brittle materials," *Annual Review of Materials Science*, vol. 16, pp. 415–439, Aug. 1986.

[30] G. I. Barenblatt, "The mathematical theory of equilibrium cracks in brittle fracture," *Advances in Applied Mechanics*, vol. 7, pp. 55–129, 1962.

[31] T. L. Anderson, *Fracture Mechanics: Fundamentals and Applications*. CRC Press, third ed., 2005.

[32] A. Atkins and Y. Mai, *Elastic and Plastic Fracture: Metals, Polymers, Ceramics, Composites, Biological Materials*. Ellis Horwood series in mechanical engineering, Ellis Horwood, 1985.

[33] T. D. Burchell, *Studies of fracture in nuclear graphite*. PhD thesis, University of Bath, 1986.

[34] J. Hutchinson and P. Paris, "Stability analysis of J-controlled crack growth. Special Technical Publication 668," in *Elastic-Plastic Fracture*, pp. 37–64, American Society for Testing and Materials International, 1979.

[35] P. Paris, H. Tada, A. Zahoor, and H. Ernst, *A Treatment of the Subject of Tearing Instability*. U.S. Nuclear Regulatory Commission, 1977.

[36] M. Sakai and M. Inagaki, "Dimensionless load-displacement relation and its application to crack propagation problems," *Journal of the American Ceramic Society*, vol. 72, no. 3, pp. 388–394, 1989.

[37] Z. P. Bažant and E. Becq-Giraudon, "Effects of size and slenderness on ductility of fracturing structures," *Journal of Engineering Mechanics*, vol. 125, no. 3, pp. 331–339, 1999.

[38] R. W. Davidge and G. Tappin, "The effective surface energy of brittle materials," *Journal of Materials Science*, vol. 3, no. 2, pp. 165–173, 1698.

[39] G. Jenkins, "Fracture in reactor graphite," *Journal of Nuclear Materials*, vol. 5, no. 3, pp. 280 – 286, 1962.

[40] J. Brocklehurst, "Fracture in polycrystalline graphite," *Chemistry and Physics of Carbon*, vol. 13, pp. 146–279, 1977.

[41] M. Sakai and R. C. Bradt, "Fracture toughness testing of brittle materials," *International Materials Reviews*, vol. 38, no. 2, pp. 53–78, 1993.

[42] M. Sakai, K. Urashima, and M. Inagaki, "Energy principle of elastic-plastic fracture and its application to the fracture mechanics of a polycrystalline graphite," *Journal of the American Ceramic Society*, vol. 66, no. 12, pp. 868–874, 1983.

[43] E. Orowan, "Fracture and strength of solids," *Reports on Progress in Physics*, vol. 12, pp. 185–232, Jan. 1949.

[44] J. Eftis and H. Liebowitz, "On fracture toughness evaluation for semi-brittle fracture," *Engineering Fracture Mechanics*, vol. 7, no. 1, pp. 101 – 135, 1975.

[45] G. M. Jenkins, "Analysis of the stress-strain relationships in reactor grade graphite," *British Journal of Applied Physics*, vol. 13, no. 1, p. 30, 1962.

[46] D. Kim, S. J. Oh, C. Jang, I. S. Kim, and S. H. Chi, "Fracture toughness and crack growth resistance of the fine grain isotropic graphite," *Carbon Letters*, 2006.

[47] M. Sakai, J. Yoshimura, Y. Goto, and M. Inagaki, "R-curve behavior of a polycrystalline graphite: Microcracking and grain bridging in the wake region," *Journal of the American Ceramic Society*, vol. 71, no. 8, pp. 609–616, 1988.

[48] H. Hübner and W. Jillek, "Sub-critical crack extension and crack resistance in polycrystalline alumina," *Journal of Materials Science*, vol. 12, no. 1, pp. 117–125, 1977.

[49] R. Pabst, J. Steeb, and N. Claussen, "Microcracking in a process zone and its relation to continuum fracture mechanics," *Fracture Mechanics of Ceramics*, vol. 4, pp. 821–833, 1978.

[50] R. Knehans and R. Steinbrech, "Memory effect of crack resistance during slow crack growth in notched Al_2O_3 bend specimens," *Journal of Materials Science Letters*, vol. 1, no. 8, pp. 327–329, 1982.

[51] A. Evans and K. Faber, "Crack-growth resistance of microcracking brittle materials," *Journal of the American Ceramic Society*, vol. 67, no. 4, pp. 255–260, 1984.

[52] H. Wieninger, K. Kromp, and R. F. Pabst, "Crack resistance curves of alumina and zirconia at room temperature," *Journal of Materials Science*, vol. 21, no. 2, pp. 411–418, 1986.

[53] American Society for Testing and Materials, "ASTM E399-81 - Standard Method of Test for Plane Strain Fracture Toughness in Metallic Materials," 1981.

[54] K. Ahlborn, T. Chou, Y. Kagawa, and A. Okura, "The influence of the heat-treatment temperature on the crack-growth-resistance of a fine-grained carbon," *Carbon*, vol. 31, no. 1, pp. 205 – 212, 1993.

[55] K. Hellan, *Introduction to Fracture Mechanics*. McGraw-Hill, 1985.

[56] G. Sih, *Handbook of Stress-Intensity Factors*. Lehigh University, Institute of Fracture and Solid Mechanics, 1973.

[57] P. Ouagne, G. B. Neighbour, and B. McEnaney, "Crack growth resistance in nuclear graphites," *Journal of Physics D: Applied Physics*, vol. 35, no. 9, p. 927, 2002.

[58] T. Fett, "Influence of bridging stresses on specimen compliances," *Engineering Fracture Mechanics*, vol. 53, no. 3, pp. 363 – 370, 1996.

[59] B. Allard, D. Rouby, G. Fantozzi, D. Dumas, and P. Lacroix, "Fracture behaviour of carbon materials," *Carbon*, vol. 29, no. 3, pp. 457 – 468, 1991.

[60] V. Kostopoulos, Y. Markopoulos, Y. Pappas, and S. Peteves, "Fracture energy measurements of 2-D carbon/carbon composites," *Journal of the European Ceramic Society*, vol. 18, pp. 69–79, Jan. 1998.

[61] American Society for Testing and Materials, "ASTM E1820-15a2 - Test Method for Measurement of Fracture Toughness," 2015.

[62] G. B. Neighbour and B. McEnaney, "Creep and recovery in graphites at ambient temperature: An acoustic emission study," *Carbon*, vol. 32, no. 4, pp. 553 – 558, 1994.

[63] R. Taylor, R. Brown, K. Gilchrist, E. Hall, A. Hodds, B. Kelly, and F. Morris, "The mechanical properties of reactor graphite," *Carbon*, vol. 5, no. 5, pp. 519 – 531, 1967.

[64] A. Hodgkins, T. J. Marrow, P. Mummery, B. Marsden, and A. Fok, "X-ray tomography observation of crack propagation in nuclear graphite," *Materials Science and Technology*, vol. 22, no. 9, pp. 1045–1051, 2006.

[65] H. Li, J. Li, G. Singh, and A. Fok, "Fracture behavior of nuclear graphite NBG-18," *Carbon*, vol. 60, pp. 46 – 56, 2013.

[66] J. Yoon, T. Byun, J. Strizak, and L. Snead, "Characterization of tensile strength and fracture toughness of nuclear graphite NBG-18 using sub-size specimens," *Journal of Nuclear Materials*, vol. 412, no. 3, pp. 315 – 320, 2011.

[67] American Society for Testing and Materials, "ASTM D7779-11 - Standard Test Method for Determination of Fracture Toughness of Graphite at Ambient Temperature," 2015.

[68] M. Sakai and H. Ichikawa, "Work-of-fracture of brittle materials with microcracking and crack bridging," *International Journal of Fracture*, vol. 55, no. 1, pp. 65–79, 1992.

[69] A. Hodgkins, J. Marrow, P. Mummery, A. Fok, and B. Marsden, "Crack propagation resistance and damage mechanisms in nuclear graphite," *Special Publication - Royal Society of Chemistry*, vol. 309, p. 127, 2007.

[70] Z. Liu, S. Swartz, and K. Hu, "Two-dimensional finite element modeling of crack growth in concrete using three-dimensional damage data," *Micromechanics of Failure of Quasi-brittle Materials*, pp. 176–87, 1990.

[71] H. Hübner and H. Schuhbauer, "Experimental determination of fracture mechanics stress intensity calibration in four-point bending," *Engineering Fracture Mechanics*, vol. 9, no. 2, pp. 403 – 410, 1977.

[72] T. Becker, T. Marrow, and R. Tait, "Damage, crack growth and fracture characteristics of nuclear grade graphite using the double torsion technique," *Journal of Nuclear Materials*, vol. 414, no. 1, pp. 32 – 43, 2011.

[73] A. C. Mazzei and J. A. Rodrigues, "Alumina-mullite-zirconia composites obtained by reaction sintering: Part I. Microstructure and mechanical

behaviour," *Journal of Materials Science*, vol. 35, no. 11, pp. 2807–2814, 2000.

[74] A. C. Mazzei, J. A. Rodrigues, and V. C. Pandolfelli, "Alumina-mullite-zirconia composites obtained by reaction sintering: Part II. R-curve behavior," *Journal of Materials Science*, vol. 35, no. 11, pp. 2815–2824, 2000.

[75] M. Sakai and H. Kurita, *Fracture of Brittle Disordered Materials: Concrete, Rock and Ceramics*, ch. 15 Deformation and fracture in the frontal process zone and the crack-face contact region of a polycrystalline graphite, pp. 227–245. E & FN Spon London, 1995.

[76] Z. P. Bažant, *Scaling of structural strength*. Butterworth-Heinemann, 2005.

[77] Z. Shi, "Chapter 2 - linear elastic and nonlinear fracture mechanics," in *Crack Analysis in Structural Concrete*, pp. 23 – 64, Boston: Butterworth-Heinemann, 2009.

[78] Z. P. Bažant and M. T. Kazemi, "Size effect in fracture of ceramics and its use to determine fracture energy and effective process zone length," *Journal of the American Ceramic Society*, vol. 73, no. 7, pp. 1841–1853, 1990.

[79] B. Karihaloo, *Fracture Mechanics and Structural Concrete*. Concrete design and construction series, Longman Scientific & Technical, 1995.

[80] Z. P. Bažant, "Size effect in blunt fracture: concrete, rock, metal," *Journal of Engineering Mechanics*, vol. 110, no. 4, pp. 518–535, 1984.

[81] P. Walsh, "Fracture of plain concrete," *Indian Concrete Journal*, vol. 46, no. 11, 1972.

[82] Z. P. Bažant and M. Kazemi, "Determination of fracture energy, process zone length and brittleness number from size effect, with application to rock and conerete," *International Journal of Fracture*, vol. 44, no. 2, pp. 111–131, 1990.

[83] Z. P. Bažant, "Instability, ductility, and size effect in strain-softening concrete," in *Proceedings of the American Society of Civil Engineers*, vol. 102, pp. 331–344, Apr. 1976.

[84] Z. P. Bažant, "Size effect on structural strength: a review," *Archive of Applied Mechanics*, vol. 69, no. 9, pp. 703–725, 1999.

[85] M. Sakai and H. Kurita, "Size-effect on the fracture toughness and the r-curve of carbon materials," *Journal of the American Ceramic Society*, vol. 79, no. 12, pp. 3177–3184, 1996.

[86] W. Weibull, "The phenomenon of rupture in solids," *Proceedings of the Royal Swedish Institute for Engineering Research*, vol. 153, pp. 1–55, 1939.

[87] W. Weibull, "A statistical distribution function of wide applicability," *Journal of Applied Mechanics*, vol. 103, pp. 293–297, 1951.

[88] Z. P. Bažant, Y. Xi, and S. Reid, "Statistical size effect in quasi-brittle structures: I. Is Weibull theory applicable?," *Journal of Engineering Mechanics*, vol. 117, no. 11, pp. 2609–2622, 1991.

[89] P. Marshall and E. Priddle, "The influence of specimen size and mode of loading on the fracture of graphite," *Carbon*, vol. 11, no. 6, pp. 627 – 631, 1973.

[90] P. Warren, "Fracture of brittle materials: effects of test method and threshold stress on the weibull modulus," *Journal of the European Ceramic Society*, vol. 21, no. 3, pp. 335 – 342, 2001.

[91] S. Fok, B. Mitchell, J. Smart, and B. Marsden, "A numerical study on the application of the Weibull theory to brittle materials," *Engineering Fracture Mechanics*, vol. 68, no. 10, pp. 1171 – 1179, 2001.

[92] G. D. Quinn, "Weibull strength scaling for standardized rectangular flexure specimens," *Journal of the American Ceramic Society*, vol. 86, no. 3, pp. 508–510, 2003.

[93] T. Fett, E. Ernst, D. Munz, D. Badenheim, and R. Oberacker, "Weibull analysis of ceramics under high stress gradients," *Journal of the European Ceramic Society*, vol. 23, no. 12, pp. 2031 – 2037, 2003.

[94] American Society for Testing and Materials, "ASTM E399-12$^{\epsilon 3}$ - Standard Test Method for Linear-Elastic Plane-Strain Fracture Toughness K_{Ic} of Metallic Materials," 2013.

[95] G. Chell and R. Harrison, "Stress intensity factors for cracks in some fracture mechanics test specimens under displacement control," *Engineering Fracture Mechanics*, vol. 7, no. 2, pp. 193 – 203, 1975.

[96] G. Chell, "A procedure for incorporating thermal and residual stresses into the concept of a failure assessment diagram. Special Technical Publication 668," in *Elastic-Plastic Fracture*, pp. 581–605, American Society for Testing and Materials International, 1979.

[97] E. Robinson, "The resistance to relaxation of materials at high temperature," *Transacactions of the American Society of Mechanical Engineers*, vol. 61, pp. 543–554, 1939.

[98] G. Horne, *Elastic follow-up and the interaction between applied and residual stresses*. PhD thesis, University of Bristol, 2013.

[99] R. Roche, "Estimation of piping elastic follow up by using conventional computations," *International Journal of Pressure Vessels and Piping*, vol. 26, no. 1, pp. 53–78, 1986.

[100] R. Roche, "Spring effect and primary stress," in *Transactions of the 12th International Conference on Structural Mechanics in Reactor Technology*, 1993.

[101] D. J. Smith, J. McFadden, S. Hadidi-moud, A. J. Smith, A. J. Stormonth-Darling, and A. A. Aziz, "Elastic follow-up and relaxation of residual stresses," *Proceedings of the Institution of Mechanical Engineers, Part C: Journal of Mechanical Engineering Science*, vol. 224, no. 4, pp. 777–787, 2010.

[102] C. Aird, S. Hadidi-Moud, C. Truman, and D. Smith, "Impact of residual stress and elastic follow-up on fracture," *Journal of ASTM International*, vol. 5, no. 8, 2008.

[103] T. Marrow, D. Liu, S. Barhli, L. S. Mora, Y. Vertyagina, D. Collins, C. Reinhard, S. Kabra, P. Flewitt, and D. Smith, "In situ measurement of

the strains within a mechanically loaded polygranular graphite," *Carbon*, vol. 96, pp. 285 – 302, 2016.

[104] M. Mostafavi and T. Marrow, "In situ observation of crack nuclei in polygranular graphite under ring-on-ring equi-biaxial and flexural loading," *Engineering Fracture Mechanics*, vol. 78, no. 8, pp. 1756 – 1770, 2011.

[105] M. Mostafavi, S. McDonald, H. Çetinel, P. Mummery, and T. Marrow, "Flexural strength and defect behaviour of polygranular graphite under different states of stress," *Carbon*, vol. 59, pp. 325 – 336, 2013.

[106] M. Novovic and P. Bowen, "Biaxial strength of graphite," tech. rep., University of Birmingham, Mar. 2014.

[107] D. Liu, M. Mostafavi, J. Marrow, D. Smith, and P. Flewitt, "Cruciform biaxial flexural testing of polygranular nuclear graphite," in *Transactions of the 23rd Conference on Structural Mechanics in Reactor Technology*, Aug. 2015.

[108] F. Berto, P. Lazzarin, and C. Marangon, "Brittle fracture of U-notched graphite plates under mixed mode loading," *Materials & Design*, vol. 41, pp. 421–432, 2012.

[109] ISO, "Metallic materials - Calibration and verification of static uniaxial testing machines - Part 1: Tension/compression testing machines - Calibration and verification of the force-measuring system," 2015.

[110] T. E. Oliphant, "Python for scientific computing," *Computing in Science Engineering*, vol. 9, pp. 10–20, May 2007.

[111] S. Sato, H. Awaji, K. Kawamata, A. Kurumada, and T. Oku, "Fracture criteria of reactor graphite under multiaxial stesses," *Nuclear Engineering and Design*, vol. 103, no. 3, pp. 291 – 300, 1987.

[112] K. L. Johnson, *Contact Mechanics*. Cambridge University Press, 1985.

[113] M. Mostafavi and T. Marrow, "Quantitative in situ study of short crack propagation in polygranular graphite by digital image correlation," *Fatigue & Fracture of Engineering Materials & Structures*, vol. 35, no. 8, pp. 695–707, 2012.

[114] E. Jones, T. Oliphant, P. Peterson, *et al.*, "SciPy: Open source scientific tools for Python," 2001–. [Online; accessed 01-03-2016].

[115] J. D. Hunter, "Matplotlib: A 2d graphics environment," *Computing in Science Engineering*, vol. 9, pp. 90–95, May 2007.

[116] O. Towers, "Stress intensity factors, compliances and elastic η factors for six tests geometries," Tech. Rep. 136, The Welding Institute, Abington, UK, 1981.

[117] C. Ishiyama and Y. Higo, "Effects of humidity on Young's modulus in poly (methyl methacrylate)," *Journal of Polymer Science Part B: Polymer Physics*, vol. 40, no. 5, pp. 460–465, 2002.

[118] L. Smith and J. Sauer, "Sorbed water and mechanical behaviour of poly (methyl methacrylate)," *Plastics and Rubber Processing and Applications*, vol. 6, no. 1, pp. 57–65, 1986.

[119] M. Mostafavi, N. Baimpas, E. Tarleton, R. Atwood, S. McDonald, A. Korsunsky, and T. Marrow, "Three-dimensional crack observation, quantification and simulation in a quasi-brittle material," *Acta Materialia*, vol. 61, no. 16, pp. 6276 – 6289, 2013.

[120] H. Li, J. Duff, and T. J. Marrow, "In-situ observation of crack nucleation in nuclear graphite by digital image correlation," in *Proceedings of Pressure Vessel and Piping Division Conference, Chicago*, 2008.

[121] Z. P. Bažant, "Probability distribution of energetic-statistical size effect in quasibrittle fracture," *Probabilistic Engineering Mechanics*, vol. 19, no. 4, pp. 307 – 319, 2004.

[122] Z. P. Bažant and Z. Li, "Modulus of rupture: size effect due to fracture initiation in boundary layer," *Journal of Structural Engineering*, vol. 121, no. 4, pp. 739–746, 1995.

[123] Z. P. Bažant and D. Novák, "Probabilistic nonlocal theory for quasibrittle fracture initiation and size effect. I: Theory," *Journal of Engineering Mechanics*, vol. 126, no. 2, pp. 166–174, 2000.

[124] D. Van Gelderen, *Effects of Load History on Low Temperature Fracture of Steels*. PhD thesis, University of Bristol, 2016.

[125] Z. P. Bažant and J. Planas, *Fracture and Size Effect in Concrete and Other Quasibrittle Materials*. CRC Press, 1998.

[126] American Society for Testing and Materials, "ASTM E561-15a - Standard Test Method for K_{R} Curve Determination," 2015.

[127] C. A. Schneider, W. S. Rasband, and K. W. Eliceiri, "Nih image to imagej: 25 years of image analysis," *Nature methods*, vol. 9, no. 7, p. 671, 2012.

[128] W. McKinney, "Data structures for statistical computing in Python," in *Proceedings of the 9th Python in Science Conference* (S. van der Walt and J. Millman, eds.), pp. 51 – 56, 2010.

[129] S. Shah, "Determination of fracture parameters (K^s_{Ic} and CTOD_c) of plain concrete using three-point bend tests," *Materials and Structures*, vol. 23, no. 6, pp. 457–460, 1990.

[130] M. Sakai and R. C. Bradt, *Graphical Methods for Determining the Nonlinear Fracture Parameters of Silica and Graphite Refractory Composites*, pp. 127–142. Boston, MA: Springer US, 1986.

[131] A. Hillerborg, "Additional concrete fracture energy tests performed by 6 laboratories according to a draft RILEM recommendation," *Report TVBM*, vol. 3017, 1984.

[132] D. Higgins and J. Bailey, "Fracture measurements on cement paste," *Journal of Materials Science*, vol. 11, no. 11, pp. 1995–2003, 1976.

[133] S. Ohgishi, H. Ono, M. Takatsu, and I. Tanahashi, "Influence of test conditions on fracture toughness of cement paste and mortar," in *Fracture Toughness and Fracture Energy of Concrete: Proceedings of the International Conference on Fracture Mechanics of Concrete*, pp. 281–290, Elsevier, Amsterdam, 1986.

Appendix A

Energy release rate with compliant structure derivation

Based on [31] and [34] the compliance of the structure, is significant to the rate of change of the crack driving force. The displacement of the spring is its compliance multiplied by the applied load:

$$\Delta_M = C_M\, P \tag{A.1}$$

The total displacement is equal to the displacement of the specimen plus the displacement of the structure.

$$\Delta_T = \Delta + C_M\, P \tag{A.2}$$

Assuming that the displacement of the specimen is only affected by the load applied and the crack length we can partially differentiate.

$$d\Delta_T = \left(\frac{\partial \Delta}{\partial a}\right)_P da + \left(\frac{\partial \Delta}{\partial P}\right)_a dP + C_M dP = 0 \tag{A.3}$$

Also, assuming that the crack driving force is only affected by the crack length and the load is it also possible to partially differentiate G by the same.

$$dG = \left(\frac{\partial G}{\partial a}\right)_P da + \left(\frac{\partial G}{\partial P}\right)_a dP \tag{A.4}$$

Then both sides can be divided by da as the machine Δ_T is fixed.

$$\left(\frac{\partial G}{\partial a}\right)_{\Delta_T} = \left(\frac{\partial G}{\partial a}\right)_P + \left(\frac{\partial G}{\partial P}\right)_a + \left(\frac{\partial P}{\partial a}\right)_{\Delta_T} \tag{A.5}$$

Substituting gives:

$$\left(\frac{\partial G}{\partial a}\right)_{\Delta_T} = \left(\frac{\partial G}{\partial a}\right)_P - \left(\frac{\partial G}{\partial P}\right)_a \left(\frac{\partial \Delta}{\partial a}\right)_P \left[C_M + \left(\frac{\partial \Delta}{\partial P}\right)_a\right]^{-1} \tag{A.6}$$

Appendix B

Interpolation & Regression

Interpolation

In order to regress over cleaner data, a linear interpolation function from Python Scipy (scipy.interpolate.interp1d) was used [114]. The linearity of the interpolation would not pose a problem as enough points are used. The points used are a function of the absolute difference between initial and final displacement or load, whichever is greater. The unload and reload, separated from the whole load-CMOD data, are fed to the interpolation function. The interpolation function creates arrays of load to equally spaced values of CMOD, over the original distance fed to the function. The interpolation creates a "pure displacement control" version of the data, ideal for linear regression.

In addition to the above, the interpolation solves the problem of regressing over the faster unloading and loading blocks. As the control of the block iterations was manual, there is a high probability of the slower blocks overlapping over the faster ones on the linear parts of the loading or unloading. This could lead to errors in the regression as twice the amount of points per unit of displacement, from the lower speeds, will be sampled closer to the non-linear parts of the cycle. By interpolating over the whole cycle and creating equally spaced, in terms of CMOD, arrays of CMOD and load this concern is addressed.

Regression

Following the interpolation, the load and crack mouth opening displacement arrays were fed to a linear regression function. The CMOD arrays were chosen

as the independent variable, with the load arrays being the dependent, based on the discussion in section 4.4.2. A linear least-squares regression function from Python Scipy, as above, was used (scipy.stats.linregress) [114]. All values returned from the function for each cycle were stored in a Python pandas data frame (pandas.DataFrame) for later use [128]. The values include the slope of the regression line, the intercept on the dependent axis and the correlation coefficient r. This coefficient represents the slope of the regression line when both variables have been standardized first and makes for the coefficient of determination r^2 or R^2. Regressions over a specific length on the arrays were tested in order to maximise the coefficient and thus predictability and accuracy of the slope measurements.

Several methods for the determination of the linear portion of the cycle to be sent to the linear regression function were evaluated. These included choosing an arbitrary initial value (centre of the cyclic line) and using two rolling regressions with relatively small window sizes to determine the upper and lower limits of linearity. A variation of the method used by Van Gelderen [124] in his PhD thesis was also evaluated. In his method a starting point was used (25 % of peak load) and subsequent regressions with increasing data points from that point onwards were performed. The moment the differential of the slopes stopped oscillating around 0 would imply a limit point was reached thus marking the limit on linearity. The complicated nature and the several required assumptions made the above methods inapplicable to the amount of cyclic loadings presented in this work.

Based on the above, a simpler method was chosen. Arbitrary values of load percentage were used to define a window upon which the regression would be performed. These window were 40 to 60 % of the peak cycle load and can be seen as black dots in Figures 5.13 and 5.14 achieving R^2 values close to 1 (0.998) for almost all unload and reload cycles with small discrepancies for the last cycles with values of about 0.94. For the initial loading a window had to be chosen that would achieve R^2 values close to 1 and that would consistently provide slopes greater than the following cycles per each specimen based on graphite's strain softening behaviour. Due to the above and through trial and error, a smaller window was chosen, 2 to 15 % of the initial peak loading value. The window size was adequate to provide enough points for a regression, based on the raw data, as well as meeting the above requirements.